



저작자표시-비영리-동일조건변경허락 2.0 대한민국

이용자는 아래의 조건을 따르는 경우에 한하여 자유롭게

- 이 저작물을 복제, 배포, 전송, 전시, 공연 및 방송할 수 있습니다.
- 이차적 저작물을 작성할 수 있습니다.

다음과 같은 조건을 따라야 합니다:



저작자표시. 귀하는 원저작자를 표시하여야 합니다.



비영리. 귀하는 이 저작물을 영리 목적으로 이용할 수 없습니다.



동일조건변경허락. 귀하가 이 저작물을 개작, 변형 또는 가공했을 경우에는, 이 저작물과 동일한 이용허락조건하에서만 배포할 수 있습니다.

- 귀하는, 이 저작물의 재이용이나 배포의 경우, 이 저작물에 적용된 이용허락조건을 명확하게 나타내어야 합니다.
- 저작권자로부터 별도의 허가를 받으면 이러한 조건들은 적용되지 않습니다.

저작권법에 따른 이용자의 권리는 위의 내용에 의하여 영향을 받지 않습니다.

이것은 [이용허락규약\(Legal Code\)](#)을 이해하기 쉽게 요약한 것입니다.

[Disclaimer](#)

공학박사학위논문

**탄성 메타물질의 유효 특성 정의 및
이를 이용한 파동 테일러링**

**Effective-Property Characterization of Elastic
Metamaterials for Advanced Wave Tailoring**

2014년 2월

서울대학교 대학원

기계항공공학부

이형진

탄성 메타물질의 유효 특성 정의 및 이를 이용한 파동 테일러링

Effective-Property Characterization of Elastic
Metamaterials for Advanced Wave Tailoring

지도교수 김 윤 영

이 논문을 공학박사 학위논문으로 제출함

2013 년 12 월

서울대학교 대학원

기계항공공학부

이 형 진

이형진의 공학박사 학위논문을 인준함

2013 년 12 월

위 원 장 : _____ 강 언 준 _____

부위원장 : _____ 김 윤 영 _____

위 원 : _____ 신 상 준 _____

위 원 : _____ 김 진 오 _____

위 원 : _____ 이 중 석 _____

ABSTRACT

Effective-Property Characterization of Elastic Metamaterials for Advanced Wave Tailoring

Lee, Hyung Jin

School of Mechanical and Aerospace Engineering

The Graduate School

Seoul National University

This work is mainly concerned with the development of a characterization methodology for determining the effective properties of anisotropic elastic metamaterials. Among the existing methods, the method using the scattering parameters of metamaterials has been known to be most efficient in electromagnetics owing to the robust performances. In the elastic regime, however, the conventional method using the scattering parameters cannot thoroughly characterize metamaterials due to the complex constitutive properties including the diagonal as well as the non-diagonal components in the stiffness tensor. Therefore, the method should be refined specifically for characterizing anisotropic elastic metamaterials.

In order to achieve the goal, the improved version of the characterization method

using scattering parameters is developed in this work. The proposed method works in the two steps: one is to determine the effective constitutive properties involved in the scattering parameters for normal incidences and the other is to determine the rest of the properties involved in the scattering parameters for oblique incidences. While the conventional method just yields the diagonal stiffness components even working only for the metamaterials having the material principal axes coinciding with the coordinate axes, the proposed method is shown to work for various types of metamaterials yielding the whole effective properties.

By utilizing the developed characterization method, three types of novel elastic metamaterials are also proposed in this work and applied for the designs of elastic magnifying hyperlens, quasi-ideal mechanical bandpass filters, and wave mode converters, respectively. In order to design elastic magnifying hyperlens, metal-air-stratified metamaterials exhibiting an extremely anisotropy is used. Owing to the extreme property, the proposed hyperlens is shown to achieve high resolution images beyond the well-known diffraction limit, the fundamental limit for an imaging device. And, in order to design quasi-ideal mechanical bandpass filters, impedance-only-varying metamaterials are proposed and utilized for constructing effective impedance-varying phononic bandgap structures. The developed phononic bandgap structures are shown to exhibit quasi-ideal bandpass filter performances including a unity passband with the flat top, broad surrounding stopbands, and steep bandedges. Lastly, in order to design wave mode converters, the metamaterials exhibiting anomalous polarization characteristics are used. The developed mode converters are shown to robustly work for various environmental conditions while achieving the high conversion efficiencies.

Keywords: Anisotropic elastic metamaterials, S-parameter retrieval method, Elastic magnifying hyperlens, Mechanical bandpass filter, Wave mode converter

Student Number: 2008-20784

TABLE OF CONTENTS

ABSTRACT	i
LIST OF TABLES	ix
LIST OF FIGURES	xi
CHAPTER 1. Introduction	1
1.1 Motivation.....	1
1.2 Research Objectives.....	4
1.3 Outline of Thesis.....	7
CHAPTER 2. Theoretical Background	11
2.1 Elastic Waves in Unbounded Anisotropic Solid Media.....	11
2.1.1 Stress-strain relations for anisotropic materials.....	12
2.1.2 The Christoffel equation	16
2.1.3 Slowness surfaces.....	18
2.2 Scattering Parameters of an Anisotropic Solid Material.....	21
2.2.1 Transfer matrix.....	21
2.2.2 Scattering parameters.....	26
CHAPTER 3. Proposition of S-Parameter Retrieval Method for Effective- Property Characterization of Anisotropic Elastic Metamaterials	31
3.1 Conventional S-Parameter Retrieval Method for Elastic Metamaterials.....	33

3.1.1 Retrieving methodology.....	33
3.1.2 Limitations.....	43
3.2 Proposed S-Parameter Retrieval Method for Anisotropic Elastic Metamaterials.....	46
3.2.1 Retrieving methodology.....	47
3.2.2 Effective properties for a normal incidence.....	49
3.2.3 Effective properties for an oblique incidence.....	54
3.2.4 Validation of retrieved effective properties.....	59
3.3 Issues in the S-Parameter Retrieval Method for Elastic Metamaterials.....	60
3.4 Summary.....	63

CHAPTER 4. Design of Elastic Magnifying Hyperlens for Sub-Wavelength

Imaging by Using Extremely Anisotropic Metamaterials.....	83
4.1 Magnifying Hyperlens.....	83
4.2 Introduction of Metal-Air Multilayer Metamaterials for Extreme Anisotropy.....	84
4.2.1 Design and configuration.....	85
4.2.2 Effective-property characterization by the analytic homogenization method.....	86
4.2.3 Validation of the analytic homogenization method by the S-parameter retrieval method.....	91
4.3 Design of Elastic Magnifying Hyperlens.....	93
4.3.1 Validation of the performance by FEM simulations.....	94
4.3.2 Validation of the performance by experiments.....	96
4.3.3 Estimation of output/input power ratio.....	98

4.4 Summary.....	99
------------------	----

CHAPTER 5. Design of Quasi-Ideal Mechanical Bandpass Filters by Using

Impedance-Only-Varying Elastic Metamaterials.....	113
5.1 Quasi-Ideal Bandpass Filters.....	113
5.2 Proposition of Impedance-Varying Phononic Bandgap Structures for Bandpass Filters.....	115
5.2.1 Theoretical analysis on the impedance variation.....	116
5.2.2 Theoretical analysis on the symmetrically impedance-varying phononic bandgap structures.....	123
5.3 Proposition of Impedance-Only-Varying Elastic Metamaterials.....	129
5.3.1 Configurations of the proposed metamaterials.....	129
5.3.2 Effective-property characterization by the S-parameter retrieval method.....	131
5.3.3 Realization of the impedance-varying HQWS structures.....	133
5.4 Design of Quasi-Ideal Bandpass Filters.....	135
5.4.1 Validation of the performance by FEM simulations.....	135
5.4.2 Tailoring of the bandpass-filter performance.....	139
5.5 Summary.....	140

CHAPTER 6. Design of Wave Mode Converters by Using Elastic

Metamaterials Exhibiting Anomalous Polarizations.....	157
6.1 Wave Mode Converters.....	157
6.2 Proposition of Elastic Metamaterials Exhibiting Anomalous Polarizations...	160

6.2.1 Configurations.....	160
6.2.2 Effective-property characterization by the S-parameter retrieval method.....	162
6.2.3 Anomalous wave propagation velocities.....	164
6.2.4 Anomalous polarization characteristics.....	167
6.3 Design of Wave Mode Converters.....	168
6.3.1 Methodology for wave mode converters.....	169
6.3.2 Validation of the performance by FEM simulations.....	172
6.3.3 Robust performance for various environmental conditions.....	176
6.4 Summary.....	179
CHAPTER 7. Conclusions.....	197
REFERENCES.....	201
APPENDIX.....	213
ABSTRACT (KOREAN).....	215
ACKNOWLEDGEMENT.....	217

LIST OF TABLES

Table 3.1 The retrievable and non-retrievable elastic constants for Models 1-4 by using conventional S-parameter retrieval method.....	65
Table 3.2 The S-parameters for normal and oblique incidences which are valid for characterizing the effective properties of Models 1-4, and the effective properties involved in them.....	66
Table 3.3 The retrievable and non-retrievable elastic constants for Models 1-4 by using proposed S-parameter retrieval method.....	67

LIST OF FIGURES

Figure 2.1	The slowness surfaces for waves exhibiting the in-plane particle motions only (a) in the y - z plane of Quartz and (b) in the x - y plane of Rutile.....	29
Figure 2.2	(a) The schematic picture for wave propagation in an anisotropic medium sandwiched by isotropic media and (b) the view from the top	30
Figure 3.1	(a) The schematic picture for a metamaterial slab sandwiched by isotropic substances and (b) the simulation setups for measuring the scattering parameters of a metamaterial slab for a normal incidence (c) with the results.....	69
Figure 3.2	The schematic configurations of the metamaterial models considered in this study.....	70
Figure 3.3	The scattering parameters of (a) Model 3 and (b) Model 4 for a normal longitudinal wave incidence.....	71
Figure 3.4	The effective properties of Models 1-3 (a-c) characterized by using the conventional S-parameter retrieval method.....	72
Figure 3.5	The EFCs for Model 1 with (a) $r = 1.0$ and (b) 1.5 mm at 30 kHz.....	73
Figure 3.6	The effective properties of Model 4 characterized by using the proposed S-parameter retrieval method.....	74
Figure 3.7	The EFCs for (a) Model 3 and (b) Model 4 at 30 kHz.....	75
Figure 3.8	The simulation setups for measuring the scattering parameters for oblique incidences and the x -directional velocity fields for the oblique longitudinal wave incidences at $\theta_{inc} = 30^\circ$ and 60°	76

Figure 3.9 The effective properties of Models 1-4 (a-d) characterized by using the proposed S-parameter retrieval method.....	77
Figure 3.10 The EFCs for Models 1-4 (a-d) at 30 kHz analyzed by using the effective medium models (black solid line) and the detailed models (magenta dots).....	78
Figure 3.11 The x -directional velocity fields for oblique longitudinal wave incidences to the single slabs of (a) Model 3 and (b) Model 4 at the varying degree of θ_{inc} , simulated by the detailed models and the effective medium models.....	79
Figure 3.12 The scattering parameters of (a) Model 3 and (b) Model 4 for the longitudinal wave incidence at the varying degree of θ_{inc} , calculated by the detailed models and the effective medium models.....	80
Figure 3.13 The effective properties of (a) Model 1 and (b) Model 2, calculated by using the scattering parameters obtained from the single (grey solid lines) and the four (dots) unit slabs.....	81
Figure 3.14 The EFCs for (a) Model 1 and (b) Model 2, calculated by using the effective properties obtained from the single (grey solid lines) and the four (black solid lines) unit slabs.....	82
Figure 4.1 The schematic configuration of a metal-air multilayer metamaterial...	101
Figure 4.2 The proposed elastic magnifying hyperlens consisting of the angularly-arranged metal-air multilayer metamaterials.....	102
Figure 4.3 The EFCs for the metal-air multilayer metamaterial at 100 kHz analyzed by the effective medium (black thick solid lines) and the detailed model using the FEM (magenta dots) and the polarization vectors at specific \mathbf{k}	

(red arrows).....	103
Figure 4.4 The effective properties of (a) Model 1 and (b) Model 2, calculated by using the analytic homogenization method (grey solid lines) and the S-parameter retrieval method (dots).....	104
Figure 4.5 The EFCs for (a) Model 1 and (b) Model 2, obtained by using the analytic homogenization method (magenta dots) and the S-parameter retrieval method (black solid lines).....	105
Figure 4.6 The FEM simulation results for the radial stress distributions without (bottom-left) and with (bottom-right) the hyperlens, and the intensity distributions (top).....	106
Figure 4.7 The FEM simulation results for the radial stress distributions analyzed by the detailed (bottom-left) and the effective medium (bottom-right) models with the zoomed views (top) in the regions of A-C-D-B and A'-C'-D-B.....	107
Figure 4.8 The photos of the fabricated elastic hyperlens and the experimental setups.....	108
Figure 4.9 The experimental results for (a) the radial stress distribution and (b) the squared radial stress distributions with the passage of time.....	109
Figure 4.10 The comparisons between the experimental and the simulation results for the normalized squared stress distributions with and without the hyperlens.....	110
Figure 4.11 The schematic pictures for the definitions of the locations A-D.....	111
Figure 4.12 The comparisons between the experimental (magenta dots) and the simulation (black solid line) results.....	112

Figure 5.1 (a) The schematic of an impedance-varying 2-period QWS structure and (b) the Bloch phases and (c) the transmittances for the varying value of c	143
Figure 5.2 (a) The schematic of an impedance-varying 5-period HQWS structure and (b) the Bloch phases and (c) the transmittances for the varying value of Δ	144
Figure 5.3 (a) The schematic of a symmetrically impedance-varying 3-period HQWS structure, (b) the transitions of T_{dip} , \hat{f}_{dip} , Q_{R} , and Q_{S} for the varying value of c , and (c) the transmittance spectra for the specific values of c	145
Figure 5.4 (a) The schematic of a symmetrically impedance-varying 5-period HQWS structure and (b) the transmittance spectra for the periodic case and Cases 1-4.....	146
Figure 5.5 The transmittance spectra for the 3-, 5-, and 7-period cases.....	147
Figure 5.6 The schematic configuration of the proposed metamaterial slab.....	148
Figure 5.7 The impedances of the proposed metamaterials relative to that of aluminum for the varying design parameters L_x and h	149
Figure 5.8 The effective properties of MM-I to MM-III: relative impedance (top- left), refractive index (top-right), mass density (bottom-left), and normal stiffness (bottom-right).....	150
Figure 5.9 The schematic configuration of an effective HQWS realized by using the proposed metamaterial slabs.....	151
Figure 5.10 (a) The phase shifts in the half-wave metamaterial slabs of MM-I to MM-III and (b) their impedance values normalized to each value at	

100 kHz.....	152
Figure 5.11 (a) The schematic of the symmetrically impedance-varying HQWS structures designed by metamaterials and (b) their transmittance spectra.....	153
Figure 5.12 The scattering parameters S_{12} of the half-wave metamaterial slabs, MM-I to MM-III.....	154
Figure 5.13 (a) The transmittance spectra analyzed by the detailed and the effective medium models and (b) the distributions of the x -directional velocity fields inside the models at 100 kHz.....	155
Figure 5.14 The transmittance spectra for the designed (a) 5- and (b) 7-period HQWS structures with the varying value of z_{avg}	156
Figure 6.1 The schematic configuration of the proposed metamaterial.....	181
Figure 6.2 The effective properties of the proposed metamaterials for the varying design parameter, h	182
Figure 6.3 The dispersion curves for the proposed metamaterials with the varying design parameter, h	183
Figure 6.4 The deviation angles for the proposed metamaterials with the varying design parameter, h	184
Figure 6.5 The EFC for the proposed metamaterial with $h = 4.0$ mm at 30 kHz.....	185
Figure 6.6 (a) The schematic configuration of the proposed mode converter and the setting considered in this study, (b) the schematic pictures for the demonstration on the refraction scheme, and (c) the description of the proposed methodology for mode converters by employing the EFCs.....	186

Figure 6.7 The FEM simulation results for the (a) incident, (b) scattered, and (c-d) total wave fields, indicated by the (a-c) x - and (d) y -directional velocities.....	187
Figure 6.8 The FEM simulation results for the strain energy density fields, indicated by (a) W_{tot} , (b) W_{xx} , (c) W_{xy} , and (d) W_{yy}	188
Figure 6.9 The FEM simulation results for the x -directional velocity fields, analyzed by (a) the detailed and (b) the effective medium models with the zoomed views on the converter regions.....	189
Figure 6.10 The FEM simulation results for the x -directional velocity fields, analyzed by (a) the detailed model and (b) the effective medium model having the linear slope with the zoomed views on the converter regions.....	190
Figure 6.11 The FEM simulation results for the varying value of w_s , indicated by the x -directional velocity fields.....	191
Figure 6.12 The FEM simulation results for $w_s = 0.33D_y$ indicated by the strain energy density fields.....	192
Figure 6.13 The FEM simulation results for the varying frequency, indicated by the x -directional velocity fields.....	193
Figure 6.14 The FEM simulation results for $f = 50$ kHz, indicated by the strain energy density fields.....	194
Figure 6.15 The FEM simulation results for (a) $\theta_s^* = \theta_s + 5^\circ$ and (b) $\theta_s^* = \theta_s - 5^\circ$, indicated by the x - (left plots) and y - (right) velocity fields.....	195

CHAPTER 1.

Introduction

1.1 Motivation

Metamaterials are the artificial materials which can be designed to possess extraordinary properties that may not exist in nature including negative refractive index [1-7]. They are assembled using subwavelength-dimensional unit cells typically in the periodic arrangements, each consisting of multiple delicately-engineered elements. They achieve unique properties not from the intrinsic properties of constituent elements but rather from the arrangement and the configuration.

Over the last few decades, metamaterials have received a great attention. Beginning from a theoretic study by Veselago [8] in electromagnetics, which presents that a material possibly possesses the negative values in the permittivity and the permeability, the left-handed metamaterials were actually realized through combining split ring resonators and continuous wires by Smith [9]. Motivated by the researches, an extensive theoretic and experiment study has been reported on the realizations of metamaterials exhibiting not only negative [2, 10-12] but also zero [3, 6, 13] or extremely high refractive indices [14, 15] as well as on their applications including hyperlens [16-18], metasurfaces with extraordinary emissions [19-21], tunable phase shifters [5, 22], and filters [6, 23].

Recently, metamaterials possessing right-handed properties also have received a considerable attention because they can consistently work in a broad frequency

range owing to non-use of resonances unlike usual left-handed metamaterials [24-28]. With the help of a transformation scheme [26, 29-32], right-handed metamaterials can effectively tailor the wave propagation characteristics and even can be utilized for the designs of complex systems such as a cloak device [24, 26, 30].

In order to understand the macro-scattering-phenomena around metamaterials and design metamaterial-based systems, the most important approach is the homogenization of metamaterials [1, 9, 33-36]. Since metamaterials usually have subwavelength dimensions, they can be characterized by the homogenized media, typically referred to as “effective media”, with the constitutive properties, “effective properties”. Three characterization methods are well-known specifically in electromagnetics: one is to estimate the effective properties by approximate analytical models [1, 9], another is by numerically calculating the wave fields inside metamaterial slabs [33, 34], and the other is by measuring the scattering parameters (reflection and transmission coefficients) [35-38]. Among them, the method using the scattering parameters (S-parameters), typically referred to as “S-parameter retrieval method”, is most widely used because it can be applied for metamaterials even having the complex configurations and it works in both numerical simulations and experiments. When considering micro-structured metamaterials usually have issues in the fabrications, the working capability in experiments gives a great potential to the S-parameter retrieval method.

There have been some attempts to adopt the left-handed-material concept into elasticity over the last few years [39-44]. Several studies show the possibilities that elastic metamaterials can also achieve the negative values in mass density and

stiffness through using constituent soft-coated solid cores [42, 44, 45]. As earlier studies in electromagnetics did, many of studies in elasticity have now focused on designing and realizing left-handed metamaterials using fundamental analyses on them.

In comparison with the technical levels of designs of elastic metamaterials, the effective-property-characterization techniques have not been sufficiently developed in elasticity. Several studies tried to use the conventional S-parameter retrieval method just after adopting it from electromagnetics [46], but it cannot yield the whole effective properties specifically for anisotropic metamaterials because they possess the complex constitutive properties including not only the diagonal components but also the non-diagonal components in the stiffness tensor even when the material principal axes lie on the coordinate axes [47-49] unlike metamaterials in electromagnetics possessing only the diagonal components in tensorial properties [35, 36, 50]. Furthermore, if metamaterials have the material principal axes not coinciding with the coordinate axes, the conventional S-parameter retrieval method totally breaks due to the intrinsic extension-shear-coupling stiffness components of elastic metamaterials. For these reasons, the characterization methods using the approximate analytic models or the numeric-based simulations are usually used for elastic metamaterials.

Here are the motivations of this research:

Motivation 1: The S-parameter retrieval method specifically for anisotropic elastic metamaterials is highly demanded.

Due to the complex constitutive properties of elastic metamaterials including the diagonal as well as the non-diagonal components in the stiffness tensor, the

conventional S-parameter retrieval methods cannot thoroughly characterize elastic metamaterials. The S-parameter retrieval method, which can be implemented in not only numerical simulations but also experiments even for complexly-configured metamaterials, should be developed.

Motivation 2: Elastic metamaterials exhibiting the robust performances are highly demanded for engineering applications.

Usual elastic metamaterials utilize a resonance scheme in order to achieve negative-valued effective properties [40, 42, 44], which leads metamaterials to work in a narrow frequency range even exhibiting strong dispersive behaviors in the range. The elastic metamaterials which can work with consistency without using a resonance scheme should be developed specifically in consideration of their applications such as in a non-destructive evaluation or a wave/vibration reduction fields.

1.2 Research Objectives

The main objectives of this research are two folds: one is to develop the S-parameter retrieval method for characterizing the effective properties of anisotropic elastic metamaterials and the other is to propose elastic metamaterials exhibiting robust performances for advanced wave tailoring and utilize them for engineering applications specifically in a non-destructive evaluation field.

The research objectives can be summarized in more detail as follows:

Objective 1: Proposition of the S-parameter retrieval method for effective-property characterization of anisotropic elastic metamaterials

Anisotropic elastic metamaterials possess the distinctly different constitutive effective properties specifically in the stiffness tensor compared with other tensorial properties such as the permeability/permittivity in electromagnetics [35, 36, 50] and the density in acoustics [51-53]. The stiffness tensor consists of not only the diagonal components but also the non-diagonal components even when materials have the principal axes coinciding with the coordinate axes, due to the existence of the Poisson's ratio. If materials have the rotated principal axes, moreover, the extension-shear-coupling components additionally appear in the stiffness originating from the existence of the shear modulus. These intrinsic constitutive properties of elastic materials lead the characterization problems for metamaterials far more difficult compared with them in electromagnetics or acoustics. In consideration of the intrinsic complex properties, the conventional S-parameter retrieval method should be refined for determining the non-diagonal stiffness components of elastic metamaterials including the extension-shear-coupling components.

Objective 2: Proposition of extremely anisotropic elastic metamaterials and design of elastic magnifying hyperlens for subwavelength imaging

Hyperlens are one of the most well-known metamaterial systems, which can achieve a subwavelength imaging beyond the diffraction limit [10, 16, 54]. Owing to the extremely anisotropic properties, they can support the evanescent wave components carrying high-resolution images to propagate while maintaining the image form intact. The left-handed metamaterials are usually used for realizing hyperlens in electromagnetics, but the metamaterials suffer from the intrinsic limitations originating from the use of a resonance scheme. In elasticity, hyperlens

can give a great potential specifically to medical imaging and ultrasonic flaw detection. For realizing an elastic hyperlens, metamaterials possessing extremely anisotropic properties should be developed. Furthermore, they should exhibit the consistent behaviors in a broad working frequency range as well as the simple configurations.

Objective 3: Proposition of impedance-only-varying elastic metamaterials and design of quasi-ideal mechanical bandpass filters

Classically, there have been great demands for achieving bandpass filters. A lot of design schemes have been suggested [55-58], but it is fairly difficult to realize the filters exhibiting the quasi-ideal performances including a flattened unity passband, broad surrounding stopbands, and steep bandedges. Recently, several studies have used the phononic bandgap structures employing the Fabry-Perot resonance schemes for filter designs [55, 59], which can develop a very narrow transmission peak in the middle of a bandgap region. However, they cannot be used when wider passbands with the flat tops and steep bandedges are demanded. A novel methodology for achieving quasi-ideal bandpass filters is still highly demanded with the realizable configurations as well as the compact dimensions.

Objective 4: Proposition of elastic metamaterials exhibiting anomalous polarizations and design of wave mode converters

In a general bulk isotropic solid, there exist two wave modes; one is a longitudinal mode and the other is a transverse mode. Owing to the distinctly different polarization characteristics between the two wave modes, they each are sometimes utilized for specific applications. The demand for a wave mode converter

specifically dealing with the conversion of a longitudinal to a transverse modes arises from the facts that a transverse mode is not easy to be directly excited by using conventional piezoelectric transducers especially into a guided structure [48, 60, 61] and it suffers from significant energy attenuation when transmitted through a waveguide for diagnosing structures deeply buried in soil or immersed in water [62, 63]. The conventional critical-angle-based converters [60, 61], however, have several limitations due to the difficulty in adjusting the angles of incident and transmitted waves as well as the low conversion efficiency. So, a novel methodology for realizing a wave mode converter is highly demanded, which can overcome the above limitations. Furthermore, a converter should robustly work regardless of environmental working conditions.

1.3 Outline of Thesis

In Chapter 2, the theoretical backgrounds of this research will be reviewed. The stress-strain relations for specific material anisotropies is described first, and the wave propagation characteristics in bulk anisotropic media are analyzed by employing the slowness surfaces calculated from the Christoffel equation. And in order to derive the scattering parameters of an anisotropic medium, the transfer matrix method is adopted here.

In Chapter 3, the S-parameter retrieval method for characterizing the effective properties of anisotropic elastic metamaterials will be presented. The motivations are described first with investigating the limitations of the conventional retrieval method when the method is applied for elastic metamaterials. Then, the detail working procedure of the proposed method is explained after employing some

metamaterial models. Issues in the method are also briefly commented specifically on the bulk properties of elastic metamaterials.

In Chapter 4, elastic magnifying hyperlens for subwavelength imaging will be proposed by using extremely anisotropic elastic metamaterials. Metal-air stratified metamaterials are adopted for the design of hyperlens, which are known to possess an extreme anisotropy in acoustics. The characterization is conducted through the unique schemes with the help of an analytic homogenization method after validating it by using the S-parameter retrieval method. Then, the performances of the designed elastic hyperlens are validated by FEM simulations as well as experiments. The output/input power ratio is also estimated through experiments.

In Chapter 5, quasi-ideal mechanical bandpass filters will be proposed by using impedance-only-varying elastic metamaterials. In order to realize quasi-ideal filters, a novel methodology utilizing impedance-varying phononic bandgap structures is introduced here, and the structures are theoretically confirmed to exhibit quasi-ideal filtering performances when the symmetric arrangements of the impedance variations are used. Then, the designs of the phononic bandgap structures are implemented after proposing the simply-configured impedance-only-varying elastic metamaterials doing roles as homogeneous half-wave slabs with specific-valued characteristic impedances. The performances are validated by FEM simulations.

In Chapter 6, wave mode converters will be proposed by using the elastic metamaterials exhibiting anomalous polarizations. The simply-configured elastic metamaterials consisting of double slits are shown to possess the anomalous

effective stiffness where the value of a shear component exceeds the value of one of normal components. Two distinct characteristics are investigated originating from the properties: one is anomalous wave propagation velocities and the other is anomalous polarization characteristics. By utilizing the extraordinary characteristics of the metamaterials, a novel methodology for designing wave mode converters is proposed. Then, the converters are realized through the metamaterials and validated to work with the high efficiencies even for various environmental conditions.

In Chapter 7, the conclusion remarks for this research will be presented.

CHAPTER 2.

Theoretical Background

In this chapter, theoretical backgrounds for analyzing the wave propagation characteristics in elastic metamaterials and deriving the scattering parameters of metamaterials will be briefly presented. Since metamaterials have the subwavelength dimensions, they usually can be regarded as general homogeneous materials even when they consist of non-resonant elements. So, the wave propagation characteristics in elastic metamaterials also can be demonstrated by a classical elasticity theory. Here, the theory for elastic waves specifically in unbounded anisotropic solid media will be presented in Section 2.1 and the theory for deriving the S-parameters of an anisotropic solid material, in Section 2.2.

2.1 Elastic Waves in Unbounded Anisotropic Solid Media

In unbounded (infinite) geometric forms of anisotropic solid media, the wave propagation characteristics are totally determined by the anisotropic material properties (elastic constants) while they are by the properties as well as the geometric boundaries in semi-infinite or guided forms [47, 48, 64, 65]. So, by investigating the wave characteristics in unbounded media, material properties can be inversely estimated. In this section, the stress-strain relations for anisotropic materials will be investigated first, and the Christoffel equation will be reviewed. Then, the wave propagation characteristics in anisotropic materials will be analyzed by using the well-known slowness surfaces. The following theories are

well covered in earlier works in more detail [47-49, 64, 65].

2.1.1 Stress-strain relations for anisotropic materials

The stress-strain relations for the several types of anisotropic materials will be reviewed here [47-49, 64, 65]. The general relation can be written in an equation form as follows from the Hooke's law:

$$\sigma_{ij} = C_{ijkl} \varepsilon_{kl} \quad (2.1)$$

where σ_{ij} and ε_{kl} denotes the stress and strain tensors respectively and C_{ijkl} the stiffness tensor. Denoting the four subscripts i, j, k, l by the contracted notations as

$$\begin{aligned} I(J) = 1 \text{ for } ij(kl) = xx, \quad 2 \text{ for } yy, \quad 3 \text{ for } zz, \\ 4 \text{ for } yz, zy, \quad 5 \text{ for } xz, zx, \quad 6 \text{ for } xy, yx \end{aligned} \quad (2.2)$$

the stiffness tensor C_{ijkl} can be rewritten in a simple form as C_{IJ} when the stress and strain tensors are both symmetric specifically with the strain component ε_J defined as

$$\begin{aligned} \varepsilon_1 = \varepsilon_{xx} = \frac{\partial u_x}{\partial x}, \quad \varepsilon_2 = \varepsilon_{yy} = \frac{\partial u_y}{\partial y}, \quad \varepsilon_3 = \varepsilon_{zz} = \frac{\partial u_z}{\partial z}, \\ \varepsilon_4 = \varepsilon_{yz} = \frac{1}{2} \left(\frac{\partial u_y}{\partial z} + \frac{\partial u_z}{\partial y} \right), \quad \varepsilon_5 = \varepsilon_{zx} = \frac{1}{2} \left(\frac{\partial u_z}{\partial x} + \frac{\partial u_x}{\partial z} \right), \quad \varepsilon_6 = \varepsilon_{xy} = \frac{1}{2} \left(\frac{\partial u_x}{\partial y} + \frac{\partial u_y}{\partial x} \right) \end{aligned} \quad (2.3)$$

where u_x , u_y , and u_z represent the displacements in the x -, y -, and z -directions respectively. Instead of the notations ε_4 , ε_5 , and ε_6 indicating the tensor shear strains, the notations γ_4 , γ_5 , and γ_6 will be used here for expressing them in the engineering shear strains because the stress-strain relation usually deals with the

engineering strain components, which are defined as

$$\gamma_4 = 2\varepsilon_4 = \frac{\partial u_y}{\partial z} + \frac{\partial u_z}{\partial y}, \quad \gamma_5 = 2\varepsilon_5 = \frac{\partial u_z}{\partial x} + \frac{\partial u_x}{\partial z}, \quad \gamma_6 = \varepsilon_6 = \frac{\partial u_x}{\partial y} + \frac{\partial u_y}{\partial x}. \quad (2.4)$$

The contracted form of the stiffness tensor, C_{IJ} has 36 constants. Among the constants, however, only 21 constants are actually independent with each other because the stiffness tensor should be symmetric in linear elasticity. The stiffness tensor can be denoted in a matrix form with the most general expression as

$$\begin{Bmatrix} \sigma_1 \\ \sigma_2 \\ \sigma_3 \\ \sigma_4 \\ \sigma_5 \\ \sigma_6 \end{Bmatrix} = \begin{bmatrix} C_{11} & C_{12} & C_{13} & C_{14} & C_{15} & C_{16} \\ & C_{22} & C_{23} & C_{24} & C_{25} & C_{26} \\ & & C_{33} & C_{34} & C_{35} & C_{36} \\ & & & C_{44} & C_{45} & C_{46} \\ & \text{sym} & & & C_{55} & C_{56} \\ & & & & & C_{66} \end{bmatrix} \begin{Bmatrix} \varepsilon_1 \\ \varepsilon_2 \\ \varepsilon_3 \\ \gamma_4 \\ \gamma_5 \\ \gamma_6 \end{Bmatrix}. \quad (2.5)$$

The Eq. (2.5) indicates the stress-strain relation for a general anisotropic material, which has no plane of symmetry for the material properties. Such an anisotropic material is usually referred to as a “triclinic material” and all the three principal material axes are oblique to each other.

If materials have the symmetry planes for the material properties with more than one, the stiffness tensor can be more simply expressed with the reduced number of independent constants. Several cases are considered in the following few paragraphs.

For materials having a single plane of symmetry (1 twofold axis), the stress-strain relation can be written in a following form specifically when the symmetry plane coincides with the x - y plane:

$$\begin{Bmatrix} \sigma_1 \\ \sigma_2 \\ \sigma_3 \\ \sigma_4 \\ \sigma_5 \\ \sigma_6 \end{Bmatrix} = \begin{bmatrix} C_{11} & C_{12} & C_{13} & 0 & 0 & C_{16} \\ & C_{22} & C_{23} & 0 & 0 & C_{26} \\ & & C_{33} & 0 & 0 & C_{36} \\ & & & C_{44} & C_{45} & 0 \\ \text{sym} & & & & C_{55} & 0 \\ & & & & & C_{66} \end{bmatrix} \begin{Bmatrix} \varepsilon_1 \\ \varepsilon_2 \\ \varepsilon_3 \\ \gamma_4 \\ \gamma_5 \\ \gamma_6 \end{Bmatrix}. \quad (2.6)$$

Such a material is referred to as a “monoclinic material” and the wave propagation characteristics in the material are governed by 13 independent elastic constants.

If there are two orthogonal symmetry planes (three mutually orthogonal symmetry planes; 3 twofold axes), the stress-strain relation becomes

$$\begin{Bmatrix} \sigma_1 \\ \sigma_2 \\ \sigma_3 \\ \sigma_4 \\ \sigma_5 \\ \sigma_6 \end{Bmatrix} = \begin{bmatrix} C_{11} & C_{12} & C_{13} & 0 & 0 & 0 \\ & C_{22} & C_{23} & 0 & 0 & 0 \\ & & C_{33} & 0 & 0 & 0 \\ & & & C_{44} & 0 & 0 \\ \text{sym} & & & & C_{55} & 0 \\ & & & & & C_{66} \end{bmatrix} \begin{Bmatrix} \varepsilon_1 \\ \varepsilon_2 \\ \varepsilon_3 \\ \gamma_4 \\ \gamma_5 \\ \gamma_6 \end{Bmatrix} \quad (2.7)$$

specifically for the case where the principal material axes are aligned in the coordinate axes. Such a material is called as an “orthorhombic or orthotropic material” and it has 9 independent elastic constants. Note that the coupling components between the shear (normal) stresses and the normal (shear) strains disappear in the present case, and it will also be in the following cases.

Further to the two (three) orthogonal symmetries, if the two symmetry planes are identical to each other when one of them is rotated by 90 degrees (1 fourfold axis), the stress-strain relation can be expressed in a more simple form as

$$\begin{Bmatrix} \sigma_1 \\ \sigma_2 \\ \sigma_3 \\ \sigma_4 \\ \sigma_5 \\ \sigma_6 \end{Bmatrix} = \begin{bmatrix} C_{11} & C_{12} & C_{13} & 0 & 0 & 0 \\ & C_{11} & C_{13} & 0 & 0 & 0 \\ & & C_{33} & 0 & 0 & 0 \\ & & & C_{44} & 0 & 0 \\ \text{sym} & & & & C_{44} & 0 \\ & & & & & C_{66} \end{bmatrix} \begin{Bmatrix} \varepsilon_1 \\ \varepsilon_2 \\ \varepsilon_3 \\ \gamma_4 \\ \gamma_5 \\ \gamma_6 \end{Bmatrix} \quad (2.8)$$

with 6 independent elastic constants. For the case, a material is called as “tetragonal material”.

When material properties are symmetric with respect to a single axis aligned normal to a plane (where the properties are isotropic), the materials are referred to as “hexagonal or transversely isotropic materials” and the corresponding stress-strain relation becomes

$$\begin{Bmatrix} \sigma_1 \\ \sigma_2 \\ \sigma_3 \\ \sigma_4 \\ \sigma_5 \\ \sigma_6 \end{Bmatrix} = \begin{bmatrix} C_{11} & C_{12} & C_{13} & 0 & 0 & 0 \\ & C_{11} & C_{13} & 0 & 0 & 0 \\ & & C_{33} & 0 & 0 & 0 \\ & & & C_{44} & 0 & 0 \\ \text{sym} & & & & C_{44} & 0 \\ & & & & & (C_{11} - C_{12})/2 \end{bmatrix} \begin{Bmatrix} \varepsilon_1 \\ \varepsilon_2 \\ \varepsilon_3 \\ \gamma_4 \\ \gamma_5 \\ \gamma_6 \end{Bmatrix} \quad (2.9)$$

where only 5 independent constants survive. The Eq. (2.9) represents the relation specifically for case having the isotropic plane in the x - y plane.

Lastly, for a material having an infinite number of symmetry planes, the relation can be written as

$$\begin{Bmatrix} \sigma_1 \\ \sigma_2 \\ \sigma_3 \\ \sigma_4 \\ \sigma_5 \\ \sigma_6 \end{Bmatrix} = \begin{bmatrix} C_{11} & C_{12} & C_{12} & 0 & 0 & 0 \\ & C_{11} & C_{12} & 0 & 0 & 0 \\ & & C_{11} & 0 & 0 & 0 \\ & & & (C_{11} - C_{12})/2 & 0 & 0 \\ \text{sym} & & & & (C_{11} - C_{12})/2 & 0 \\ & & & & & (C_{11} - C_{12})/2 \end{bmatrix} \begin{Bmatrix} \varepsilon_1 \\ \varepsilon_2 \\ \varepsilon_3 \\ \gamma_4 \\ \gamma_5 \\ \gamma_6 \end{Bmatrix} \quad (2.10)$$

and the material is the well-known “isotropic material”. The isotropic materials have only 2 independent constants in their stiffness tensors.

2.1.2 The Christoffel equation

Keeping in mind the stress-strain relations for the various types of anisotropic materials shown in Section 2.1, now the Christoffel equation for anisotropic materials will be reviewed [47, 48, 64, 65]. Begin with the governing wave equation derived from the Newton’s law,

$$\nabla \cdot \boldsymbol{\sigma} = \rho \frac{\partial^2 \mathbf{u}}{\partial t^2} \quad (2.11)$$

where $\boldsymbol{\sigma}$ denotes the stress tensor and \mathbf{u} , the displacement vector and ρ , mass density. The wave equation can be rewritten in the following matrix form with subscripts as

$$\frac{\partial \sigma_{ij}}{\partial x_j} = \rho \frac{\partial^2 u_i}{\partial t^2}. \quad (2.12)$$

Substituting the stress-strain relation shown in Eq. (2.1) into Eq. (2.11) after combining with the following definition of strain

$$\varepsilon_{kl} = \frac{1}{2} \left(\frac{\partial u_k}{\partial x_l} + \frac{\partial u_l}{\partial x_k} \right), \quad (2.13)$$

the wave equation becomes

$$\frac{\partial}{\partial x_j} \left(C_{ijkl} \frac{\partial u_k}{\partial x_l} \right) = \rho \frac{\partial^2 u_i}{\partial t^2} \quad (2.14)$$

or

$$\frac{\partial C_{ijkl}}{\partial x_j} \frac{\partial u_k}{\partial x_i} + C_{ijkl} \frac{\partial^2 u_k}{\partial x_j \partial x_i} = \rho \frac{\partial^2 u_i}{\partial t^2}. \quad (2.15)$$

Under the assumption that anisotropic materials considered here are purely homogeneous, the first term in Eq. (2.15) is negligible and the equation becomes

$$C_{ijkl} \frac{\partial^2 u_k}{\partial x_j \partial x_i} = \rho \frac{\partial^2 u_i}{\partial t^2}. \quad (2.16)$$

Referring to Eq. (2.16), the wave propagation characteristics are totally determined by the stiffness tensor in an unbounded solid medium and their anisotropic characteristics follow the anisotropies of materials appearing in the stiffness tensor.

In order to investigate the detail wave propagation characteristics for the varying propagating direction, consider the following plane harmonic waves with the particle displacement, u_m propagating in an anisotropic medium:

$$u_m = U_m \exp\{j(k_n x_n - \omega t)\} \quad \text{with } j = \sqrt{-1} \quad (2.17)$$

where k_n denotes the wavenumber for the x_n -direction (propagation direction) and ω , the angular frequency while U_m , the amplitude of the particle displacement in the x_m -direction (polarization direction). Substituting Eq. (2.17) into Eq. (2.16) yields

$$k^2 C_{ijkl} n_j n_i u_k = \rho \omega^2 u_i \quad (2.18)$$

with the directional unit vector,

$$\mathbf{n} = n_x \hat{\mathbf{x}} + n_y \hat{\mathbf{y}} + n_z \hat{\mathbf{z}}. \quad (2.19)$$

Eq. (2.18) is the well-known Christoffel equation, and it can be rewritten in a detail matrix form as

$$k^2 \mathbf{\Gamma} \begin{bmatrix} u_x \\ u_y \\ u_z \end{bmatrix} = k^2 \begin{bmatrix} \Gamma_{11} & \Gamma_{12} & \Gamma_{13} \\ & \Gamma_{22} & \Gamma_{23} \\ \text{sym} & & \Gamma_{33} \end{bmatrix} \begin{bmatrix} u_x \\ u_y \\ u_z \end{bmatrix} = \rho \omega^2 \begin{bmatrix} u_x \\ u_y \\ u_z \end{bmatrix} \quad (2.20)$$

where

$$\begin{aligned} \Gamma_{11} &= C_{11}n_x^2 + C_{66}n_y^2 + C_{55}n_z^2 + 2C_{56}n_y n_z + 2C_{15}n_z n_x + 2C_{16}n_x n_y, \\ \Gamma_{22} &= C_{66}n_x^2 + C_{22}n_y^2 + C_{44}n_z^2 + 2C_{24}n_y n_z + 2C_{46}n_z n_x + 2C_{26}n_x n_y, \\ \Gamma_{33} &= C_{55}n_x^2 + C_{44}n_y^2 + C_{33}n_z^2 + 2C_{34}n_y n_z + 2C_{35}n_z n_x + 2C_{45}n_x n_y, \\ \Gamma_{12} &= C_{16}n_x^2 + C_{26}n_y^2 + C_{45}n_z^2 + (C_{46} + C_{25})n_y n_z + (C_{14} + C_{56})n_z n_x + (C_{12} + C_{66})n_x n_y, \\ \Gamma_{13} &= C_{15}n_x^2 + C_{46}n_y^2 + C_{35}n_z^2 + (C_{45} + C_{36})n_y n_z + (C_{13} + C_{55})n_z n_x + (C_{14} + C_{56})n_x n_y, \\ \Gamma_{23} &= C_{56}n_x^2 + C_{24}n_y^2 + C_{34}n_z^2 + (C_{44} + C_{23})n_y n_z + (C_{36} + C_{45})n_z n_x + (C_{25} + C_{46})n_x n_y \end{aligned} \quad (2.21)$$

and $\mathbf{\Gamma}$ is typically referred to as the Christoffel matrix. The Christoffel matrix totally consists of two kinds of elements, one is the wave propagation direction (\mathbf{n}) and the other is the elastic constants composing the stiffness tensor (\mathbf{C}).

The Christoffel equation shown in Eq. (2.18) or Eq. (2.20) gives the eigenvalue problem described as

$$\left| k^2 \Gamma_{ij}(n_x, n_y, n_z) - \rho \omega^2 \delta_{ij} \right| = 0, \quad (2.22)$$

which determines the wavevector (\mathbf{k}) variation profile at the frequency ω or the slowness (inverse of the phase velocity) variation profile for the varying wave propagation direction, \mathbf{n} . Throughout the thesis, the former shall be referred to as “equi-frequency contour (EFC)” [66-68] while the later, as “slowness surface” as in earlier works [47, 48, 64, 65].

2.1.3 Slowness surfaces

The equi-frequency contour (EFC) or slowness surface gives the wavevector or slowness variation profile for the varying angle of wave propagation direction, which enables the easy interpretation for the anisotropic properties of materials. In addition to the information on wavevector or slowness variation profile, they also carry the information on the group (energy) velocity direction, which is well-known to be always normal to the EFC or slowness surface [47, 48, 64, 65] as

$$\delta\mathbf{k} \cdot \mathbf{v}_g = 0 \quad (2.23)$$

where \mathbf{v}_g represents the group (energy) velocity and \mathbf{k} , the wave vector. In this section, the wave propagation characteristics in anisotropic materials will be investigated by employing the slowness surfaces.

Before the analysis, definitions of the phase, particle, and group velocities will be reviewed here. The phase velocity means the propagation velocity of a wave phase, which can be expressed in an equation form as

$$\mathbf{v}_p = \frac{\omega}{\mathbf{k}} \quad (2.24)$$

where \mathbf{v}_p represents the phase velocity and ω , the angular frequency. The phase velocity is equal to the inverse of the slowness, and it can be easily calculated by using the slowness surface.

The particle velocity is the moving velocity of a particle in a medium when waves propagate. Specifically when a medium is bulk isotropic, the particle velocity direction should be parallel or perpendicular to the phase velocity direction (\mathbf{k} -direction), and for the each case the wave is typically referred to as a (purely) longitudinal or a (purely) transverse wave, respectively. In a bulk anisotropic

medium, on the other hand, the particle velocity direction is not always parallel or perpendicular to the phase velocity direction, and actually the pure wave modes are rather rare. When the particle velocity direction is close to parallel or perpendicular to the phase velocity direction, the wave is referred to as a quasi-longitudinal or a quasi-transverse wave, respectively. The direction of the particle velocity, called as polarization vector, can be calculated from the Christoffel equation described in Eq. (2.18) after solving the characteristic equation in Eq. (2.22).

Lastly, the group velocity is the velocity of a wave modulation, which is defined as

$$\mathbf{v}_g = \frac{\partial \omega}{\partial \mathbf{k}}. \quad (2.25)$$

Note that the group velocity coincides with the energy velocity, meaning that the group velocity also represents the energy transport velocity of a wave. The direction of the group velocity is usually called as pointing vector. Referring to the definition in Eq. (2.23), the group velocity can be derived from the characteristic equation in Eq. (2.22) as

$$\mathbf{v}_g = -\frac{\nabla_{\mathbf{k}} \Omega}{\partial \Omega / \partial \omega} \quad (2.26)$$

where Ω denotes the characteristic equation in Eq. (2.22).

In Figure 2.1, the slowness surfaces are shown for the substances of Quartz and Rutile with the phase (\mathbf{v}_p ; marked by black dashed arrow), particle (\mathbf{v} ; red arrow), and group (\mathbf{v}_g ; blue arrow) velocity directions also graphically indicated (see APPENDIX for the material properties of Quartz and Rutile [47]). Note that the slowness surface for Quartz in Figure 2.1(a) is drawn for the waves propagating in the y - z plane specifically with the in-plane particle motions only while the slowness

surface for Rutile, in Figure 2.1(b) for the waves in the x - y plane also with the in-plane particle motions. Therefore only the two wave modes, quasilongitudinal modes located at the inside of each plot and quasitransverse modes at the outside, are shown in the plots. From the results, it is observed that the direction of \mathbf{v}_p (phase velocity) does not always coincide with the direction of \mathbf{v} (particle velocity) as previously demonstrated while the direction of \mathbf{v}_g (group velocity) is always normal to the slowness surfaces. For the case of Rutile, which is a tetragonal material, a propagating wave should be purely longitudinal or purely transverse specifically when it carries the zero value of k_x or k_y component in the x - y plane.

2.2 Scattering Parameters of an Anisotropic Solid Material

The term “scattering parameters (S-parameters)” originates from the parameters describing the electrical behaviors of linear electrical networks, specifically the reflections and transmissions of a network system, in electromagnetics [35, 69-73]. In the thesis, the term S-parameters will be employed for representing the reflection and transmission coefficients of a solid slab, whose detail definitions will be described later. Here are the contents which will be treated in this section: in Section 2.2.1, the transfer matrix for an anisotropic solid slab [74-80] will be derived first specifically for the two-dimensional (2D) case and in Section 2.2.2, the S-parameters will be calculated by using the transfer matrix [74, 78, 81-83].

2.2.1 Transfer matrix

See Figure 2.2 for the geometry of an anisotropic solid slab considered here. The anisotropic medium is set to be finite in the x -direction with the length d while infinite in the y - and z -directions, and the anisotropic slab is inserted in an isotropic medium as shown in the schematic picture in Figure 2.2(a). When dealing with the propagating plane waves in the x - y plane with the in-plane particle motions only, the problem can be simplified to a 2D problem under the plane strain condition for the z -direction [49, 84] as illustrated in Figure 2.2(b). Only the two wave modes (quasilongitudinal and quasitransverse modes with the in-plane particle motions in the x - y plane) are considered here, which are denoted by the indices QL and QT respectively in the figure. Here, the transfer matrix will be derived for the simplified case.

The stiffness tensor of an anisotropic material [47, 49] can be simply written as follows specifically for the present problem:

$$\mathbf{C} = \begin{bmatrix} C_{11} & C_{12} & C_{16} \\ & C_{22} & C_{26} \\ \text{sym} & & C_{66} \end{bmatrix}. \quad (2.27)$$

When considering the waves transporting energies in the positive and negative x -directions, the displacements in an anisotropic medium, u_x and u_y for the x - and y -directions respectively can be expressed as

$$u_x = \left(AP_x^\alpha e^{j\alpha x} + BP_x^\beta e^{j\beta x} + CP_x^\gamma e^{j\gamma x} + DP_x^\delta e^{j\delta x} \right) e^{j\sigma y} e^{-j\omega t} \quad (2.28)$$

$$u_y = \left(AP_y^\alpha e^{j\alpha x} + BP_y^\beta e^{j\beta x} + CP_y^\gamma e^{j\gamma x} + DP_y^\delta e^{j\delta x} \right) e^{j\sigma y} e^{-j\omega t} \quad (2.29)$$

where the two components in each equation usually represent the quasilongitudinal wave components for the positive- and negative- x directions respectively while the other two, the quasitransverse components. In Eqs. (2.28-29), A , B , C , and D

denote the displacement amplitudes of the wave modes having the wavevectors as α , β , γ , and δ for the x -direction respectively while σ for the y -direction. P_x^i and P_y^i ($i = \alpha, \beta, \gamma, \delta$) represent the polarization vectors for the x - and y -directions respectively and $e^{-j\omega t}$, the time harmonic term. The wavenumbers for the x -direction ($\alpha, \beta, \gamma, \delta$) and the corresponding polarization vectors ($\mathbf{P} = P_x^i \hat{\mathbf{x}} + P_y^i \hat{\mathbf{y}}$) can be determined from the Christoffel equation described in Eq. (2.18) for a given wavenumber for the y -direction, σ . Note that the four wave components having the different x -directional wavenumbers as α, β, γ , and δ share the same value of the y -directional wavenumber σ because they should follow the Snell's law [47, 48, 81, 83].

By using the governing wave equation shown in Eq. (2.16) and the simplified stiffness tensor in Eq. (2.27), the stress components σ_{xx} and σ_{xy} can be expressed in terms of u_x and u_y as

$$\sigma_{xx} = C_{11} \frac{\partial u_x}{\partial x} + C_{12} \frac{\partial u_y}{\partial y} + C_{16} \left(\frac{\partial u_y}{\partial x} + \frac{\partial u_x}{\partial y} \right) \quad (2.30)$$

$$\sigma_{xy} = C_{16} \frac{\partial u_x}{\partial x} + C_{26} \frac{\partial u_y}{\partial y} + C_{66} \left(\frac{\partial u_y}{\partial x} + \frac{\partial u_x}{\partial y} \right) \quad (2.31)$$

and rewriting Eqs. (2.30-31) in terms of the detail components of u_x and u_y in Eqs. (2.28-29) yields

$$\begin{aligned} \sigma_{xx} = & \left[j\alpha (C_{11}P_x^\alpha + C_{16}P_y^\alpha) + j\sigma (C_{12}P_y^\alpha + C_{16}P_x^\alpha) \right] A e^{j\alpha x} \\ & + \left[j\beta (C_{11}P_x^\beta + C_{16}P_y^\beta) + j\sigma (C_{12}P_y^\beta + C_{16}P_x^\beta) \right] B e^{j\beta x} \\ & + \left[j\gamma (C_{11}P_x^\gamma + C_{16}P_y^\gamma) + j\sigma (C_{12}P_y^\gamma + C_{16}P_x^\gamma) \right] C e^{j\gamma x} \\ & + \left[j\delta (C_{11}P_x^\delta + C_{16}P_y^\delta) + j\sigma (C_{12}P_y^\delta + C_{16}P_x^\delta) \right] D e^{j\delta x} \end{aligned} \quad (2.32)$$

and

$$\begin{aligned}
\sigma_{xy} = & \left[j\alpha (C_{16}P_x^\alpha + C_{66}P_y^\alpha) + j\sigma (C_{26}P_y^\alpha + C_{66}P_x^\alpha) \right] A e^{j\alpha x} \\
& + \left[j\beta (C_{16}P_x^\beta + C_{66}P_y^\beta) + j\sigma (C_{26}P_y^\beta + C_{66}P_x^\beta) \right] B e^{j\beta x} \\
& + \left[j\gamma (C_{16}P_x^\gamma + C_{66}P_y^\gamma) + j\sigma (C_{26}P_y^\gamma + C_{66}P_x^\gamma) \right] C e^{j\gamma x} \\
& + \left[j\delta (C_{16}P_x^\delta + C_{66}P_y^\delta) + j\sigma (C_{26}P_y^\delta + C_{66}P_x^\delta) \right] D e^{j\delta x}
\end{aligned} \tag{2.33}$$

with the term $e^{j\sigma y} e^{-j\omega t}$ omitted in each equation. When describing the stress fields (σ_{xx} and σ_{xy}) in Eqs. (2.32-33) and the x - and y -directional velocity fields ($\partial u_x / \partial t = v_x$ and $\partial u_y / \partial t = v_y$) in terms of the displacement amplitudes (A , B , C , and D), the following equation can be constructed:

$$\begin{Bmatrix} v_x \\ v_y \\ \sigma_{xx} \\ \sigma_{xy} \end{Bmatrix} = \mathbf{MN} \begin{Bmatrix} A \\ B \\ C \\ D \end{Bmatrix} \tag{2.34}$$

with

$$\mathbf{N} = \begin{bmatrix} e^{j\alpha x} & 0 & 0 & 0 \\ 0 & e^{j\beta x} & 0 & 0 \\ 0 & 0 & e^{j\gamma x} & 0 \\ 0 & 0 & 0 & e^{j\delta x} \end{bmatrix} \tag{2.35}$$

and \mathbf{M} consisting of the components as

$$M_{11} = -j\omega P_x^\alpha, \quad M_{12} = -j\omega P_x^\beta, \quad M_{13} = -j\omega P_x^\gamma, \quad M_{14} = -j\omega P_x^\delta,$$

$$M_{21} = -j\omega P_y^\alpha, \quad M_{22} = -j\omega P_y^\beta, \quad M_{23} = -j\omega P_y^\gamma, \quad M_{24} = -j\omega P_y^\delta,$$

$$M_{31} = j\alpha (C_{11}P_x^\alpha + C_{16}P_y^\alpha) + j\sigma (C_{12}P_y^\alpha + C_{16}P_x^\alpha),$$

$$M_{32} = j\beta (C_{11}P_x^\beta + C_{16}P_y^\beta) + j\sigma (C_{12}P_y^\beta + C_{16}P_x^\beta),$$

$$M_{33} = j\gamma (C_{11}P_x^\gamma + C_{16}P_y^\gamma) + j\sigma (C_{12}P_y^\gamma + C_{16}P_x^\gamma),$$

$$\begin{aligned}
M_{34} &= j\delta(C_{11}P_x^\delta + C_{16}P_y^\delta) + j\sigma(C_{12}P_y^\delta + C_{16}P_x^\delta), \\
M_{41} &= j\alpha(C_{16}P_x^\alpha + C_{66}P_y^\alpha) + j\sigma(C_{26}P_y^\alpha + C_{66}P_x^\alpha), \\
M_{42} &= j\beta(C_{16}P_x^\beta + C_{66}P_y^\beta) + j\sigma(C_{26}P_y^\beta + C_{66}P_x^\beta), \\
M_{43} &= j\gamma(C_{16}P_x^\gamma + C_{66}P_y^\gamma) + j\sigma(C_{26}P_y^\gamma + C_{66}P_x^\gamma), \\
M_{44} &= j\delta(C_{16}P_x^\delta + C_{66}P_y^\delta) + j\sigma(C_{26}P_y^\delta + C_{66}P_x^\delta).
\end{aligned} \tag{2.36}$$

For the anisotropic material slab with the length d in the x -direction as shown in Figure 2.2(b), the velocity and stress components in Eq. (2.34) become as follows specifically at $x=0$ and d , respectively:

$$\begin{Bmatrix} v_x \\ v_y \\ \sigma_{xx} \\ \sigma_{xy} \end{Bmatrix}_{x=0^+} = \mathbf{MN}_{x=0} \begin{Bmatrix} A \\ B \\ C \\ D \end{Bmatrix} = \mathbf{M} \begin{Bmatrix} A \\ B \\ C \\ D \end{Bmatrix} \tag{2.37}$$

and

$$\begin{Bmatrix} v_x \\ v_y \\ \sigma_{xx} \\ \sigma_{xy} \end{Bmatrix}_{x=d^-} = \mathbf{MN}_{x=d} \begin{Bmatrix} A \\ B \\ C \\ D \end{Bmatrix} \tag{2.38}$$

where the terms $x=0^+$ and $x=d^-$ indicate the x -coordinates right after the first boundary between the isotropic and the anisotropic materials and right before the second boundary respectively, both located inside the anisotropic material area. A , B , C , and D are the displacement amplitudes of propagating waves inside the anisotropic material.

Then, combining Eqs. (2.37-38) gives

$$\begin{Bmatrix} v_x \\ v_y \\ \sigma_{xx} \\ \sigma_{xy} \end{Bmatrix}_{x=d^-} = \mathbf{M} \mathbf{N}_{x=d} \mathbf{M}^{-1} \begin{Bmatrix} v_x \\ v_y \\ \sigma_{xx} \\ \sigma_{xy} \end{Bmatrix}_{x=0^+} \triangleq \mathbf{T} \begin{Bmatrix} v_x \\ v_y \\ \sigma_{xx} \\ \sigma_{xy} \end{Bmatrix}_{x=0^+} \quad (2.39)$$

where \mathbf{T} is the transfer matrix for the anisotropic material slab, which shows the relation between the velocity (stress) fields at the left and the right sides of the slab.

2.2.2 Scattering parameters

In order to calculate the scattering parameters (S-parameters) of the anisotropic material slab sandwiched by two isotropic materials as depicted in Figure 2.2(b), the continuity boundary conditions [74, 83] are imposed at the two boundaries between the isotropic and the anisotropic media. When defining the matrix \mathbf{M} in Eq. (2.36) specifically for (isotropic) Media 1 and 3 as \mathbf{M}_1 and \mathbf{M}_3 , respectively while it for (anisotropic) Medium 2 as \mathbf{M}_2 , the continuity boundary condition imposed at the first boundary yields

$$\begin{Bmatrix} v_x \\ v_y \\ \sigma_{xx} \\ \sigma_{xy} \end{Bmatrix}_{x=0^-} = \mathbf{M}_1 \begin{Bmatrix} A_1 \\ B_1 \\ C_1 \\ D_1 \end{Bmatrix} = \begin{Bmatrix} v_x \\ v_y \\ \sigma_{xx} \\ \sigma_{xy} \end{Bmatrix}_{x=0^+} \quad (2.40)$$

and the condition at the second boundary yields

$$\begin{Bmatrix} v_x \\ v_y \\ \sigma_{xx} \\ \sigma_{xy} \end{Bmatrix}_{x=d^+} = \mathbf{M}_3 \mathbf{N}_3 \Big|_{x=d} \begin{Bmatrix} A_3 \\ B_3 \\ C_3 \\ D_3 \end{Bmatrix} = \begin{Bmatrix} v_x \\ v_y \\ \sigma_{xx} \\ \sigma_{xy} \end{Bmatrix}_{x=d^-} \quad (2.41)$$

where the subscripts 1 and 3 are also used for the displacement amplitudes in order to differentiate them in Media 1 and 3, and \mathbf{N}_3 denotes the matrix \mathbf{N} defined in Eq.

(2.35) for Medium 3. Then, combining Eqs. (2.40-41) and Eq. (2.39) gives

$$\mathbf{N}_3|_{x=d} \begin{Bmatrix} A_3 \\ B_3 \\ C_3 \\ D_3 \end{Bmatrix} = \mathbf{M}_3^{-1} \mathbf{T}_2 \mathbf{M}_1 \begin{Bmatrix} A_1 \\ B_1 \\ C_1 \\ D_1 \end{Bmatrix} \quad (2.42)$$

where

$$\mathbf{T}_2 = \mathbf{M}_2 \mathbf{N}_2|_{x=d} \mathbf{M}_2^{-1}, \quad (2.43)$$

the transfer matrix for the centered anisotropic medium. Eq. (2.42) shows the relations between the displacement amplitudes in Media 1 and 3, and the S-parameters can be determined from it. After introducing the matrix \mathbf{S} indicating

$$\mathbf{S} = \mathbf{M}_3^{-1} \mathbf{T}_2 \mathbf{M}_1 = \mathbf{M}_3^{-1} (\mathbf{M}_2 \mathbf{N}_2|_{x=d} \mathbf{M}_2^{-1}) \mathbf{M}_1, \quad (2.44)$$

Eq. (2.42) can be rewritten as follows with the detail components in $\mathbf{N}_3|_{x=d}$:

$$\begin{Bmatrix} A_3 e^{j\alpha d} \\ B_3 e^{j\beta d} \\ C_3 e^{j\gamma d} \\ D_3 e^{j\delta d} \end{Bmatrix} = \mathbf{S} \begin{Bmatrix} A_1 \\ B_1 \\ C_1 \\ D_1 \end{Bmatrix}. \quad (2.45)$$

Note that in Media 1 and 3 (isotropic media), propagating waves should be purely longitudinal or purely transverse. So, among the wave components with the displacement amplitudes A_i , B_i , C_i , and D_i ($i=1, 3$), the two should represent the purely longitudinal wave components while the other two, the purely transverse components. When regarding A_i and B_i as the longitudinal components while C_i and D_i as the transverse components which propagate in the positive and negative x -directions respectively, the reflection and transmission coefficients can be derived from Eq. (2.45) specifically for the case of a longitudinal wave incidence as

$$\begin{Bmatrix} TLL \times e^{j\alpha d} \\ 0 \\ TLT \times e^{j\gamma d} \\ 0 \end{Bmatrix} = \mathbf{S} \begin{Bmatrix} 1 \\ RLL \\ 0 \\ RLT \end{Bmatrix} \triangleq \begin{Bmatrix} SLL \\ 0 \\ SLT \\ 0 \end{Bmatrix} \quad (2.46)$$

where RLL and RLT denote the reflection coefficients for reflected longitudinal and transverse waves respectively while TLL and TLT the transmission coefficients for transmitted longitudinal and transverse waves respectively. Here, the parameters SLL and SLT are introduced representing $SLL = TLL \times e^{j\alpha d}$ and $SLT = TLT \times e^{j\gamma d}$, respectively. For the case of a transverse wave incidence, Eq. (2.45) becomes

$$\begin{Bmatrix} 0 \\ TTL \times e^{j\beta d} \\ 0 \\ TTT \times e^{j\delta d} \end{Bmatrix} = \mathbf{S} \begin{Bmatrix} 0 \\ RTL \\ 1 \\ RTT \end{Bmatrix} \triangleq \begin{Bmatrix} 0 \\ STL \\ 0 \\ STT \end{Bmatrix} \quad (2.47)$$

where RTL and RTT denote the reflection coefficients for reflected longitudinal and transverse waves respectively while TTL and TTT the transmission coefficients for transmitted longitudinal and transverse waves, respectively with the definitions of $STL = TTL \times e^{j\beta d}$ and $STT = TTT \times e^{j\delta d}$.

Once the material properties for the three media are known, the S-parameters of an anisotropic material slab (Medium 2) can be calculated through using Eqs. (2.46-47) for longitudinal and transverse wave incidence cases respectively. In the thesis, the S-parameters shall be defined to representing the parameters RLL (RTL), RLT (RTT), SLL (STL), and SLT (STT) excluding TLL (TTL) and TLT (TTT) for a longitudinal (transverse) wave incidence as in earlier works in electromagnetics [70, 72, 73].

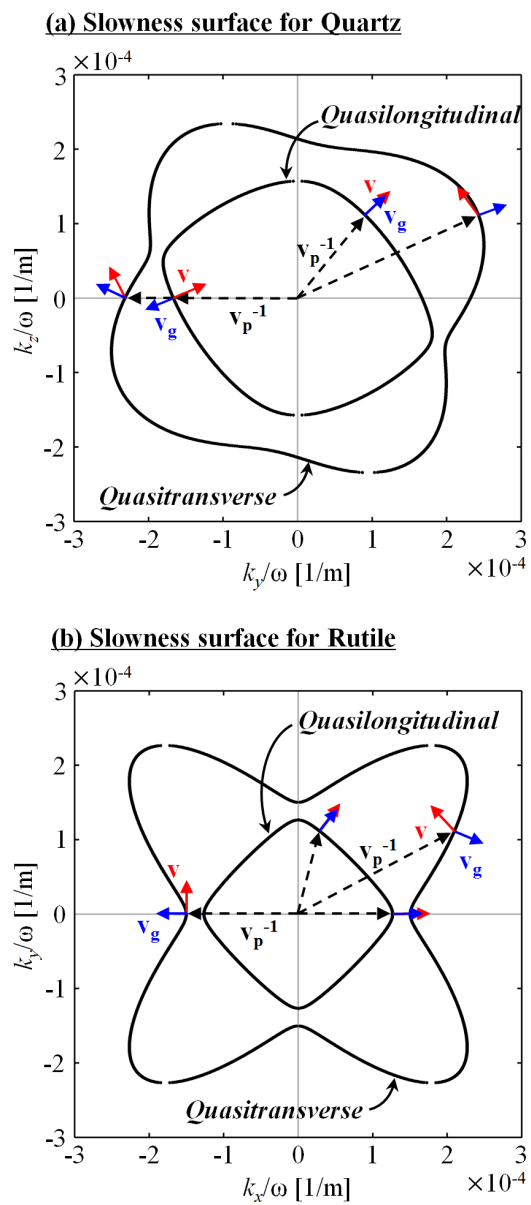


Figure 2.1 The slowness surfaces for waves exhibiting the in-plane particle motions only (a) in the y - z plane of Quartz and (b) in the x - y plane of Rutile

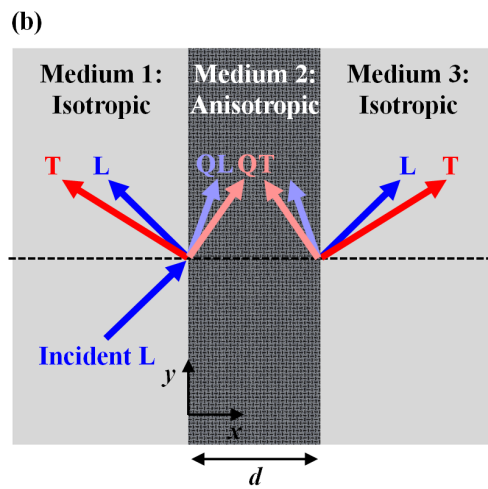
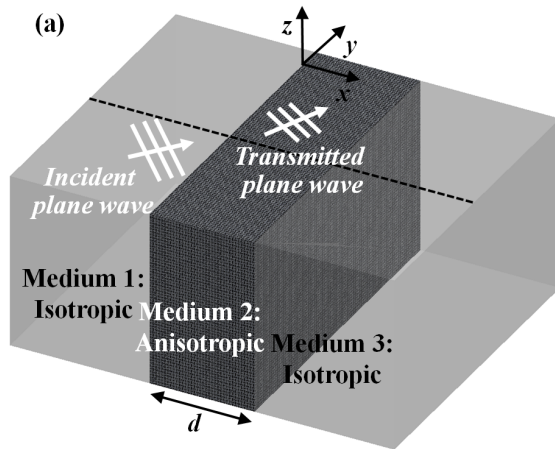


Figure 2.2 (a) The schematic picture for wave propagation in an anisotropic medium sandwiched by isotropic media and (b) the view from the top

CHAPTER 3.

Proposition of S-Parameter Retrieval Method for Effective-Property Characterization of Anisotropic Elastic Metamaterials

For characterizing wave propagation characteristics in metamaterials, the properties of metamaterials should be determined accurately. Since metamaterials usually consist of subwavelength-dimensional unit cells with the subwavelength elements in them [35, 36, 85, 86], they equivalently work as general homogeneous materials and their homogenized properties also can be defined using the same constitutive parameters with them of general materials in nature, specifically density and stiffness in elasticity. In many of metamaterial studies, the equivalent homogenized medium corresponding to a metamaterial structure is referred to as a “effective medium” while its constitutive properties, as “effective properties” [35, 36, 85, 86]. In the thesis, these terms shall be employed from now on.

Specifically in electromagnetics, many effective-property characterizing techniques are suggested for various types of metamaterials, including the techniques by using analytic models [87, 88], wave-field-averaging computations [33, 34], and the S-parameters [35-38, 86, 89, 90]. Among them, the technique using the S-parameters of metamaterials, usually referred to as an “S-parameter retrieval method”, is regarded as the most well-known and powerful tool since it yields the very accurate effective properties of metamaterials even having the complex configurations simply through using the S-parameters. The distinctive strength of this technique lies on the fact that it works not only with the estimated S-parameters from

simulations but also with the measured ones from experiments, both by the same retrieving procedure. The technique does not rely on numerical simulations unlike the other techniques.

For elastic metamaterials, the conventional S-parameter retrieval method is also used after employing it from electromagnetics [46]. However, the conventional method is not sufficient to determine the whole constitutive properties of elastic metamaterials because stiffness in elasticity has complex and different tensorial features compared to a permeability (permittivity) tensor in electromagnetics [35, 36, 91] or a density tensor in acoustics [52, 53, 92]. Even for the materials whose material principal axes are aligned with the coordinate axes, the stiffness tensor consists of the diagonal components as well as the non-diagonal components involved with the extension-extension couplings [47, 49] while the permeability (permittivity) and density tensors just consist of the diagonal ones. Furthermore, when material principal axes do not coincide with the coordinate axes, additional unique components involved with the extension-shear couplings appear in the stiffness tensor [47, 49] unlike in the permeability and density tensors, which makes the characterizations of elastic metamaterials far more difficult just by employing the conventional retrieval method. Refinements on the method are surely required for characterizing elastic metamaterials.

Here are the contents for this chapter. After introducing the conventional S-parameter retrieval method specifically for elastic metamaterials in Section 3.1, the improved version of the method will be proposed and the validations will be implemented in Section 3.2. The rest part of the chapter covers the issues in the method in 3.3 and a summary of the chapter.

3.1 Conventional S-Parameter Retrieval Method for Elastic Metamaterials

In electromagnetics, the conventional S-parameter retrieval method works with the crucial constraint that the material principal axes of metamaterials are aligned with the coordinate axes [35, 36, 54]. The constraint leads only the diagonal components to survive in the permeability and permittivity tensors and it reduces the number of effective properties, which should be defined. Then, by using normal plane wave incidences to the material principal (coordinate) axes, each involving diagonal component in the tensorial properties can be retrieved from the S-parameters. Although the effective stiffness tensor for elastic metamaterials consists of the diagonal as well as the non-diagonal components even under the constraint on the material and coordinate axes unlike the tensorial properties in electromagnetics, the conventional method in electromagnetics can be employed for characterizing elastic metamaterials, but just for determining the diagonal components in the stiffness tensor [46].

3.1.1 Retrieving methodology

The conventional S-parameter retrieval method works in a following procedure [35, 36, 92]. First, the S-parameters (reflection and transmission coefficients) of a metamaterial slab are measured specifically for normal plane wave incidences to the slab surfaces (coinciding with the material and coordinate axes). Secondly, under the assumption that the metamaterial slab can be characterized using the constitutive parameters of general homogenous materials, the effective properties

are inversely estimated from the S-parameters by using the relations between the S-parameters and the homogenized material properties.

By following the same procedure, the elastic metamaterials also can be characterized. The schematic pictures in Figure 3.1 demonstrate how to obtain the S-parameters of an elastic metamaterial slab. To simplify the problem, the two-dimensional bulk elastic metamaterials having simply-shaped void inhomogeneities are employed here.

Referring to Figure 3.1(a), the S-parameters of a metamaterial slab can be simply measured after inserting the slab into an infinite isotropic solid material whose properties are same with them of the metamaterial substrate. In the conventional retrieving procedure, only the S-parameters for normal incidences ($\theta_{\text{inc}} = 0$) are required. The detail simulation setups for measuring the S-parameters for a normal incidence are depicted in Figure 3.1(b) also with the results at a specific frequency in Figure 3.1(c). The simulations are conducted using COMSOL Multiphysics 3.5a. The periodic boundary conditions are imposed at the top and bottom edges aligned along the x -direction in order to obtain the responses of a metamaterial slab for a plane wave incidence, and the perfectly matched layers (PMLs) are used in the analysis domain located at the leftmost and the rightmost for eliminating wave reflections at the left and right edges of the domain. And for the present case the free end boundary condition is imposed at the boundaries of void inhomogeneity inside the metamaterial slab.

When considering only the metamaterials that work as general homogeneous materials here, they should satisfy the bulk property and their effective properties are identical regardless of the slab thicknesses [35, 36, 93, 94]; the effective

properties of the metamaterial slab consisting of multiple unit cells along the x -direction as shown in the upper schematic in Figure 3.1(b) are assumed to correspond with them of the slab consisting of a single unit cell as shown in the lower. So, the S-parameters of the metamaterial slab with a single unit cell should sufficiently yield the effective properties. The incident longitudinal wave field is shown at the top in Figure 3.1(c) by the x -directional velocity (v_x) component and the scattered field at the present metamaterial slab, at the center while their total fields at the bottom. The S-parameters can be derived after analyzing the wave fields.

In this chapter, the detail retrieval results shall be demonstrated after employing the several specific metamaterial models constructed using the following simply-shaped void inhomogeneities into an aluminum substrate (mass density $\rho_0 = 2700 \text{ kg/m}^3$, Young's modulus $E_0 = 7.1 \times 10^{10} \text{ N/m}^2$, Poisson's ratio $\nu_0 = 0.33$) with the lattice constants L_x and L_y for the x - and y -directions respectively as depicted in Figure 3.2:

Model 1: a circle with the radius r ,

Model 2: a square with the length w ,

Model 3: a rectangle with the width w and the height h ,

Model 4: a rectangle with the width w and the height h , rotated by the angle θ_{rot} .

Before presenting the results for the effective properties of the above metamaterial models by using the conventional S-parameter retrieval method, the relations between the S-parameters and the constitutive material properties will be reviewed in the following few paragraphs specifically for a normal wave incidence along the x -direction [35, 36, 69, 90]. Here, the case where a solid slab having the finite

length just in the x -direction is inserted in an infinite homogeneous solid material is considered just as illustrated in Figure 2.2 (2D case in the x - y plane), and the slab is assumed to have the material principal axes aligned with the coordinate axes ($C_{16} = C_{26} = 0$).

Begin with Eq. (2.36) to investigate the matrix \mathbf{M} for the solid slab (having the material axes aligned with the coordinate axes). For the x -directional normal incidence of a longitudinal (transverse) wave into the slab, only the purely longitudinal (transverse) waves propagating along the positive and negative x -directions ($\sigma = 0$) should develop inside the slab. The polarization vectors of the positive- and negative-propagating waves should be $\mathbf{P}^\alpha = 1\hat{\mathbf{x}} + 0\hat{\mathbf{y}}$ and $\mathbf{P}^\beta = -1\hat{\mathbf{x}} + 0\hat{\mathbf{y}} = -\mathbf{P}^\alpha$ respectively for the longitudinal waves while both $\mathbf{P}^\gamma = \mathbf{P}^\delta = 0\hat{\mathbf{x}} + 1\hat{\mathbf{y}}$ for the transverse waves, and it leads the matrix \mathbf{M} in Eq. (2.36) into the following simplified form under the conditions that $\sigma = 0$ and $C_{16} = C_{26} = 0$:

$$\mathbf{M} = \begin{bmatrix} -j\omega & j\omega & 0 & 0 \\ 0 & 0 & -j\omega & -j\omega \\ j\alpha C_{11} & j\alpha C_{11} & 0 & 0 \\ 0 & 0 & j\beta C_{66} & -j\beta C_{66} \end{bmatrix} \quad (3.1)$$

where α and β represent the x -directional wavenumbers of longitudinal and transverse waves respectively. And the matrix \mathbf{N} described in Eq. (2.35) becomes

$$\mathbf{N} = \begin{bmatrix} e^{j\alpha x} & 0 & 0 & 0 \\ 0 & e^{-j\alpha x} & 0 & 0 \\ 0 & 0 & e^{j\beta x} & 0 \\ 0 & 0 & 0 & e^{-j\beta x} \end{bmatrix}. \quad (3.2)$$

As seen in Eq. (3.1), longitudinal and transverse wave modes are completely

decoupled for the present case, and the matrix \mathbf{M} can be divided into \mathbf{M}^α and \mathbf{M}^β as follows for longitudinal and transverse modes respectively while \mathbf{N} also:

$$\mathbf{M}^\alpha = \begin{bmatrix} -j\omega & j\omega \\ j\alpha C_{11} & j\alpha C_{11} \end{bmatrix} \quad (3.3)$$

and

$$\mathbf{M}^\beta = \begin{bmatrix} -j\omega & -j\omega \\ j\beta C_{66} & -j\beta C_{66} \end{bmatrix} \quad (3.4)$$

while

$$\mathbf{N}^\alpha = \begin{bmatrix} e^{j\alpha x} & 0 \\ 0 & e^{-j\alpha x} \end{bmatrix} \quad (3.5)$$

and

$$\mathbf{N}^\beta = \begin{bmatrix} e^{j\beta x} & 0 \\ 0 & e^{-j\beta x} \end{bmatrix}. \quad (3.6)$$

By substituting \mathbf{M}^α (\mathbf{M}^β) and \mathbf{N}^α (\mathbf{N}^β) into Eq. (2.43), the transfer matrix for a longitudinal (transverse) wave mode can be derived. Specifically for a longitudinal mode, the transfer matrix for the slab can be expressed as

$$\mathbf{T}^\alpha = \mathbf{M}^\alpha \mathbf{N}^\alpha \Big|_{x=d} (\mathbf{M}^\alpha)^{-1} \quad (3.7)$$

and becomes

$$\mathbf{T}^\alpha = \begin{bmatrix} \cos(\alpha d) & -(j/z^\alpha) \sin(\alpha d) \\ -jz^\alpha \sin(\alpha d) & \cos(\alpha d) \end{bmatrix} \quad (3.8)$$

with the characteristic (acoustic) impedance z^α of the slab for a longitudinal wave mode defined as

$$z^\alpha = \frac{\alpha C_{11}}{\omega} = \sqrt{\rho C_{11}} \quad (3.9)$$

where ρ denotes the mass density of the slab.

For a transverse wave mode, the transfer matrix is expressed as

$$\mathbf{T}^\beta = \mathbf{M}^\beta \mathbf{N}^\beta \Big|_{x=d} (\mathbf{M}^\beta)^{-1} \quad (3.10)$$

and becomes

$$\mathbf{T}^\beta = \begin{bmatrix} \cos(\beta d) & -(j/z^\beta) \sin(\beta d) \\ -jz^\beta \sin(\beta d) & \cos(\beta d) \end{bmatrix} \quad (3.11)$$

with the characteristic impedance of the slab for a transverse wave mode defined as

$$z^\beta = \frac{\beta C_{66}}{\omega} = \sqrt{\rho C_{66}}. \quad (3.12)$$

Now, the detail components in the matrix \mathbf{S} will be investigated by using Eq. (2.44).

When defining the matrices \mathbf{M}_1 and \mathbf{M}_3 in Eq. (2.44), which represent \mathbf{M} for the isotropic media surrounding the slab located at the left and right sides respectively, both as \mathbf{M}_0^α (\mathbf{M}_0^β) for a longitudinal (transverse) wave mode, they also can be expressed in the following simplified forms by employing Eqs. (3.3-4):

$$\mathbf{M}_0^\alpha = \begin{bmatrix} -j\omega & j\omega \\ j\alpha_0 C_{11}^0 & j\alpha_0 C_{11}^0 \end{bmatrix} \quad (3.13)$$

and

$$\mathbf{M}_0^\beta = \begin{bmatrix} -j\omega & -j\omega \\ j\beta_0 C_{66}^0 & -j\beta_0 C_{66}^0 \end{bmatrix} \quad (3.14)$$

where α_0 (β_0) represents the x -directional longitudinal (transverse) wavenumber in the surrounding isotropic media and C_{11}^0 (C_{66}^0), the stiffness component governing the longitudinal (transverse) wave propagation in the media.

Then, the matrix \mathbf{S} can be expressed as follows in terms of \mathbf{T}^α (\mathbf{T}^β) and \mathbf{M}_0^α

(\mathbf{M}_0^β) :

$$\mathbf{S}^\alpha = (\mathbf{M}_0^\alpha)^{-1} \mathbf{T}^\alpha \mathbf{M}_0^\alpha \quad (3.15)$$

for a longitudinal wave mode where the detail components in \mathbf{S}^α are

$$S_{11}^\alpha = \cos(\alpha d) + j \frac{1}{2} \left(\frac{z^\alpha}{z_0^\alpha} + \frac{z_0^\alpha}{z^\alpha} \right) \sin(\alpha d) \quad (3.16a)$$

$$S_{12}^\alpha = -j \frac{1}{2} \left(\frac{z^\alpha}{z_0^\alpha} - \frac{z_0^\alpha}{z^\alpha} \right) \sin(\alpha d) \quad (3.16b)$$

$$S_{21}^\alpha = j \frac{1}{2} \left(\frac{z^\alpha}{z_0^\alpha} - \frac{z_0^\alpha}{z^\alpha} \right) \sin(\alpha d) \quad (3.16c)$$

$$S_{22}^\alpha = \cos(\alpha d) - j \frac{1}{2} \left(\frac{z^\alpha}{z_0^\alpha} + \frac{z_0^\alpha}{z^\alpha} \right) \sin(\alpha d) \quad (3.16d)$$

while

$$\mathbf{S}^\beta = (\mathbf{M}_0^\beta)^{-1} \mathbf{T}^\beta \mathbf{M}_0^\beta \quad (3.17)$$

for a transverse wave mode where the detail components in \mathbf{S}^β are

$$S_{11}^\beta = \cos(\beta d) + j \frac{1}{2} \left(\frac{z^\beta}{z_0^\beta} + \frac{z_0^\beta}{z^\beta} \right) \sin(\beta d) \quad (3.18a)$$

$$S_{12}^\beta = j \frac{1}{2} \left(\frac{z^\beta}{z_0^\beta} - \frac{z_0^\beta}{z^\beta} \right) \sin(\beta d) \quad (3.18b)$$

$$S_{21}^\beta = -j \frac{1}{2} \left(\frac{z^\beta}{z_0^\beta} - \frac{z_0^\beta}{z^\beta} \right) \sin(\beta d) \quad (3.18c)$$

$$S_{22}^\beta = \cos(\beta d) - j \frac{1}{2} \left(\frac{z^\beta}{z_0^\beta} + \frac{z_0^\beta}{z^\beta} \right) \sin(\beta d) \quad (3.18d)$$

with the characteristic impedance z_0^α (z_0^β) of the surrounding media for a longitudinal (transverse) wave defined as

$$z_0^\alpha = \frac{\alpha_0 C_{11}^0}{\omega} = \sqrt{\rho_0 C_{11}^0} \quad (3.19)$$

and

$$z_0^\beta = \frac{\beta_0 C_{66}^0}{\omega} = \sqrt{\rho_0 C_{66}^0} . \quad (3.20)$$

Then, the S-parameters of the slab for the normal incidence of a longitudinal wave can be derived when substituting Eq. (3.16) into Eq. (2.46) as

$$SLL = \left[\cos(\alpha d) - j \frac{1}{2} \left(\frac{z^\alpha}{z_0^\alpha} + \frac{z_0^\alpha}{z^\alpha} \right) \sin(\alpha d) \right]^{-1}, \quad (3.21)$$

$$RLL = \frac{-j \frac{1}{2} \left(\frac{z^\alpha}{z_0^\alpha} - \frac{z_0^\alpha}{z^\alpha} \right) \sin(\alpha d)}{\cos(\alpha d) - j \frac{1}{2} \left(\frac{z^\alpha}{z_0^\alpha} + \frac{z_0^\alpha}{z^\alpha} \right) \sin(\alpha d)} \quad (3.22)$$

while the S-parameters for a transverse wave, when substituting Eq. (3.18) into Eq. (2.47) as

$$STT = \left[\cos(\beta d) - j \frac{1}{2} \left(\frac{z^\beta}{z_0^\beta} + \frac{z_0^\beta}{z^\beta} \right) \sin(\beta d) \right]^{-1}, \quad (3.23)$$

$$RTT = \frac{j \frac{1}{2} \left(\frac{z^\beta}{z_0^\beta} - \frac{z_0^\beta}{z^\beta} \right) \sin(\beta d)}{\cos(\beta d) - j \frac{1}{2} \left(\frac{z^\beta}{z_0^\beta} + \frac{z_0^\beta}{z^\beta} \right) \sin(\beta d)}. \quad (3.24)$$

Eqs. (3.21-24) shows how the effective properties of a metamaterial slab are inversely estimated from the S-parameters. Once the S-parameters of the slab are measured, the effective wavenumber α (β) of an x -directional longitudinal (transverse) wave and the characteristic impedance, z^α (z^β) of the slab can be retrieved from Eqs. (3.21-24) with the known value of z_0^α (z_0^β), leading the

effective mass density ρ and the stiffness component, specifically C_{11} (C_{66}) also to be determined.

For the easier retrieval procedure, the effective parameters α (β) and z^α (z^β) in Eqs. (3.21-24) are expressed in terms of the S-parameters as follows:

$$\cos(\alpha d) = \frac{1 - RLL^2 + SLL^2}{2SLL}, \quad (3.25)$$

$$\left(\frac{z^\alpha}{z_0^\alpha} \right)^2 = \frac{(1 + RLL)^2 - SLL^2}{(1 - RLL)^2 - SLL^2} \quad (3.26)$$

through combining Eqs. (3.21-22) while

$$\cos(\beta d) = \frac{1 - RTT^2 + STT^2}{2STT}, \quad (3.27)$$

$$\left(\frac{z^\beta}{z_0^\beta} \right)^2 = \frac{(1 - RTT)^2 - STT^2}{(1 + RTT)^2 - STT^2} \quad (3.28)$$

through combining Eqs. (3.23-24) where the signs of the wave number, α (β) and the characteristic impedance, z^α (z^β) can be chosen as follows by employing the indefinite medium condition [35, 36, 85, 86] for a metamaterial slab:

$$\text{imag}(\alpha) \geq 0 \quad \text{and} \quad \text{real}(z^\alpha) \geq 0 \quad (3.29)$$

while

$$\text{imag}(\beta) \geq 0 \quad \text{and} \quad \text{real}(z^\beta) \geq 0. \quad (3.30)$$

where $\text{real}(A)$ and $\text{imag}(A)$ represent the real and imaginary values of A , respectively.

Now, the effective properties of the metamaterial models presented in Figure 3.2 will be characterized by using Eqs. (3.25-30). Note again that the conventional retrieval procedure using Eqs. (3.25-30) cannot be applied for Model 4, which have

the material principal axes not aligned with the coordinate axes when $\theta_{\text{rot}} \neq 0$. So, only Models 1-3 will be considered in this section dealing the conventional retrieval method. The S-parameters calculated by analyzing the wave fields around the metamaterial slab consisting of a single unit cell along the x -direction as demonstrated in Figure 3.1 are shown in Figure 3.3(a) specifically for Model 3 with $w=0.2$ mm, $h=5$ mm, and $L_x=L_y=6$ mm while the S-parameters of Model 4 having the same configuration with present Model 3 but with $\theta_{\text{rot}}=45^\circ$ are also shown in Figure 3.3(b) for the comparison. Both the sets of S-parameters are calculated for the normal incidence of a longitudinal wave in the frequency range between 10 and 30 kHz. The S-parameters for Model 3 exhibit the zero values of RLT and SLT , which represent the reflected and transmitted transverse wave ratios to an incident longitudinal wave (associated with the wave mode conversion ratios), confirming that the material principal axes lie in the coordinate axes and the conventional retrieval method can be applied for the model. The S-parameters for Model 4, on the other hand, exhibit the non-zero values and they violate the characterization by using the conventional method.

In Figure 3.4, the effective properties of Models 1-3 are determined for the following geometric parameters as

- (a) Model 1: $r=1$ mm,
- (b) Model 2: $w=h=2$ mm,
- (c) Model 3: $w=0.2$ mm and $h=5$ mm

while the lattice constants for the x - and y -directions are set to be $L_x=L_y=6$ mm for all the cases. The results for the density and the stiffness components,

specifically C_{11} and C_{66} are shown in the left and right plots respectively for each case where ρ and C_{11} , which are retrieved from a longitudinal wave incidence by using Eqs. (3.25-26), are marked by blue lines while ρ and C_{11} , retrieved from a transverse wave incidence by using Eqs. (3.27-28), by red lines. Note that the values of ρ retrieved from longitudinal and transverse wave incidences are slightly different and the discrepancy increases as frequency increases because the Bragg regimes for the two wave modes are different [95]. The frequency region of the Bragg regime for a transverse wave is usually lower than it for a longitudinal wave, leading the dispersions along the frequency in the effective properties from a transverse wave to be stronger than those from a longitudinal wave. In spite of the discrepancy in the values of ρ , they are observed to be negligible in the long-wavelength limit.

3.1.2 Limitations

In the previous section, the conventional S-parameter retrieval method is shown to capably yield the effective properties of elastic metamaterials, specifically the diagonal components in the stiffness tensor and the density when the metamaterials have the material principal axes aligned with the coordinate axes. The constraint on the material and coordinate axes is an essential requirement for the operation of the conventional method.

There exist two main limitations in the conventional retrieval method for characterizing the effective properties of elastic metamaterials:

Limitation 1: the non-diagonal components in the stiffness tensor cannot be determined,

Limitation 2: metamaterials not satisfying the constraint on the material and coordinate axes cannot be characterized.

The first limitation applies to the retrieval method only when characterizing elastic metamaterials. In electromagnetics and acoustics, there exist only the diagonal components in the tensorial constitutive parameters such as permeability (permittivity) in electromagnetics [35, 50, 89, 96, 97] and density in acoustics [51, 52, 88, 92] specifically when the material principal and coordinate axes coincide with each other. Just in elasticity, the tensorial parameter, stiffness, instinctively contains the non-diagonal components involved with the extension-extension couplings even under the constraint on the material axes, and they cannot be determined through the conventional method. Only if metamaterials are confirmed to exhibit the isotropic material properties, the whole effective properties can be defined. Confirming the isotropy, however, highly requires another property-characterization technique because it cannot be done just through looking at the configurations of metamaterials.

See the EFCs for Model 1 with $r = 1$ and 1.5 mm in Figures 3.5(a, b) respectively, which are calculated by using the finite element method (FEM) [66-68] solving the eigenvalue problems on the models. The EFCs at 30 kHz specifically for the quasilongitudinal and quasitransverse wave modes exhibiting the in-plane motions in the x - y plane are marked by blue dots while they in the (isotropic) aluminum substance, by black solid lines. Even though the constituent void inhomogeneity is simply circular-shaped in both the cases, the profiles of the EFCs are actually not circular and also vary according to the geometric parameter r . It means the model even consisting of a circular element is not always isotropic (strictly speaking,

transversely isotropic for the present 2D cases), and the effective non-diagonal stiffness component (C_{12}) cannot be guaranteed to satisfy the relation $C_{12} = C_{11} - 2C_{66}$ just as seen in isotropic materials. It leads elastic metamaterials not to be wholly characterized through using the conventional method.

The second limitation, on the other hand, applies to the retrieval method not only in elasticity but also in electromagnetics and acoustics. When metamaterials have the material principal axes not aligned with the coordinate axes, the non-diagonal components in tensorial parameters should appear, which are not covered in the conventional method. Specifically for the case in elasticity, the number of the non-diagonal components is significantly larger than the number in electromagnetics or acoustics due to the intrinsic extension-shear coupling components, leading the characterizations far more difficult.

In order to overcome the limitation, the assumption that the tensorial material parameters of metamaterials having the tilted material axes are possibly estimated employing the coordinate transformation is usually used in electromagnetics and acoustics [90, 98-100]. Also in elasticity, the assumption is frequently used [44, 45]. When considering the effective properties of metamaterials are determined by the detail shapes of the constituent elements as well as the unit cell boundaries, however, the assumption seems to be not always true. The unit cell boundaries should give a strong influence on the effective properties specifically when metamaterials exhibit the strong interactions among the adjacent unit cells or the non-local effects [37, 89, 93, 101-103]. It shall be demonstrate in detail later.

The retrievable and non-retrievable stiffness components (elastic constants) by using the conventional S-parameter retrieval method are listed in Table 3.1 for the

metamaterial models presented in Figure 3.2. For Models 1-3 exhibiting the material axes aligned with the coordinate axes, the diagonal components (C_{11} , C_{66} , and C_{22} with the unit cell rotation [92, 104]) can be determined while the non-diagonal components (C_{12}) cannot. Only for the cases where the models are confirmed to possess the isotropic material properties, the non-diagonal components can be estimated by using the relation $C_{12} = C_{11} - 2C_{66}$ as previously mentioned [47, 49]. For Model 4 exhibiting the material axes not aligned with the coordinate axes, the diagonal as well as the non-diagonal components cannot be determined at all.

3.2 Proposed S-Parameter Retrieval Method for Anisotropic Elastic Metamaterials

In this section, the improved version of the S-parameter retrieval method will be proposed, which can be applied for general anisotropic elastic metamaterials. The proposed method overcomes the limitations of the conventional method, which are the non-retrievabilities of the non-diagonal components in the effective stiffness tensor and the whole effective parameters for the metamaterials having the material axes not aligned with the coordinate axes. First, in order to determine the non-diagonal components, the S-parameters are measured not only for normal incidences but also for oblique incidences and the effective properties are extracted from them. The use of an oblique incidence has been introduced in earlier works in electromagnetics [38, 89, 90, 98], but it is just for revealing the dependence or independence of the diagonal components in tensorial parameters on the varying angles of incident waves not for determining the non-diagonal components.

Secondly, in order to characterize the metamaterials having the tilted material axes and directly determine the effective properties without using the coordinate transformation on the stiffness, the analytic relations between the S-parameters and the homogenized constitutive properties are derived for a general anisotropic solid material. The details will be demonstrated in the following sections.

3.2.1 Retrieval methodology

The proposed retrieval methodology works in the two main steps:

Step 1: determine the effective properties involved in the S-parameters for normal incidences; specifically ρ , C_{11} , C_{16} , and C_{66} for the 2D metamaterial models in Figure 3.2 by using x -directional normal incidences

Step 2: determine the rest of the effective properties involved in the S-parameters for oblique incidences; specifically C_{12} , C_{22} , and C_{26} for the 2D models.

The S-parameters for normal and oblique incidences which are valid for characterizing the effective properties of Models 1-4 are summarized in Table 3.2 with the effective properties involved in them also.

For normal incidences, the S-parameters are totally determined by the material properties including ρ , C_{11} , C_{16} , and C_{66} for the x -directional incidences while ρ , C_{22} , C_{26} , and C_{66} for the y -directional incidences (in 2D case). And for oblique incidences, the S-parameters are determined by ρ and the whole components in the stiffness tensor. When considering it, the retrieval procedure performed in the above two steps should be more efficient while yielding the more accurate values of the effective properties than the procedure retrieving the whole properties at once.

Note that the two-step approach is available only when metamaterials exhibit the local responses [89, 93, 101]. If metamaterials exhibit the non-local responses, on the other hand, the effective material parameters should vary depending on a varying incident angle, and the whole properties including ρ and \mathbf{C} are necessarily retrieved at once at each angle. The thesis covers only the metamaterials with the local responses, and the effective properties are characterized by using the proposed two-step retrieval procedure.

Here, it should be worth to remark that the procedure in Step 1 becomes identical to the procedure done in the conventional method specifically for the metamaterials whose material axes lie in the coordinate axes since the longitudinal and transverse wave modes in the metamaterials are totally decoupled in the case; through the normal incidence of a longitudinal wave incidence, ρ and C_{11} (or C_{22}) are determined and through the normal incidence of a transverse wave, ρ and C_{66} are determined. For the metamaterials with the tilted material axes, on the other hand, just the S-parameters for the normal incidence of a longitudinal or transverse wave are used and they sufficiently yield the material properties involved such as ρ , C_{11} , C_{16} , and C_{66} for the x -directional incidence while ρ , C_{22} , C_{26} , and C_{66} for the y -directional incidence.

Following the proposed two-step retrieval procedure, the whole material properties can be well determined including not only the diagonal components in the stiffness tensor but also the non-diagonal components even for the metamaterials with the tilted material axes. And it doesn't require the cell rotation or other directional normal incidences as done in [92, 104] just for determining the other diagonal stiffness components since the components can be determined through the oblique

wave incidences. The detail procedures will be demonstrated in the following sections after employing the metamaterial models in Figure 3.2.

3.2.2 Effective properties for a normal incidence

In this section, the effective properties involved in the S-parameters for normal incidences will be characterized specifically for Model 4 in Figure 3.2 since the properties for the other models can be determined just through the same procedure done in the conventional method. Before showing the results, the analytic relations between the S-parameters and the homogenized material properties will be derived here for 2D elastic metamaterials specifically at a normal wave incidence.

The Christoffel equation described in Eqs. (2.20-21) can be simplified to as follows for propagating waves in the x - y plane:

$$k^2 \mathbf{\Gamma} \begin{bmatrix} u_x \\ u_y \end{bmatrix} = \rho \omega^2 \begin{bmatrix} u_x \\ u_y \end{bmatrix} \quad (3.31)$$

where

$$\begin{aligned} \Gamma_{11} &= C_{11}n_x^2 + C_{66}n_y^2 + 2C_{16}n_xn_y \\ \Gamma_{22} &= C_{66}n_x^2 + C_{22}n_y^2 + 2C_{26}n_xn_y \\ \Gamma_{12} &= C_{16}n_x^2 + C_{26}n_y^2 + (C_{12} + C_{66})n_xn_y. \end{aligned} \quad (3.32)$$

Specifically for the propagating wave exhibiting the zero value of the y -directional wavenumber as $kn_y = 0$, the Christoffel equation in Eqs. (3.31-32) becomes

$$\begin{bmatrix} C_{11}k_x^2 - \rho\omega^2 & C_{16}k_x^2 \\ C_{16}k_x^2 & C_{66}k_x^2 - \rho\omega^2 \end{bmatrix} \begin{bmatrix} u_x \\ u_y \end{bmatrix} = 0 \quad (3.33)$$

where the non-trivial solutions yield the four x -directional wavenumbers k_x among which two correspond to the quasilongitudinal waves while the other two, to the quasitransverse waves as

$$\alpha^\pm = \pm \left[\frac{\rho\omega^2 (C_{11} + C_{66}) - \rho\omega^2 \sqrt{(C_{11} - C_{66})^2 + 4C_{16}^2}}{2(C_{11}C_{66} - C_{16}^2)} \right]^{1/2} \quad (3.34)$$

$$\beta^\pm = \pm \left[\frac{\rho\omega^2 (C_{11} + C_{66}) + \rho\omega^2 \sqrt{(C_{11} - C_{66})^2 + 4C_{16}^2}}{2(C_{11}C_{66} - C_{16}^2)} \right]^{1/2}. \quad (3.35)$$

The x -directional wavenumbers α^+ and α^- in Eq. (3.34) usually represent the wavenumbers for the quasilongitudinal waves propagating in the positive- and negative- x directions respectively while β^+ and β^- in Eq. (3.35), the wavenumbers for the quasitransverse waves respectively.

The polarization vectors for the quasilongitudinal ($\mathbf{P}^\alpha = P_x^\alpha \hat{\mathbf{x}} + P_y^\alpha \hat{\mathbf{y}}$) and the quasitransverse ($\mathbf{P}^\beta = P_x^\beta \hat{\mathbf{x}} + P_y^\beta \hat{\mathbf{y}}$) wave modes can be defined as follows from Eq. (3.31):

$$P_x^{k_x} = \frac{X_{k_x}}{\sqrt{1 + |X_{k_x}|^2}} \quad (3.36)$$

$$P_y^{k_x} = \frac{1}{\sqrt{1 + |X_{k_x}|^2}} \quad (3.37)$$

where

$$X_{k_x} = -\frac{C_{16}k_x^2}{C_{11}k_x^2 - \rho\omega^2} = \frac{C_{66}k_x^2 - \rho\omega^2}{C_{16}k_x^2} \quad (k_x = \alpha^\pm, \beta^\pm). \quad (3.38)$$

Now, the detail components in the matrices \mathbf{M} and \mathbf{N} will be investigated using Eqs.

(2.35-36). Substituting the condition $\sigma = 0$ into Eqs. (2.35-36) while employing the definitions of the x -directional wavenumbers described in Eqs. (3.34-35) yields the following simplified \mathbf{M} and \mathbf{N} specifically for the propagating waves exhibiting the zero value of the y -directional wavenumber:

$$\begin{aligned}
M_{11} &= -j\omega P_x^\beta, & M_{12} &= -j\omega P_x^\alpha, & M_{13} &= -j\omega P_x^\alpha, & M_{14} &= -j\omega P_x^\beta, \\
M_{21} &= -j\omega P_y^\beta, & M_{22} &= -j\omega P_y^\alpha, & M_{23} &= -j\omega P_y^\beta, & M_{24} &= -j\omega P_y^\alpha, \\
M_{31} &= j\beta^+ (C_{11}P_x^\beta + C_{16}P_y^\beta), & M_{32} &= j\alpha^+ (C_{11}P_x^\alpha + C_{16}P_y^\alpha), \\
M_{33} &= j\alpha^- (C_{11}P_x^\alpha + C_{16}P_y^\alpha), & M_{34} &= j\beta^- (C_{11}P_x^\beta + C_{16}P_y^\beta), \\
M_{41} &= j\beta^+ (C_{16}P_x^\beta + C_{66}P_y^\beta), & M_{42} &= j\alpha^+ (C_{16}P_x^\alpha + C_{66}P_y^\alpha), \\
M_{43} &= j\alpha^- (C_{16}P_x^\alpha + C_{66}P_y^\alpha), & M_{44} &= j\beta^- (C_{16}P_x^\beta + C_{66}P_y^\beta),
\end{aligned} \tag{3.39}$$

and

$$\mathbf{N} = \begin{bmatrix} e^{j\beta^+x} & 0 & 0 & 0 \\ 0 & e^{j\alpha^+x} & 0 & 0 \\ 0 & 0 & e^{j\alpha^-x} & 0 \\ 0 & 0 & 0 & e^{j\beta^-x} \end{bmatrix}. \tag{3.40}$$

with the polarization vectors \mathbf{P}^α and \mathbf{P}^β defined in Eqs. (3.36-37).

For the case where the general anisotropic solid slab is sandwiched by isotropic materials at $x=0$ and d just as considered in Section 3.1, the matrix \mathbf{S} in Eq. (2.44) becomes

$$\mathbf{S} = (\mathbf{M}_0)^{-1} \mathbf{T} \mathbf{M}_0 = (\mathbf{M}_0)^{-1} (\mathbf{M} \mathbf{N}|_{x=d} \mathbf{M}^{-1}) \mathbf{M}_0 \tag{3.41}$$

where \mathbf{M}_0 represent the matrix \mathbf{M} defined in Eq. (3.39) but for the surrounding

isotropic materials. Substituting \mathbf{S} into Eqs. (2.46-47) yields the following S-parameters of the anisotropic solid slab for x -directional normal wave incidences:

$$RLL = \frac{S_{41}S_{24} - S_{21}S_{44}}{S_{22}S_{44} - S_{42}S_{24}}, \quad (3.42a)$$

$$RLT = \frac{S_{42}S_{21} - S_{22}S_{41}}{S_{22}S_{44} - S_{42}S_{24}}, \quad (3.42b)$$

$$SLL = S_{11} + S_{12}RLL + S_{14}RLT, \quad (3.42c)$$

$$SLT = S_{31} + S_{32}RLL + S_{34}RLT \quad (3.42d)$$

for a longitudinal wave incidence while

$$RTL = \frac{S_{43}S_{24} - S_{23}S_{44}}{S_{22}S_{44} - S_{42}S_{24}}, \quad (3.43a)$$

$$RTT = \frac{S_{42}S_{23} - S_{22}S_{43}}{S_{22}S_{44} - S_{42}S_{24}}, \quad (3.43b)$$

$$STL = S_{12}RTL + S_{13} + S_{14}RTT, \quad (3.43c)$$

$$STT = S_{32}RTL + S_{33} + S_{34}RTT \quad (3.43d)$$

for a transverse wave incidence. When the stiffness component C_{16} , involved with an extension-shear coupling has the non-zero value, the S-parameters including SLT (STL) and RLT (RTL) (wave mode conversion ratios) will exist as shown in Figure 3.3(b), the result for Model 4.

As shown in Eqs. (3.31-43), the S-parameters for normal incidences are totally defined by the material parameters ρ , C_{11} , C_{16} , and C_{66} . So, once the S-parameters of a metamaterial slab are measured at ω , the effective properties specifically ρ , C_{11} , C_{16} , and C_{66} can be inversely estimated in this procedure even for the metamaterials having the material axes not aligned with the coordinate

axes. Note that the number of the effective properties involved in the S-parameters for normal incidences is smaller than the number of the S-parameters as presented in Table 3.2, so the properties can be sufficiently determined. For the retrieval procedure, the Gauss-Newton algorithm [105] is employed to extract the properties for the specific values of the S-parameters.

Figure 3.6 shows the retrieved effective properties of Model 4 with $w = 0.2$ mm, $h = 5$ mm, $\theta_{\text{rot}} = 45^\circ$ and $L_x = L_y = 6$ mm, which are involved in the S-parameters for normal wave incidences. Specifically at 30 kHz, the properties are observed to be $\rho = 2614$ kg/m³ while $C_{11} = 5.23 \times 10^{10}$, $C_{16} = 1.43 \times 10^{10}$, and $C_{66} = 2.10 \times 10^{10}$ N/m² (the validation shall be shown in the following section). Even for the present model having the tilted material axes, the proposed method successfully yields the effective properties.

Here, it may worth remarking on why the retrieval method is highly required for the metamaterials having the tilted material axes. In earlier studies, this type of metamaterials is usually characterized by using the coordinate transformation [44, 45, 98]; for example, the stiffness of Model 4 ($\theta_{\text{rot}} \neq 0$) is usually assumed to be equal to the stiffness of Model 3 (having the identically-configured constituent element with it in Model 4 but $\theta_{\text{rot}} = 0$) when the coordinate transformation by θ_{rot} is applied to it.

See Figures 3.7(a, b) where the EFCs for Models 3 and 4 are shown respectively, which are calculated through the FEM solving the eigenvalues under the periodic boundary conditions. In order to investigate the simple coordinate transformation is valid for estimating the effective properties of Model 4 by using them of Model 3,

the rotated EFC for Model 3 (black solid lines) is compared to it for Model 4 in Figure 3.7(b). Even though the rotated EFC for a quasilongitudinal wave (located at the inner side in the plot) fairly coincide to the corresponding EFC for Model 3, the EFCs for a quasitransverse wave (at the outer side) show a significant discrepancy between each other. It means that the simple coordinate transformation does not always work for characterizing the metamaterials having the tilted material axes. The result signifies that the proposed S-parameter retrieval method covering general anisotropic metamaterials is highly required.

3.2.3 Effective properties for an oblique incidence

In the retrieval procedure using the S-parameters for oblique incidences, the rest of effective properties will be determined after adopting the properties obtained from the S-parameters for normal incidences. Specifically for the 2D metamaterial models depicted in Figure 3.2, the properties including C_{12} , C_{22} and C_{26} will be defined in this procedure (Step 2) by using ρ , C_{11} , C_{16} , and C_{66} already obtained in the previous procedure (Step 1).

Note again that the proposed two-step retrieval method is valid only when metamaterials exhibit the local responses, i.e., when the effective material parameters (ρ and \mathbf{C}) are consistent regardless of a varying incident angle. This assumption enables only the rest of the properties to be determined from the S-parameters for oblique incidences. If metamaterials exhibit the nonlocal responses, the whole properties should be defined for a varying incident angle, which also can be done through the procedure to be explained in this section. Here, the cases exhibiting the local responses are considered only.

In order to measure the S-parameters of a metamaterial slab for oblique wave incidences, the wave fields around the slab are simulated in COMSOL Multiphysics 3.5a by using the same setups as illustrated in Figure 3.1(b) but for oblique incidences ($\theta_{\text{inc}} \neq 0^\circ$). The setups are shown in Figure 3.8(a). The simulation results for the incident, scattered, and total wave fields specifically at $\theta_{\text{inc}} = 30^\circ$ and 60° are also shown in Figures 3.8(b, c) respectively after indicating them by the x -directional velocity components v_x . Here, the metamaterial slab consisting of a single-period unit cell in the x -direction is used again after confirming the bulk property of the metamaterial [35, 94].

The analytic relations between the S-parameters and the homogenized material properties for an oblique incidence can be derived just in the same procedure as demonstrated in Section 3.2.2. Here, it shall be briefly commented for the 2D metamaterial models:

- (1) the x -directional wavenumbers and the polarization vectors of the propagating waves in a general anisotropic solid material are obtained through the Christoffel equation at given k_y (the y -directional wavenumber) and ω by using Eqs. (3.31-32),
- (2) after determining the matrices \mathbf{M} and \mathbf{N} for the anisotropic material while \mathbf{M}_0 for the surrounding isotropic solid materials, the matrix \mathbf{S} is derived as described in Eq. (3.41),
- (3) the S-parameters are determined through using the components in \mathbf{S} as described in Eqs. (3.42-43).

Here, it may worth reminding the Christoffel equation in Eqs. (3.31-32) as

$$k^2 \mathbf{\Gamma} \begin{bmatrix} u_x \\ u_y \end{bmatrix} = \rho \omega^2 \begin{bmatrix} u_x \\ u_y \end{bmatrix}$$

where

$$\Gamma_{11} = C_{11}n_x^2 + C_{66}n_y^2 + 2C_{16}n_xn_y$$

$$\Gamma_{22} = C_{66}n_x^2 + C_{22}n_y^2 + 2C_{26}n_xn_y$$

$$\Gamma_{12} = C_{16}n_x^2 + C_{26}n_y^2 + (C_{12} + C_{66})n_xn_y.$$

See the stiffness component C_{22} , which appears only in Γ_{22} . Remarking that C_{22} does not appear in the matrices \mathbf{M} and \mathbf{N} at all as shown in Eqs. (2.35-36), it should less influence on the S-parameters than the other components do. Furthermore, when considering the component exists multiplied by n_y^2 (the square of the y-directional cosine), its influence on the S-parameters should become significantly weak when the incident angle, θ_{inc} is small. It means that the choice of θ_{inc} is important for the retrieval procedure especially for determining C_{22} by using the S-parameters for oblique incidences. For this reason, the degree of θ_{inc} should be chosen somewhat large while avoiding the critical angles, which usually leads to a large numerical error.

After adopting the effective properties already retrieved from normal incidences (ρ , C_{11} , C_{16} , and C_{66} for the present 2D case) as demonstrated in the previous section, the rest of the stiffness components (specifically C_{12} , C_{22} and C_{26}) will be determined in the procedure using an oblique incidence. Note that the number of the stiffness components to be determined in this procedure is also smaller than that of the S-parameters even if the components are assumed to get the complex values, so they can be sufficiently well determined. For the retrieval procedure, the Gauss-

Newton algorithm [105] is used again.

In Figure 3.9, the whole effective properties of Models 1-4 are presented for the following geometric parameters:

- (a) Model 1: $r = 1$ mm,
- (b) Model 2: $w = h = 2$ mm,
- (c) Model 3: $w = 0.2$ mm and $h = 5$ mm,
- (d) Model 4: $w = 0.2$ mm, $h = 5$ mm, and $\theta_{\text{rot}} = 0$

while the lattice constants for the x - and y -directions are all set to be $L_x = L_y = 6$ mm. The first and second plots in each figure show ρ and the stiffness components including C_{11} , (C_{16} ,) and C_{66} respectively, which are retrieved from normal incidences while the third shows C_{12} , (C_{22} ,) and C_{26} , which are from an oblique incidence specifically at $\theta_{\text{inc}} = 50^\circ$. Even for Model 4, the whole material parameters are successfully determined.

The detail effective properties are as follows at 30 kHz:

$$\rho = 2460 \text{ kg/m}^3 \text{ and } \mathbf{C} = \begin{bmatrix} 7.84 & 3.52 & 0 \\ & 7.86 & 0 \\ \text{sym} & & 2.07 \end{bmatrix} \times 10^{10} \text{ N/m}^2 \text{ for Model 1,}$$

$$\rho = 2390 \text{ kg/m}^3 \text{ and } \mathbf{C} = \begin{bmatrix} 6.96 & 2.78 & 0 \\ & 7.06 & 0 \\ \text{sym} & & 1.71 \end{bmatrix} \times 10^{10} \text{ N/m}^2 \text{ for Model 2,}$$

$$\rho = 2600 \text{ kg/m}^3 \text{ and } \mathbf{C} = \begin{bmatrix} 3.03 & 1.48 & 0 \\ & 8.50 & 0 \\ \text{sym} & & 1.41 \end{bmatrix} \times 10^{10} \text{ N/m}^2 \text{ for Model 3,}$$

$$\rho = 2610 \text{ kg/m}^3 \text{ and } \mathbf{C} = \begin{bmatrix} 5.23 & 1.85 & 1.43 \\ & 5.39 & 1.38 \\ \text{sym} & & 2.10 \end{bmatrix} \times 10^{10} \text{ N/m}^2 \text{ for Model 4.}$$

From the results, the following observations can be remarked:

- (1) for Models 1 and 2, the values of C_{11} and C_{22} are fairly identical; they should be in the case where the models exhibit the local responses since the geometries of the constituent inhomogeneity are circular and square respectively,
- (2) for Model 1, $(C_{11} - C_{12})/2 = 2.16 \times 10^{10}$ while $C_{66} = 2.07 \times 10^{10} \text{ N/m}^2$, which indicates Model 1 is close to isotropic as shown in Figure 3.5(a),
- (3) for Models 3 and 4, the effective mass densities are fairly identical; they should be when considering the mass density usually depends on the volume fraction of the substrate for the present cases,
- (4) for Model 3, $C_{22}/C_{11} \approx 2.6$, which indicates that the values of the diagonal stiffness components for the models depend inversely on the degree of wave interruptions by the constituent inhomogeneity along the corresponding directions,
- (5) for Model 4, $C_{11} \approx C_{22}$ while $C_{16} \approx C_{26}$; they should be since the slit-shaped inhomogeneity lies in the direction rotated by 45° with respect to the coordinate axes,
- (6) the following coordinate-transformed stiffness tensor for Model 3 by the 45° rotation is not identical to the stiffness for Model 4 as already mentioned in Figure 3.7:

$$\mathbf{C} = \begin{bmatrix} 5.03 & 2.21 & 1.37 \\ & 5.03 & 1.37 \\ \text{sym} & & 2.14 \end{bmatrix} \times 10^{10} \text{ N/m}^2$$

- (7) from the above observations, Model 1 is close to transversely isotropic while Models 2, 3, and 4 are tetragonal, orthotropic, and monoclinic respectively.

3.2.4 Validation of retrieved effective properties

The proposed two-step retrieval procedure is shown to possibly yield the whole effective properties of elastic metamaterials even if they have the material principal axes not aligned with the coordinate axes. Here, the validations of the retrieved properties will be performed specifically for the metamaterial models presented in Figure 3.9.

First, the validations are implemented by using the EFCs. Figure 3.10 shows the EFCs for Models 1-4; the EFCs indicated by black solid lines are calculated after substituting the retrieved properties into the Christoffel equation described in Eqs. (3.31-32), i.e., by using the effective medium, while those indicated by magenta dots are by using the FEM solving the eigenvalue problem on the detailed models. As seen in the results, they are fairly identical with each other for every model. When looking at the degrees of anisotropy for the models, they are confirmed to effectively work as transversely isotropic, tetragonal, orthotropic, and monoclinic materials, respectively.

Not that Model 4 having the tilted material axes with respect to the coordinate axes is also successfully characterized for the effective medium by directly extracting the properties from the S-parameters not by using the coordinate transformation. The result for Model 4 exhibits slight discrepancies compared to those for the other

models, which may originate from the lack of the bulk property [37, 93, 94].

Secondly, the validations are done by analyzing the wave fields around the metamaterial slabs for the wave incidences at the specific angles. The results specifically for Models 3 and 4 are presented in Figures 3.11(a, b) respectively after calculating the fields by using the detailed models and their effective medium models both under the same simulation setups illustrated in Figure 3.8. The results are indicated by the x -directional velocity components (v_x). The wave fields from the detailed and the effective medium models show excellent agreements and it means that the metamaterial slabs do successful roles as homogeneous anisotropic materials.

Lastly, the validations are conducted by calculating the S-parameters employing the detailed and the effective medium models. In Figures 3.12(a, b), the S-parameters of Models 3 and 4 are shown respectively for a varying incident angle with black solid lines for the effective medium models while with magenta dots for the detailed models. The results also confirm that the retrieved properties are fairly accurate and they well demonstrate the behaviors of the metamaterials.

In Table 3.3, the retrievable and the non-retrievable stiffness components (elastic constants) are listed for the metamaterial models when using the improved version of the S-parameter retrieval method. Not only the diagonal components but also the non-diagonal terms are successfully obtained for every model even for Model 4 having the tilted material axes.

3.3 Issues in the S-Parameter Retrieval Method for Elastic Metamaterials

In this section, some issues in the S-parameter retrieval method will be briefly introduced specifically when it is applied for characterizing elastic metamaterials. In elasticity, wave propagation characteristics are somewhat different with those in electromagnetics or acoustics; the two wave modes including longitudinal and transverse wave modes exist in a bulk medium, the mode conversion between the two modes exist, the scattering phenomena by inhomogeneities are complex compared to those in other areas. Due to the unique physics in elasticity, the retrieval method should additionally cover the shear and the extension-shear coupling components in the stiffness tensor and more carefully check the bulk property of metamaterials. Among the issues, the issue on the bulk property will be reviewed here, which are covered in earlier works [35, 36, 92-94].

Specifically the elastic metamaterials are not guaranteed to satisfy the bulk property even they consist of simple and subwavelength elements due to the significant and complex scattering phenomena around the constituent elements. The intrinsic scattering phenomena sometimes lead the interactions among the adjacent metamaterial unit cells to be strong and the effective material parameters to largely depend on the periodicity condition. In this case, the number of unit cell periods should be considered for extracting the exact properties.

See Figures 13(a, b) where the effective properties of Models 1 and 2 are presented respectively for the geometric parameters as $r = 2 \text{ mm}$ for Model 1 and $w = h = 3 \text{ mm}$ for Model 2 with the lattice constants as $L_x = L_y = 6 \text{ mm}$ for each. The sizes of the inhomogeneity are larger than those considered in Figure 3.9 but still significantly smaller than the wavelength. Here the material parameters are extracted by using the two sets of the S-parameters: one set from the metamaterial

slab with a single period of the unit cell in the x -direction and the other set from the slab with the four periods. The material parameters from the two sets are denoted by $\rho^{(1)}$ and $\mathbf{C}^{(1)}$ while $\rho^{(4)}$ and $\mathbf{C}^{(4)}$, respectively in the figure while the values are indicated by dots and grey solid lines respectively.

The two sets of properties show large discrepancies as the frequency increases, and the discrepancy is observed significant especially for the effective mass densities between $\rho^{(1)}$ and $\rho^{(4)}$. The results signify that the present models do not satisfy the bulk property and their effective properties change depending on the period numbers specifically when they consist of the small-period unit cells.

After defining the effective medium model possessing the effective properties, $\rho^{(1)}$ and $\mathbf{C}^{(1)}$ as EM⁽¹⁾ model while it possessing $\rho^{(4)}$ and $\mathbf{C}^{(4)}$ as EM⁽⁴⁾ model, the EFCs for the models are drawn for Models 1 and 2 in Figures 3.14(a, b), respectively; the EFC for EM⁽¹⁾ model is marked by grey solid line while it for EM⁽⁴⁾ model, by black. In each figure, the EFCs for the detailed models calculated using the FEM solving the eigenvalue problems under the periodic boundary condition are also shown with magenta dots.

The EFC profiles for EM⁽¹⁾ and EM⁽⁴⁾ models are observed to significantly differ between each other as already seen in Figure 3.13 while the profile for EM⁽⁴⁾ model well corresponds to it for the detailed model. It means that in the present cases with the period number approximately above four, the metamaterial slabs sufficiently cover the interactions among the adjacent unit cells and they satisfy the bulk property. With the period number below four, however, the slabs do not cover the interactions and the material properties should vary depending on the period number.

So, when describing the wave propagation characteristics in bulk metamaterial slabs through the effective media, the sufficient period number should be considered in the retrieval procedure after confirming the bulk property. Note that the issue also can be overcome by employing the inhomogeneity assumption, which are well covered in [37].

3.4 Summary

The improved S-parameter retrieval method is proposed in this chapter for characterizing the elastic anisotropic metamaterials. In elasticity, metamaterials should possess the effective stiffness tensor, which is composed with not only the diagonal components but also the non-diagonal components unlike the other tensorial material parameters in electromagnetics and acoustics do. So, the conventional retrieval method using normal wave incidences only cannot yield the whole constitutive parameters. In order to overcome the limitation, the two-step retrieval procedure is proposed, which uses normal incidences for determining the properties involved in the S-parameters (specifically ρ , C_{11} , C_{16} , and C_{66} for 2D cases in the x - y plane) as well as an oblique incidence for determining the rest of the properties (specifically C_{12} , C_{22} and C_{26}). The proposed method is shown to successfully work even for the metamaterials which possess the tilted material principal axes with respect to the coordinate axes.

The main contributions of this study are three folds. First, the S-parameter retrieval method which enables the characterization of the whole material parameters for elastic anisotropic metamaterials is first proposed. Secondly, the analytic relations between the S-parameters and the constitutive material parameters for normal and

oblique incidences are reviewed first in the elastic metamaterial area. Thirdly, the validations are successfully implemented for the anisotropic metamaterials possessing various symmetry planes. The proposed retrieval method is expected to be widely utilized specifically in the elastic regime.

Conventional S-parameter retrieval method

	Elastic constants	Retrievable elastic constants	Non-retrievable elastic constants
Model 1	$C_{11}, C_{12}, C_{22}, C_{66}$	C_{11}, C_{66}, C_{22} (cell rotation required), sometimes C_{12} (additional technique required)	usually C_{12}
Models 2, 3	$C_{11}, C_{12}, C_{22}, C_{66}$	C_{11}, C_{66}, C_{22} (cell rotation required)	C_{12}
Model 4	$C_{11}, C_{12}, C_{16}, C_{22}, C_{26}, C_{66}$	none	$C_{11}, C_{12}, C_{16}, C_{22}, C_{26}, C_{66}$

Table 3.1 The retrievable and non-retrievable elastic constants for Models 1-4 by using conventional S-parameter retrieval method

	Effective properties (EPs)	S-parameters and the EPs involved, for normal incidences		S-parameters and the EPs involved, for oblique incidences	
		S-parameters	EPs	S-parameters	EPs
Models 1-3	$\rho,$ $C_{11}, C_{12},$ C_{22}, C_{66}	RLL, SLL (longitudinal wave) RTT, STT (transverse wave)	$\rho,$ C_{11}, C_{66}	$RLL, RLT,$ SLL, SLT (longitudinal wave) $RTL, RTT,$ STL, STT (transverse wave)	$\rho,$ $C_{11}, C_{66},$ C_{12}, C_{22}
Model 4	$\rho,$ $C_{11}, C_{12}, C_{16},$ C_{22}, C_{26}, C_{66}	$RLL, RLT,$ SLL, SLT (longitudinal wave) $RTL, RTT,$ STL, STT (transverse wave)	$\rho,$ $C_{11}, C_{16},$ C_{66}	$RLL, RLT,$ SLL, SLT (longitudinal wave) $RTL, RTT,$ STL, STT (transverse wave)	$\rho,$ $C_{11}, C_{16},$ $C_{66}, C_{12},$ C_{22}, C_{26}

Table 3.2 The S-parameters for normal and oblique incidences which are valid for characterizing the effective properties of Models 1-4, and the effective properties involved in them

Proposed S-parameter retrieval method

	Elastic constants	Retrievable elastic constants	Non-retrievable elastic constants
Model 1	$C_{11}, C_{12}, C_{22}, C_{66}$	$C_{11}, C_{12}, C_{22}, C_{66}$	None
Models 2, 3	$C_{11}, C_{12}, C_{22}, C_{66}$	$C_{11}, C_{12}, C_{22}, C_{66}$	None
Model 4	$C_{11}, C_{12}, C_{16}, C_{22}, C_{26}, C_{66}$	$C_{11}, C_{12}, C_{16}, C_{22}, C_{26}, C_{66}$	None

Table 3.3 The retrievable and non-retrievable elastic constants for Models 1-4 by using proposed S-parameter retrieval method

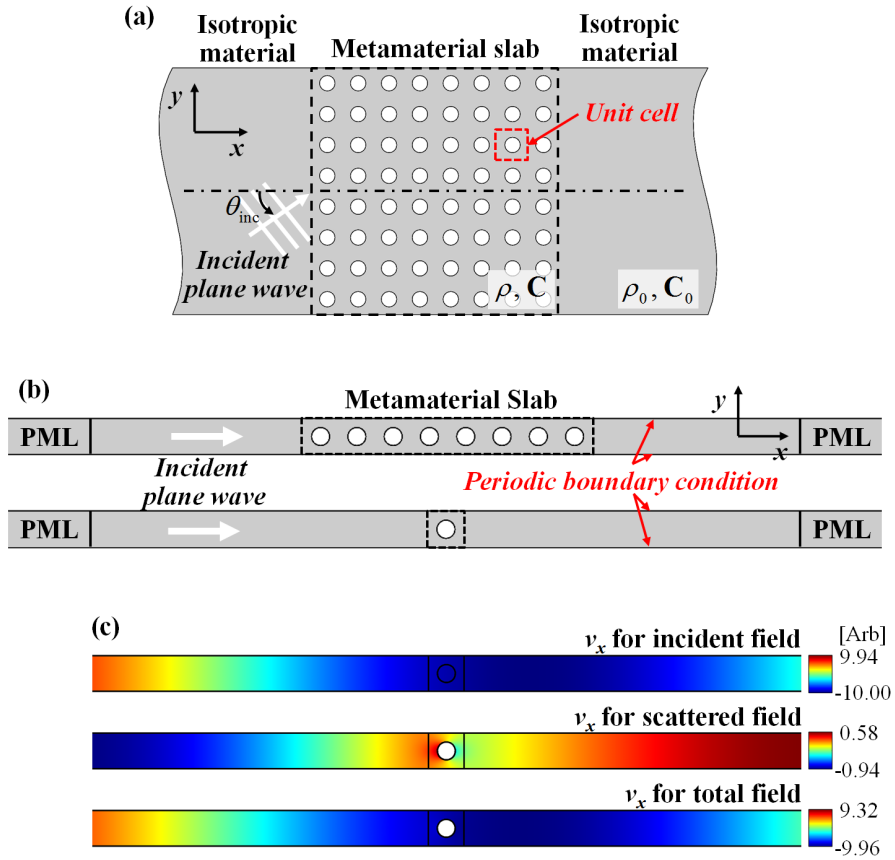


Figure 3.1 (a) The schematic picture for a metamaterial slab sandwiched by isotropic substances and (b) the simulation setups for measuring the scattering parameters of a metamaterial slab for a normal incidence (c) with the results

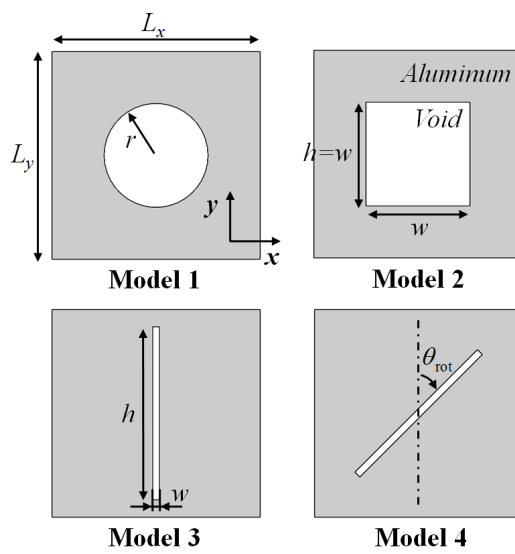
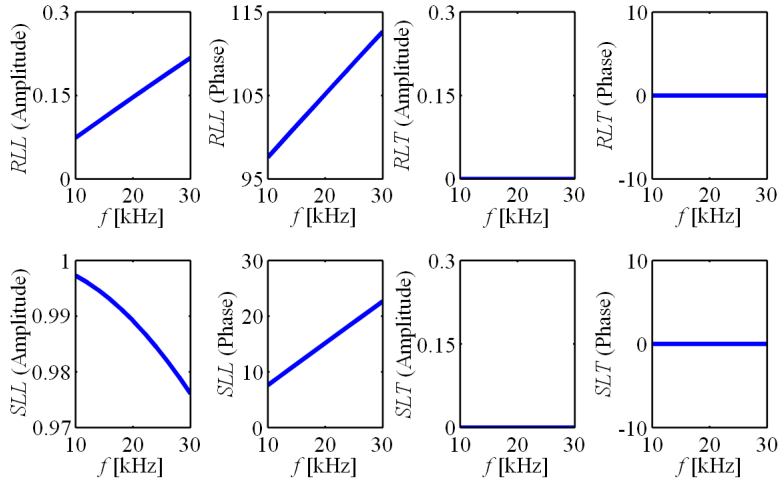


Figure 3.2 The schematic configurations of the metamaterial models considered in this study

(a) S-parameters for Model 3



(b) S-parameters for Model 4

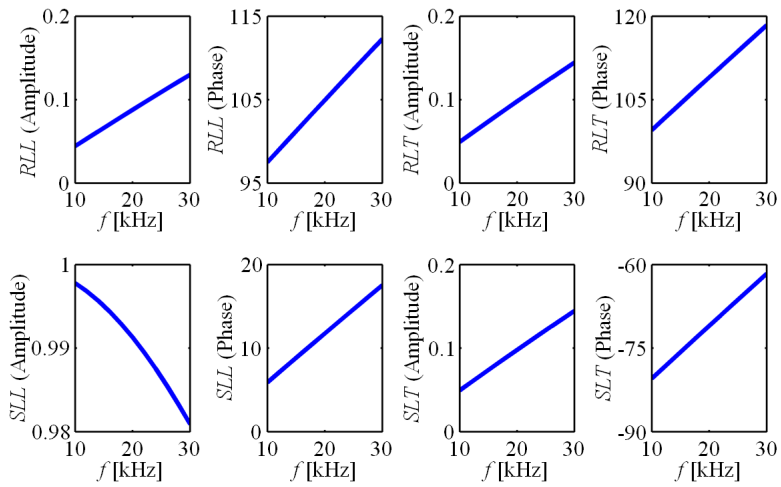
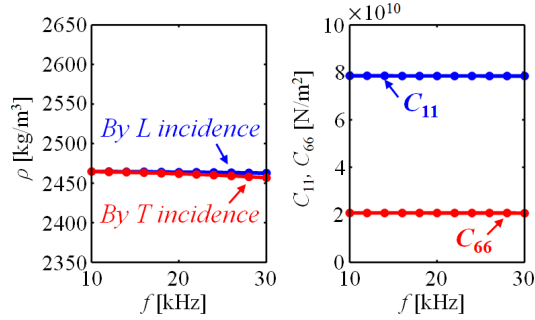
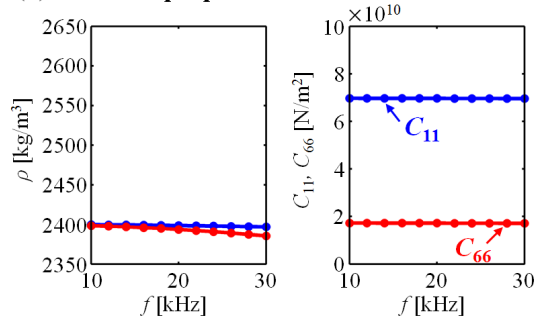


Figure 3.3 The scattering parameters of (a) Model 3 and (b) Model 4 for a normal longitudinal wave incidence

(a) Effective properties of Model 1



(b) Effective properties of Model 2



(c) Effective properties of Model 3

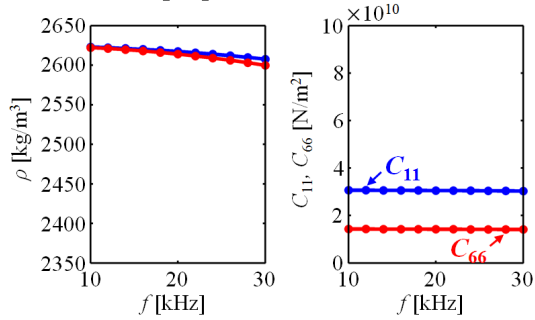
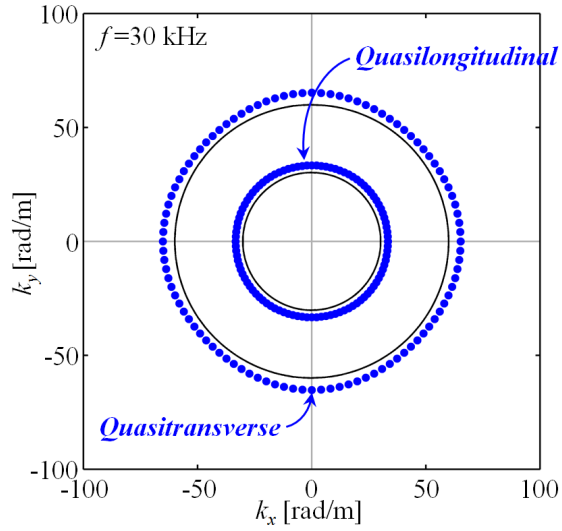


Figure 3.4 The effective properties of Models 1-3 (a-c) characterized by using the conventional S-parameter retrieval method

(a) EFC for Model 1 with $r=1.0$ mm



(b) EFC for Model 1 with $r=1.5$ mm

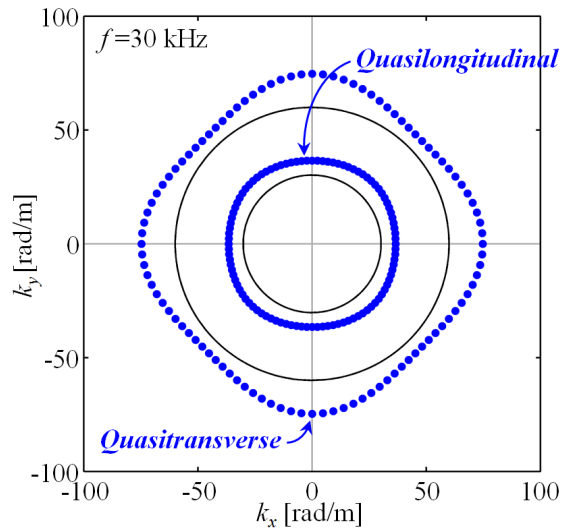


Figure 3.5 The EFCs for Model 1 with (a) $r=1.0$ mm and (b) 1.5 mm at 30 kHz

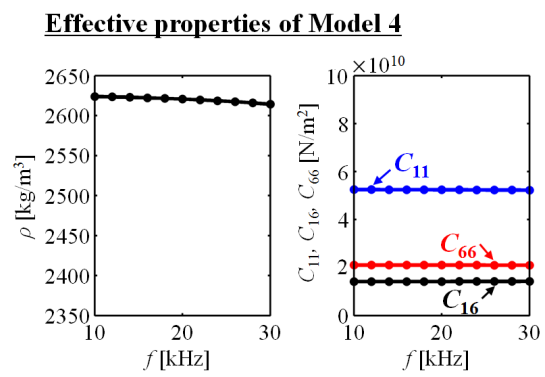
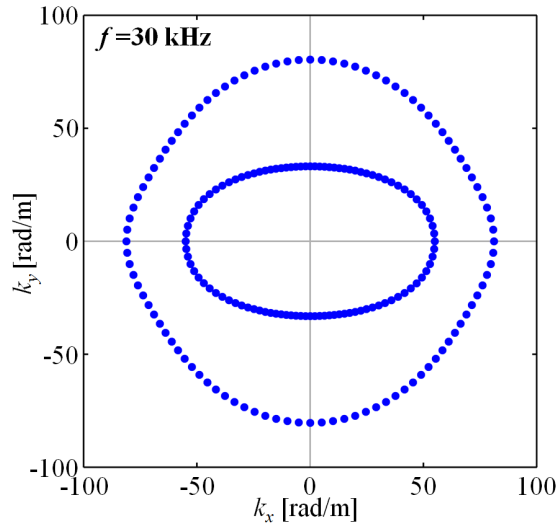


Figure 3.6 The effective properties of Model 4 characterized by using the proposed S-parameter retrieval method

(a) EFC for Model 3



(b) EFC for Model 4

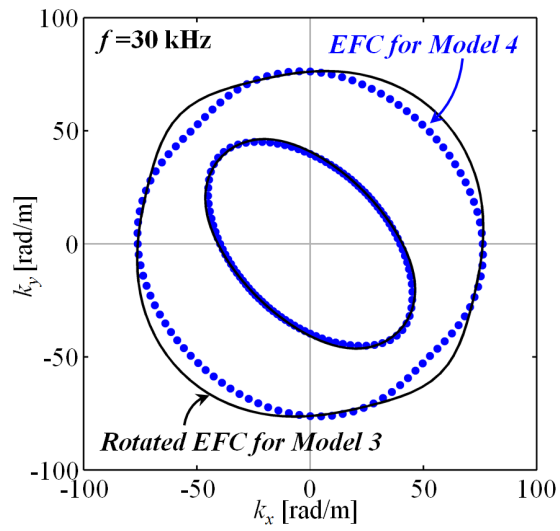


Figure 3.7 The EFCs for (a) Model 3 and (b) Model 4 at 30 kHz

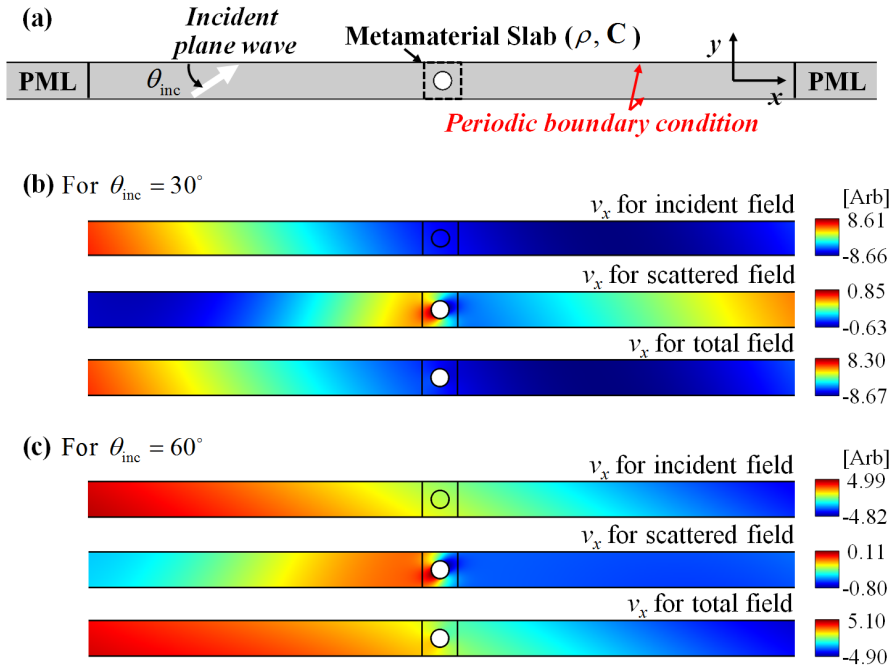
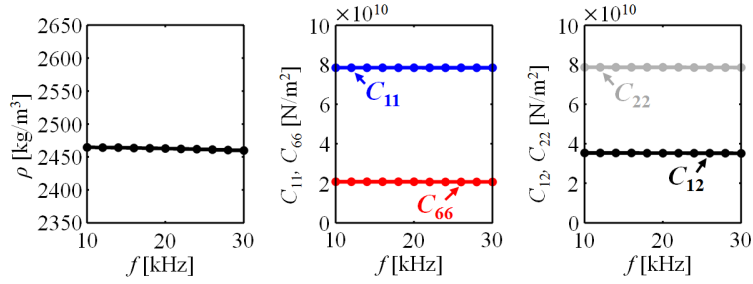
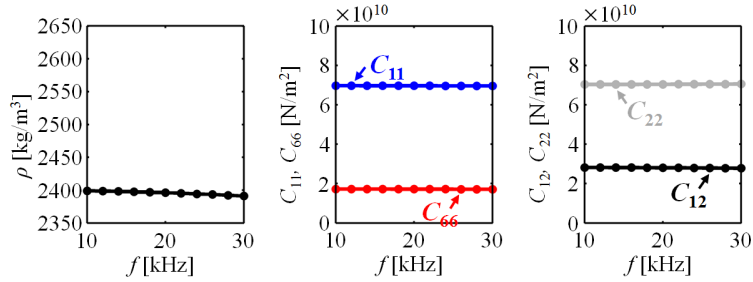


Figure 3.8 The simulation setups for measuring the scattering parameters for oblique incidences and the x -directional velocity fields for the oblique longitudinal wave incidences at $\theta_{\text{inc}} = 30^\circ$ and 60°

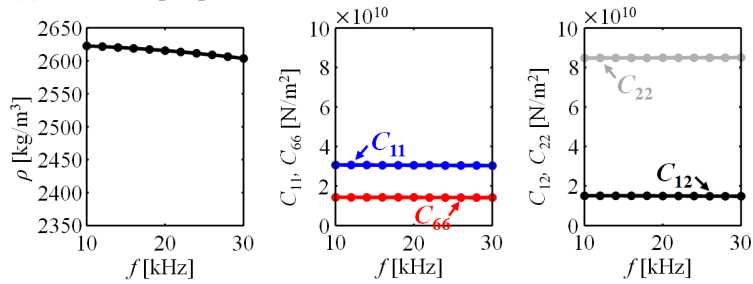
(a) Effective properties of Model 1



(b) Effective properties of Model 2



(c) Effective properties of Model 3



(d) Effective properties of Model 4

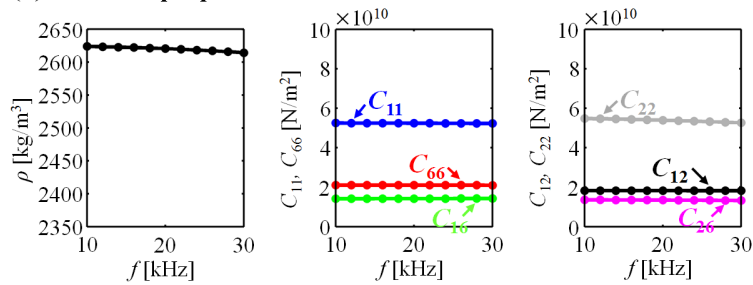
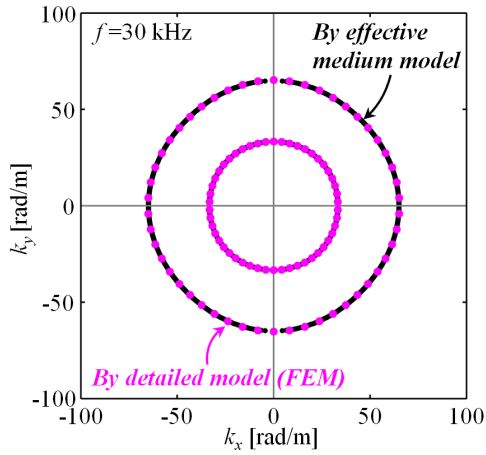
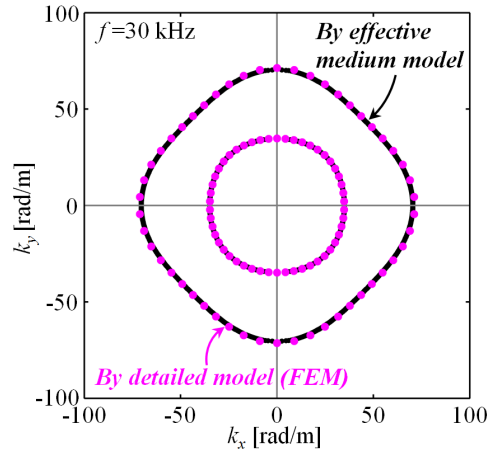


Figure 3.9 The effective properties of Models 1-4 (a-d) characterized by using the proposed S-parameter retrieval method

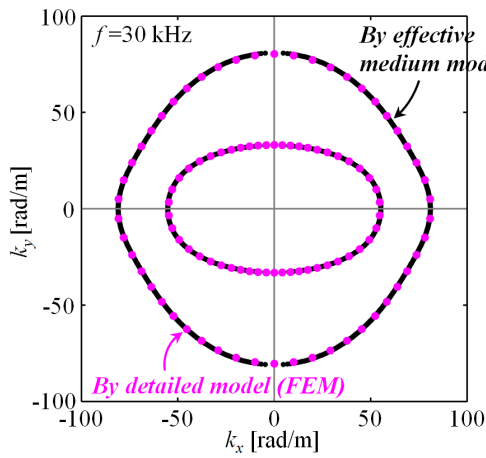
(a) EFC for Model 1



(b) EFC for Model 2



(c) EFC for Model 3



(d) EFC for Model 4

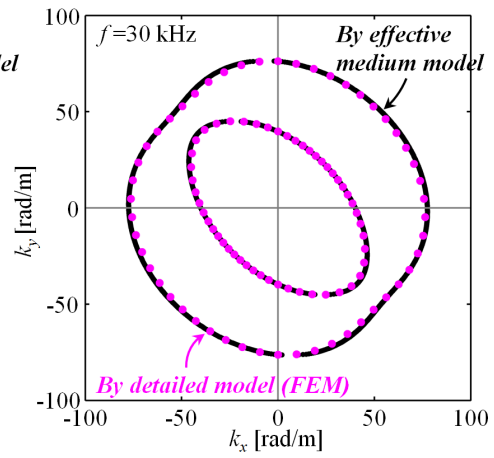
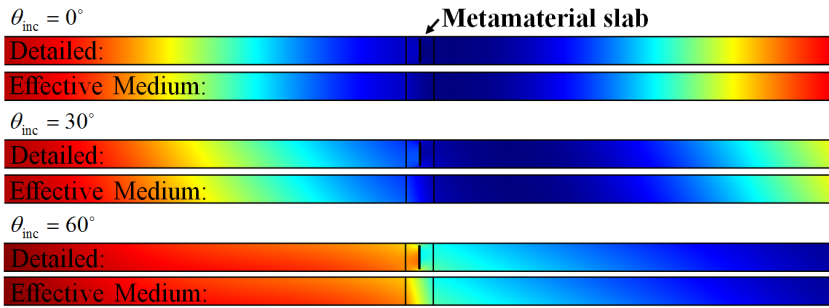


Figure 3.10 The EFCs for Models 1-4 (a-d) at 30 kHz analyzed by using the effective medium models (black solid line) and the detailed models (magenta dots)

(a) v_x fields at 30 kHz for Model 3



(b) v_x fields at 30 kHz for Model 4

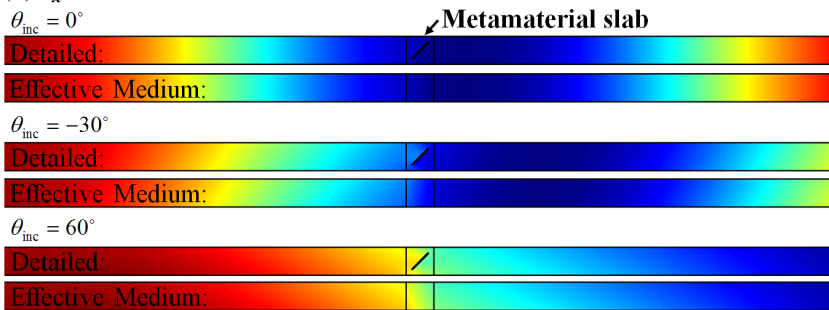
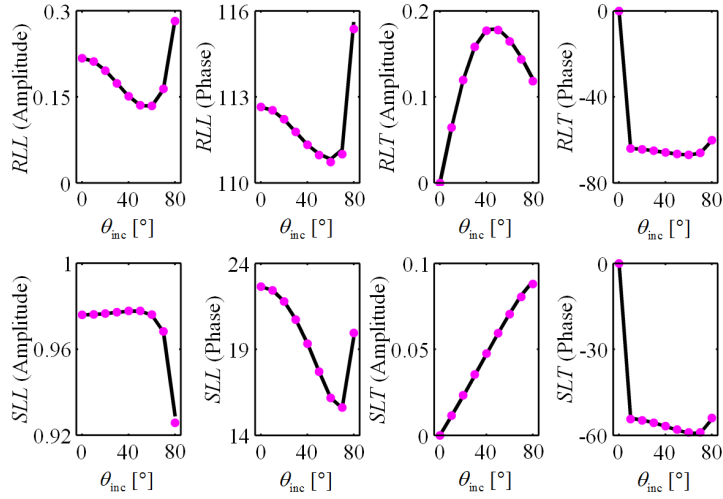


Figure 3.11 The x -directional velocity fields for oblique longitudinal wave incidences to the single slabs of (a) Model 3 and (b) Model 4 at the varying degree of θ_{inc} , simulated by the detailed models and the effective medium models

(a) S-parameters of Model 3

— : By effective medium model

● : By detailed model



(b) S-parameters of Model 4

— : By effective medium model

● : By detailed model

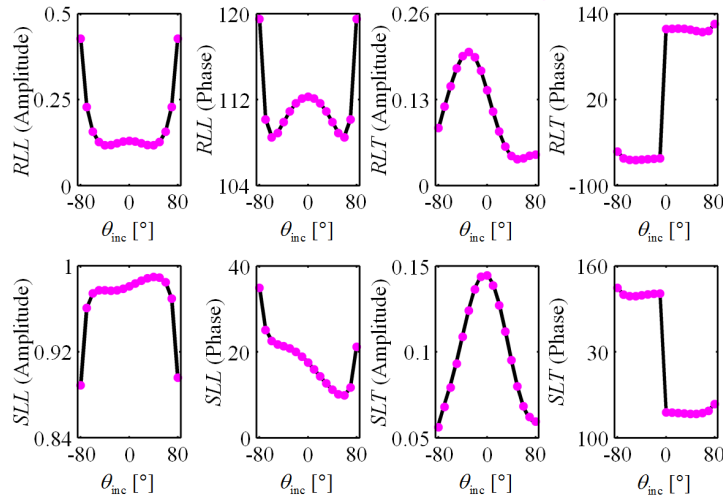
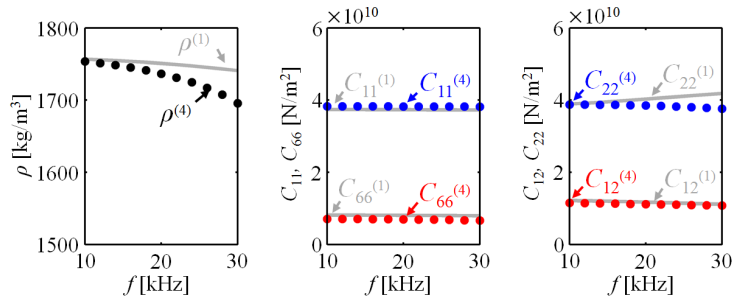


Figure 3.12 The scattering parameters of (a) Model 3 and (b) Model 4 for the longitudinal wave incidence at the varying degree of θ_{inc} , calculated by the detailed models and the effective medium models

(a) Effective properties of Model 1



(b) Effective properties of Model 2

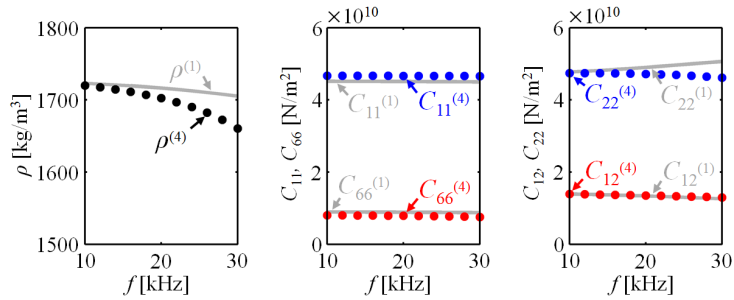
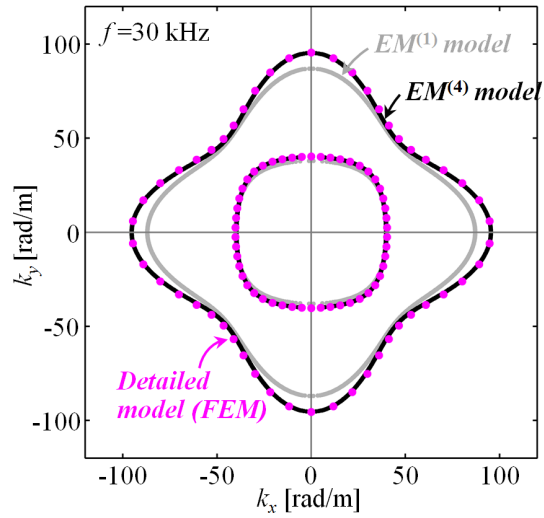


Figure 3.13 The effective properties of (a) Model 1 and (b) Model 2, calculated by using the scattering parameters obtained from the single (grey solid lines) and the four (dots) unit slabs

(a) EFC for Model 1



(b) EFC for Model 2

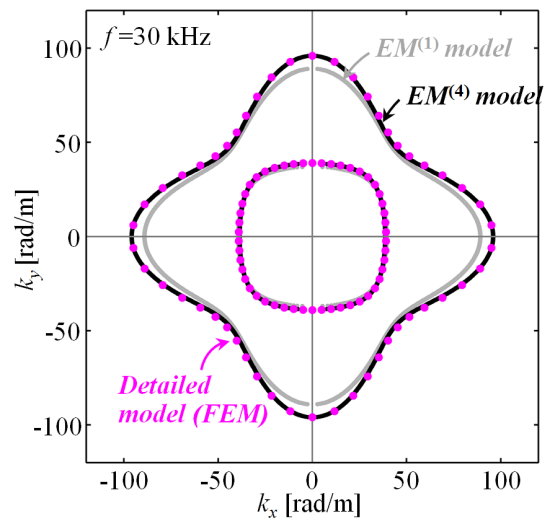


Figure 3.14 The EFCs for (a) Model 1 and (b) Model 2, calculated by using the effective properties obtained from the single (grey solid lines) and the four (black solid lines) unit slabs

CHAPTER 4.

Design of Elastic Magnifying Hyperlens for Sub-Wavelength Imaging by Using Extremely Anisotropic Metamaterials

4.1 Magnifying Hyperlens

Recent studies have shown that magnifying optical hyperlenses [16-18] are capable to overcome the diffraction limit in electromagnetics, the fundamental limit due to the exponentially decaying wave components containing the subwavelength informations of a imaging object [10, 17, 54, 106, 107]. Hyperlenses convert the evanescent waves to propagating waves while magnifying the subwavelength image, thereby transferring it up to the far field beyond the hyperlens region. The novel characteristics are achieved through the extreme anisotropy in the effective permittivity tensor, which usually gives the hyperbolic form of a dispersion relation spanning the high angular wavevector components [16-18, 50, 54].

There also have been some attempts to extend these ideas in acoustics [108-110]. Among them, Li et al. [109] experimentally demonstrate that the acoustic magnifying hyperlens also can be realized without using the negative effective parameters for density and bulk modulus, which are usually obtained by the local resonances of constituent elements. Thus avoiding the limitations on a working frequency range and a large loss originating from the use of resonances, the acoustic hyperlens achieves the subwavelength-imaging capability while exhibiting a nearly-flat dispersion relation over a wide range of angular wavevectors. The extraordinary dispersion relation is simply obtained from the highly large contrast

in the (positive-valued) effective densities for the radial and angular directions by using the non-resonant angularly stratified structure consisting of air and brass layers.

To the best of our knowledge, there has been no study on an elastic magnifying hyperlens using a simple metal-air multilayer metamaterial [109, 110]. In this study, the elastic hyperlens consisting of the non-resonant metamaterials, which works in an ultrasonic frequency range, will be proposed and its subwavelength-imaging capability will be demonstrated by experiments.

This chapter covers the following contents. In Section 4.2, a metal-air multilayer metamaterial is introduced and its effective properties are characterized by adopting the analytic homogenization method as well as the S-parameter retrieval method demonstrated in Chapter. 3. In Section 4.3, the performance of the designed elastic hyperlens constructed by using the metal-air multilayer metamaterial is validated by implementing the FEM simulations as well as the experiments.

The overall contents are also covered in [111].

4.2 Introduction of Metal-Air Multilayer Metamaterials for Extreme Anisotropy

Earlier studies in acoustics have shown that a metal-air multilayer metamaterial can achieve an extreme anisotropy without using a resonance scheme [109, 110]. The metamaterial yields the two main characteristics on wave propagation: one is that waves propagate dominantly along the orthogonal to the stratified direction while do not along the stratified direction and the other is that the wave components exhibiting high wavenumbers in the stratified direction, which are supposed to

decay in a general isotropic medium, are supported to propagate. The characteristics yield the hyperlens-like behaviors specifically when the metamaterial is arranged in the angular direction even without the help of a resonance scheme as seen in [109].

The meta-air multilayer metamaterial has distinct strengths compared to the resonance-based metamaterials exhibiting strong anisotropies, which are (1) the very-simple configuration and (2) the working capability in a quite broad frequency range. In spite of the strengths, however, the metamaterial has not been widely utilized for the applications, and the analysis on wave propagation in the metamaterial has not been deeply conducted specifically in the elastic regime.

In this section, the characterization of the effective properties for the metamaterial will be implemented in the elastic regime by using the analytic homogenization method after validating the method by the S-parameter retrieval method.

4.2.1 Design and configuration

Figure 4.1 shows the schematic configuration of a 2D metal-air multilayer metamaterial model disposed in the x - y plane with the stratified direction on the x -axis. For a metal substance, aluminum is employed here and the material properties of aluminum and air are considered as follows:

aluminum: mass density $\rho_{\text{al}} = 2700 \text{ kg/m}^3$, Poisson's ratio $\nu_{\text{al}} = 0.33$, Young's

$$\text{modulus } E_{\text{al}} = 7.1 \times 10^{10} \text{ N/m}^2,$$

air: mass density $\rho_{\text{air}} = 1.21 \text{ kg/m}^3$, Bulk modulus $K_{\text{air}} = 1.42 \times 10^5 \text{ N/m}^2$.

The length of a unit cell (lattice constant) for the stratified direction is denoted by d

in the figure while the thicknesses of metal and air layers, by $f_v d$ and $(1 - f_v) d$ respectively where f_v indicate the volume fraction of a metal layer in the unit cell. Here, the schematic configuration of the elastic magnifying hyperlens, which is constructed by using the present metamaterial, is also shown in Figure 4.2. After rearranging the metamaterial in the angular direction with $f_v = 0.6$, the elastic hyperlens is designed in a half-circular shape following the configuration of the acoustic hyperlens [109]. The detail design is as follows: it consists of 90 air fins extending from 5.2 cm to 31.2 cm from the origin in a 2-mm-thick aluminum plate and each air fin is slit to occupy 0.8° in the angular direction while each of the remaining aluminum fins occupies 1.2° .

Even though the proposed hyperlens resembles the acoustic hyperlens by Li et al., the involved physics on wave propagation in the hyperlens should be completely different with each other. It is because the main path of wave power is different; most of the power propagates through metal layers in case of elastic waves while it propagates through air layers in case of acoustic waves. Therefore, a different characterization methodology is required in this case compared with that done in acoustics. The homogenization of stiffness should be adopted here, not the homogenization of density as done in acoustics [51-53, 109] since the propagation characteristics of elastic waves in anisotropic solid media are totally determined by the stiffness tensor [47, 48, 64, 65, 112].

4.2.2 Effective-property characterization by the analytic homogenization method

In order to the characterize the effective properties of the metal-air multilayer metamaterial, the two schemes are proposed in this study; one is defining air by a solid substance possessing the corresponding material properties to them of air and the other is characterizing the metamaterial by employing the analytic homogenization method. Using the two schemes, the characterization will be implemented here and the result will be compared to the FEM result later.

Begin with the first scheme, which is regarding air as a solid substance and defining the elastic constitutive properties for air. The stiffness of air can be derived by using the linear continuity equation in acoustics and the instinct characteristic of fluid that it does not support the shear stress [113, 114]. The linearized continuity equation is as follows:

$$\frac{\partial s}{\partial t} + \nabla \cdot \mathbf{v} = 0 \quad (4.1)$$

where s denotes the condensation and \mathbf{v} , the particle velocity of a fluid element. When the condensation s is small enough, it can be written in terms of acoustic pressure p and adiabatic bulk modulus K as

$$s \approx \frac{p}{K}. \quad (4.2)$$

Substituting Eq. (4.2) into Eq. (4.1) yields

$$\frac{1}{K} \frac{\partial p}{\partial t} + \nabla \cdot \mathbf{v} = 0 \quad (4.3)$$

under the condition that K is invariant with respect to t . Rewriting Eq. (4.3) as

$$\frac{p}{K} + \nabla \cdot \mathbf{u} = 0 \quad (4.4)$$

in terms of displacement \mathbf{u} gives

$$-p = K \nabla \cdot \mathbf{u} = K \frac{\partial u_i}{\partial x_i}. \quad (4.5)$$

For the 2D case in the x - y plane, the stiffness tensor of air can be expressed as follows from Eq. (4.5):

$$\mathbf{C}^{\text{air}} = \begin{bmatrix} K & K & 0 \\ K & K & 0 \\ 0 & 0 & 0 \end{bmatrix}. \quad (4.6)$$

Then the second scheme, which is characterizing the effective properties of the metamaterial after adopting the analytic homogenization method, will be described. Specifically for the simple alternating layered structure, the analytic homogenization approach [115] is valid and it is known to give the fairly accurate effective properties. Here are the adopted analytic equations for the homogenization of the stiffness components when the structure consists of alternating two bilayers, Layer A and Layer B, in the x -direction:

$$C_{11}^{\text{eff}} = \left[\frac{f_v}{C_{11}^A} + \frac{1-f_v}{C_{11}^B} \right]^{-1} \quad (4.7)$$

$$C_{12}^{\text{eff}} = \left[f_v \frac{C_{12}^A}{C_{11}^A} + (1-f_v) \frac{C_{12}^B}{C_{11}^B} \right] \cdot \left[\frac{f_v}{C_{11}^A} + \frac{1-f_v}{C_{11}^B} \right]^{-1} \quad (4.8)$$

$$C_{22}^{\text{eff}} = \left[f_v C_{22}^A + (1-f_v) C_{22}^B \right] - \left[f_v \frac{(C_{12}^A)^2}{C_{11}^A} + (1-f_v) \frac{(C_{12}^B)^2}{C_{11}^B} \right] + \left[f_v \frac{C_{12}^A}{C_{11}^A} + (1-f_v) \frac{C_{12}^B}{C_{11}^B} \right]^2 \cdot \left[\frac{f_v}{C_{11}^A} + \frac{1-f_v}{C_{11}^B} \right]^{-1} \quad (4.9)$$

$$C_{66}^{\text{eff}} = \left[\frac{f_v}{C_{66}^A} + \frac{1-f_v}{C_{66}^B} \right]^{-1} \quad (4.10)$$

where \mathbf{C}^A and \mathbf{C}^B represent the stiffness tensors of the substances composing

Layers A and B respectively and f_v , the volume fraction of Layer A in the unit cell. By using Eqs. (4.7-10), the homogenized stiffness tensor can be derived after substituting the stiffness tensor of air defined in Eq. (4.6) and the following stiffness tensor of metal (aluminum) into the equations:

$$\mathbf{C}^{\text{al}} = \begin{bmatrix} E_{\text{al}}/(1-\nu_{\text{al}}^2) & \nu_{\text{al}}E_{\text{al}}/(1-\nu_{\text{al}}^2) & 0 \\ \nu_{\text{al}}E_{\text{al}}/(1-\nu_{\text{al}}^2) & E_{\text{al}}/(1-\nu_{\text{al}}^2) & 0 \\ 0 & 0 & E_{\text{al}}/2(1+\nu_{\text{al}}) \end{bmatrix} \quad (4.11)$$

under the plane stress condition and

$$\mathbf{C}^{\text{al}} = \begin{bmatrix} E_{\text{al}}(1-\nu_{\text{al}})/(1+\nu_{\text{al}})(1-2\nu_{\text{al}}) & E_{\text{al}}\nu_{\text{al}}/(1+\nu_{\text{al}})(1-2\nu_{\text{al}}) & 0 \\ E_{\text{al}}\nu_{\text{al}}/(1+\nu_{\text{al}})(1-2\nu_{\text{al}}) & E_{\text{al}}(1-\nu_{\text{al}})/(1+\nu_{\text{al}})(1-2\nu_{\text{al}}) & 0 \\ 0 & 0 & E_{\text{al}}/2(1+\nu_{\text{al}}) \end{bmatrix} \quad (4.12)$$

under the plane strain condition [84] where E_{al} and ν_{al} denote the Young's modulus and the Poisson's ratio respectively for aluminum. Specifically under the plane strain condition for the stiffness of aluminum, the homogenized stiffness tensor is calculated to be

$$\mathbf{C}^{\text{eff}} \approx \begin{bmatrix} 3.55 \times 10^5 & 2.47 \times 10^5 & 0 \\ 2.47 \times 10^5 & 4.78 \times 10^{10} & 0 \\ 0 & 0 & 0 \end{bmatrix} \text{ N/m}^2 \quad (4.13)$$

while the effective mass density, ρ^{eff} is 1621 kg/m^3 , which is estimated from the arithmetic mean of the densities for aluminum and air expressed as

$$\rho^{\text{eff}} = f_v \rho_{\text{al}} + (1-f_v) \rho_{\text{air}}. \quad (4.14)$$

Note that the arithmetical mean is adopted here for determining the effective mass density because it well-known to give the fairly reasonable value specifically for

the elastic metamaterials consisting of non-resonant elements in a low frequency region [53, 116-118].

It may worth to remarking on the retrieved effective stiffness described in Eq. (4.13). The normal component for the y -direction (orthogonal to the stratified direction) C_{22}^{eff} is significantly large compared to it for the x -direction (stratified direction) C_{11}^{eff} , which means that waves should propagate dominantly in the y -direction in the medium when considering the corresponding phase velocities or wavenumbers. The each value well coincide with the results from the Reuss and Voigt models [119], respectively. Note that the effective shear component C_{66}^{eff} exhibits the nearly-zero value because of the presence of air. So in the present medium, shear waves should not be supported to propagate and only (quasi)longitudinal waves will develop. The result shows that the metamaterial is retrieved to be extremely anisotropic without negative-valued parameters.

To see the extremely-anisotropic wave propagation characteristic in the metamaterial, the EFC is calculated at 100 kHz after substituting the retrieved effective properties described in Eq. (4.13) into the Christoffel equation in Eqs. (3.31-32). The result is plotted in Figure 4.3 by black thick line where the EFC for (isotropic) aluminum is also shown with black thin line. Owing the extreme difference in modulus between aluminum and air, yielding the ratio of 7.4×10^5 , the metamaterial achieves the nearly flat profile that covers significantly high wavevectors in the x -direction (stratified direction). Consequently, not only propagating waves but also evanescent waves carrying high wavevector components are supported to propagate specifically along the y -direction when considering the group velocity direction known to be normal to the EFC profile [54,

75, 96].

In the figure, the directions of the polarization vectors [47] at specific wavevectors are also shown with red arrows, which are calculated through using the effective properties. They are observed to be aligned nearly with the y -direction regardless of \mathbf{k} , which implies that wave modes are purely longitudinal even for the large values of k_x .

In order to compare the present result obtained by using the homogenized effective properties with those by other approaches, the EFCs are also calculated by the transfer matrix method [79, 81, 82], the reciprocal approach [53, 109], and the FEM solving the eigenvalue problem on the detailed model [66-68]. Here, only the result from the FEM is shown and marked by magenta dots in the figure. It fairly corresponds to that from the effective properties, confirming that the properties are accurately estimated and the proposed homogenization scheme successfully works. Although the other two results are not shown here, they also yield the EFCs very close to that from the homogenization method.

4.2.3 Validation of the analytic homogenization method by the S-parameter retrieval method

In the previous section, the proposed homogenization scheme employing the analytic homogenization method is shown to yield the accurate effective properties for the metal-air multilayer metamaterial. Here, the validation of the analytic homogenization method will be implemented to confirm that the method is valid for general metamaterials consisting of alternating two bilayers. The validation is required because the analytic equations do not take dynamic characteristics into

account. For the validation, the S-parameter retrieval method demonstrated in Chapter. 3 is employed.

Two metamaterial models are considered here whose configurations are exactly same with that shown in Figure 4.1 but both consisting of solid bilayers:

- (1) Model 1: aluminum-Lucite multilayer metamaterial where the material parameters for Lucite are $\rho_{lu} = 1200 \text{ kg/m}^3$, $E_{lu} = 0.4 \times 10^{10} \text{ N/m}^2$, and $\nu_{lu} = 0.4$,
- (2) Model 2: aluminum-rubber multilayer metamaterial where the material parameters for rubber are $\rho_{rb} = 1100 \text{ kg/m}^3$, $E_{rb} = 0.23 \times 10^{10} \text{ N/m}^2$, and $\nu_{rb} = 0.4$ [113].

By using the S-parameter retrieval method, the effective properties of Models 1 and 2 are determined and the results are presented with dots in Figures 4.4(a, b) respectively. For the comparison, the properties from the analytic homogenization method are also shown with grey solid lines. The properties from the two methods quite coincide with each other even though they exhibit some discrepancies as frequency increases. The results signify that the analytic method is valid for the present metamaterials and yields the accurate properties specifically in the long-wavelength limit.

Note that the contrast ratio between the values of C_{11} and C_{22} is observed to be large in the case of Model 2 compared to it in the case of Model 1. It should originate from the large contrast value in the stiffness parameters between aluminum and rubber (Model 2) compared to it between aluminum and Lucite (Model 1). As the constituent bilayer exhibits a large stiffness contrast, the metamaterial becomes to get strong anisotropy. It demonstrates how come the

metal-air metamaterial achieves the extreme anisotropy.

In Figure 4.5, the EFCs for the two models are shown where the EFC obtained by using the analytic homogenization method is indicated by magenta dots while it by using the S-parameter retrieval method, by black solid lines. At 10 kHz, the two results are nearly identical with each other as already seen in the retrieved properties in Figure 4.4.

From the EFC profiles, strong anisotropy is observed with respect to the x - and y -axes specifically in the case of Model 2. The profile for a quasilongitudinal wave is fairly flattened along the x -direction and it covers even large- k_x wave components while the profile for a quasitransverse wave is significantly expanded. The results demonstrate how come the extremely-flat EFC profile is obtained for a longitudinal wave in the metal-air model while the negligible profile, for a transverse wave.

4.3 Design of Elastic Magnifying Hyperlens

The metal-air multilayer metamaterial is shown to exhibit extreme anisotropy with respect to the stratified and the orthogonal directions. Owing to the anisotropy, it gets the nearly flattened EFC profile in the stratified direction, which leads longitudinal waves to propagate dominantly along the orthogonal direction, while spanning the significantly-large-valued wavenumbers, which leads the evanescent waves in a general isotropic medium to propagate also along the orthogonal direction.

By rearranging the metal-air metamaterial with the stratified direction in the angular direction, the elastic hyperlens is constructed as already shown in Figure 4.2. The effective properties of the hyperlens are assumed to be equal to them of

the metamaterial depicted in Figure 4.1, which can be obtained from the analytic homogenization equations described in Eqs. (4.7-10).

In this section, the performance of the elastic hyperlens will be shown. It is analyzed by using the FEM simulations on the detailed and the effective medium models of the hyperlens, and the simulation results are validated by experiments.

4.3.1 Validation of the performance by FEM simulations

Figure 4.6 shows the time-harmonic simulation results conducted in COMSOL Multiphysics 3.5a under the plane stress condition. In order to investigate the subwavelength-imaging capability of the proposed hyperlens, a sub-diffraction-limited object is set to be located just in front of the inner edge of the hyperlens. As the object, two sources having the width of 1.3 cm are used with the center-to-center separation distance of 2.47 cm. It corresponds to 0.45λ (λ : wavelength) at 100 kHz. The separation distance is limited due to the crosstalk in deformations between the sources that results from Poisson's ratio. To minimize the crosstalk, each source is set to be approximately line-shaped for generating waves dominantly along the radial direction [113, 120].

Note that the actual waves propagating in the plate hyperlens (thickness: 2 mm) are the lowest symmetric guided waves, but their behavior at frequencies around 100 kHz can be accurately predicted by using non-dispersive longitudinal bulk waves under the plane stress condition [48, 84], which can be easily simulated with FEM tools.

The radial stress fields without and with the hyperlens are shown at the bottom-left and -right respectively in the figure also with the zoomed fields outside the

hyperlens region. The stress distributions along the azimuthal arc A-B-C-D-E, located just outside the hyperlens, are shown at the top where the distributions without and with the hyperlens are indicated by blue and red lines respectively.

In the case without the hyperlens, the high-angular wavevector components carrying subwavelength information are supposed to exponentially decay in the near field of the sources. So, the two sources within a sub-diffraction limited distance cannot be resolved with the homogeneous isotropic medium alone. In the case with the hyperlens, however, the two sources can be resolved because the hyperlens recovers the evanescent waves to propagate with their fine features remaining. The surprising behavior of the hyperlens also can be confirmed by the propagation velocities of the longitudinal waves in the medium, which can be calculated by using the effective properties: 5432 m/s and 15 m/s for the radial and angular directions, respectively. The significantly high contrast in velocity leads the subwavelength image to be wholly transferred up to the outer edge of the hyperlens. Note that the waves transmitted to the outer edge still propagate while maintaining the form intact even far beyond the hyperlens. It is because the linear tangential momentum of the waves becomes compressed in the hyperlens while the angular momentum is conserved [16-18, 109], which can be demonstrated by the fact that the initial separation distance between the sources, 0.45λ , is magnified to 2.78λ at the outer edge. Thereby, the image of two distinct beams can be still obtained in the far-field.

The performance of the hyperlens is also analyzed by using the effective medium model, and it is compared to the result for the detailed model in Figure 4.7. At the top of the figure, the zoomed view of the stress distribution in a region just outside

the hyperlens (A-C-D-B and A'-C'-D-B) is also shown. The result from the effective medium model is almost identical to that from the full metal-air model. This agreement signifies that the proposed hyperlens is unlike a waveguide, because the manipulation of wave propagation is achieved in the absence of discontinuous boundaries but only with the homogenized properties [121]. The results confirm that the hyperlens is accurately characterized by using the proposed homogenization scheme.

4.3.2 Validation of the performance by experiments

In this section, the performances of the proposed hyperlens not only resolving a subwavelength image but also transferring it dominantly along the radial direction will be validated by experiments.

The configuration of the fabricated elastic hyperlens and the experiment setups are shown in Figure 4.8. In the experiment, ultrasonic magnetostrictive transducers [120, 122] are used for the generation and measurement of the lowest symmetric Lamb wave mode. Because it is difficult to install ultrasonic transducers directly at the source locations while maintaining the subwavelength separation distance, a special configuration is designed by using slender waveguides. Pulse signals generated by the transducers located at the far ends of the waveguides propagate through the waveguides to reach the other ends, and then they serve as the actual sources. In order to minimize the crosstalk, the source regions are set to be approximately line-shaped for generating waves dominantly along the radial direction as previously mentioned.

Figure 4.9 shows the experimental results over the range from 1.8 cm to 14.3 cm

away from the outer edge of the hyperlens in the radial direction. A modulated Gaussian [120, 122] input pulse signal with the center frequency of 100 kHz was used for the experiment. The radial stress field at a specific time is shown in Figure 4.9(a) while the squared radial stress fields, in Figure 4.9(b) with the passage of time. In all the results, two distinct peaks are clearly identified as seen in the simulation results. It demonstrates that the hyperlens successfully resolves the sub-diffraction-limited object and transfers it to the far field beyond the hyperlens while magnifying its form. Observed non-vanishing stress levels along the line B-D should be due to the crosstalk between two sources.

The normalized squared stress distributions along the arc C-C' with (marked by blue lines) and without (red lines) the hyperlens are compared with the results from the simulations in Figure 4.10. The results from the experiments and simulations are fairly identical with each other, and it signifies that experiments are successfully implemented to investigate the hyperlens performance.

From the experimental results, the following remarks can be made.

- (1) The input pulse generated by the transducer has a center frequency with a relatively narrow but finite bandwidth. The fact that the two distinct peaks are observed in the experimental results demonstrates that the proposed hyperlens clearly shows a capability to operate over a relatively broad frequency band owing to not involving a local resonance.
- (2) The magnified sub-diffraction-limited image is obtained at the outer edge of the hyperlens exactly at the expected locations. It demonstrates that all of the wave components propagate nearly along the radial direction as predicted from the FEC profile.

- (3) The resolved two distinct peaks are consistently observed with the passage of time as shown in Figure 4.9(b). It indicates that high angular wavevector components carrying the subwavelength information on an imaging object are transmitted through the hyperlens and thus propagate in the far field.

4.3.3 Estimation of output/input power ratio

Here, the ratio between the input and output powers (output/input) for the proposed hyperlens will be investigated and the ratio obtained from experiments will be compared with it from simulations.

Because the magnitudes of the incident elastic waves entering the hyperlens cannot be directly measured using a sensor usually having a certain size in the experiment, the experimental ratio between the input and output wave magnitudes is estimated by an indirect way as follows:

$$\frac{\varepsilon_{rr}^B|_{\text{exp}}}{\varepsilon_{rr}^A|_{\text{exp}}} = \frac{\varepsilon_{rr}^B|_{\text{exp}}}{\varepsilon_{rr}^D|_{\text{exp}}} \cdot \frac{\varepsilon_{rr}^D|_{\text{exp}}}{\varepsilon_{rr}^A|_{\text{exp}}} = \frac{\varepsilon_{rr}^B|_{\text{exp}}}{\varepsilon_{rr}^D|_{\text{exp}}} \cdot \frac{\varepsilon_{rr}^D|_{\text{exp}}}{\varepsilon_{rr}^C|_{\text{exp}}} \approx \frac{\varepsilon_{rr}^B|_{\text{exp}}}{\varepsilon_{rr}^D|_{\text{exp}}} \cdot \frac{\varepsilon_{rr}^D|_{\text{sim}}}{\varepsilon_{rr}^C|_{\text{sim}}} \quad (4.15)$$

where $\varepsilon_{rr}|_{\text{exp}}$ indicates the strain magnitude for the radial direction which is measured in the experiment while $\varepsilon_{rr}|_{\text{sim}}$, the strain magnitude obtained in the numerical simulation. The upper indices, A and B indicate the locations just near the inner and outer edges of the hyperlens respectively as denoted in Figure 4.11(a) while the upper indices, C and D, the same locations with A and B respectively but for the case without the hyperlens as denoted in Figure 4.11(b); so $\varepsilon_{rr}^A|_{\text{exp}}$ indicates the strain magnitude experimentally measured at the point A, the input wave magnitude, while $\varepsilon_{rr}^B|_{\text{exp}}$, the output wave magnitude.

In order to verify the validity of the following assumption in Eq. (4.15) as

$$\frac{\varepsilon_{rr}^D|_{\text{exp}}}{\varepsilon_{rr}^C|_{\text{exp}}} \approx \frac{\varepsilon_{rr}^D|_{\text{sim}}}{\varepsilon_{rr}^C|_{\text{sim}}}, \quad (4.16)$$

an extra experiment is conducted to compare the distribution of the strain field along the line C-D obtained by the experiment to one by the numerical simulation.

The result is shown in Figure 4.12. Both the strain fields obtained by the FEM simulation (marked by black line) and the experiment (by magenta dots) are normalized with respect to each value obtained at 2 cm away from the location of C. Good correlation is observed between them and the assumption described in Eq. (4.16) is regarded somewhat reasonable. Note that the region just around the location C, the grey-colored region in the figure, is not accessible with a sensor due to the specific size.

By using Eq. (4.15), the ratio between the input and output wave magnitudes can be experimentally estimated after measuring the strain fields at B ($\varepsilon_{rr}^B|_{\text{exp}}$) and D ($\varepsilon_{rr}^D|_{\text{exp}}$). The ratio is observed to be around 0.295 while the ratio in the simulation is obtained as 0.251. A small amount of discrepancy is found, which may originate from the difference between the actual source used in the experiment and its simulated model, among others.

4.4 Summary

In this study, the effective-property characterization is implemented for a metal-air multilayer metamaterial by using the analytic homogenization method. The retrieved properties are shown to exhibit extreme anisotropy with respect to the

stratified and the orthogonal directions; the normal stiffness component for the stratified direction is observed to be in the order of 10^5 N/m^2 while it for the orthogonal direction, 10^{10} N/m^2 . Owing to the extreme anisotropy, the proposed hyperlens achieves the nearly flattened EFC profile along the stratified direction spanning a significantly large range of wavenumbers, which leads evanescent waves carrying the large-valued wavenumbers to propagate nearly along the orthogonal to the stratified direction.

After angularly rearranging the metamaterial, the elastic magnifying hyperlens is constructed. The performance of the hyperlens is experimentally validated for a subwavelength imaging at 100 kHz, an ultrasonic frequency. The experiment results show that a sub-diffraction-limited object can be imaged without any help of a resonance scheme. The experiment may be useful to expedite the realization of subwavelength imaging in medical ultrasound or non-destructive evaluation using ultrasonic elastic waves.

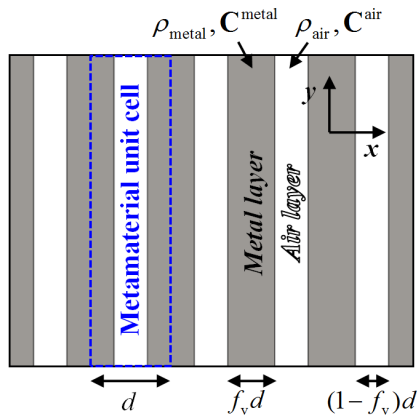


Figure 4.1 The schematic configuration of a metal-air multilayer metamaterial

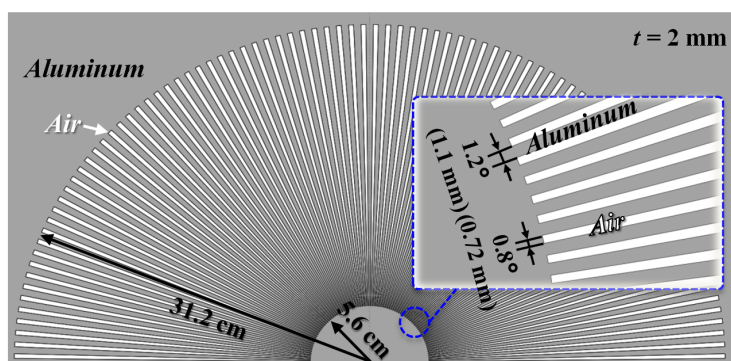


Figure 4.2 The proposed elastic magnifying hyperlens consisting of the angularly-arranged metal-air multilayer metamaterials

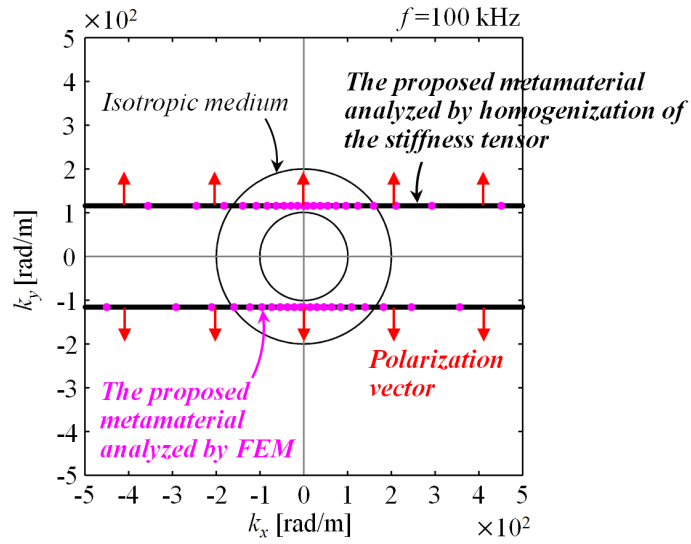
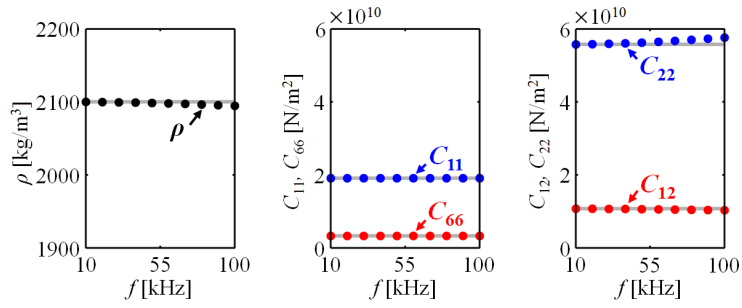


Figure 4.3 The EFCs for the metal-air multilayer metamaterial at 100 kHz analyzed by the effective medium (black thick solid lines) and the detailed model using the FEM (magenta dots) and the polarization vectors at specific \mathbf{k} (red arrows)

(a) Effective properties of Model 1



(b) Effective properties of Model 2

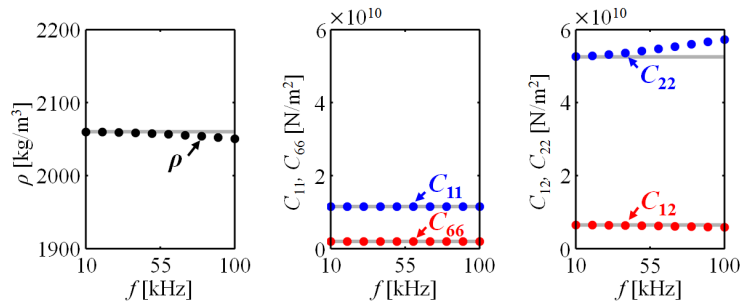
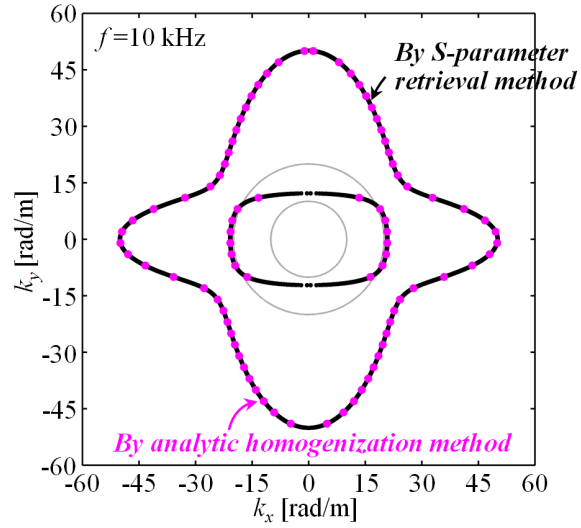


Figure 4.4 The effective properties of (a) Model 1 and (b) Model 2, calculated by using the analytic homogenization method (grey solid lines) and the S-parameter retrieval method (dots)

(a) EFC for Model 1



(b) EFC for Model 2

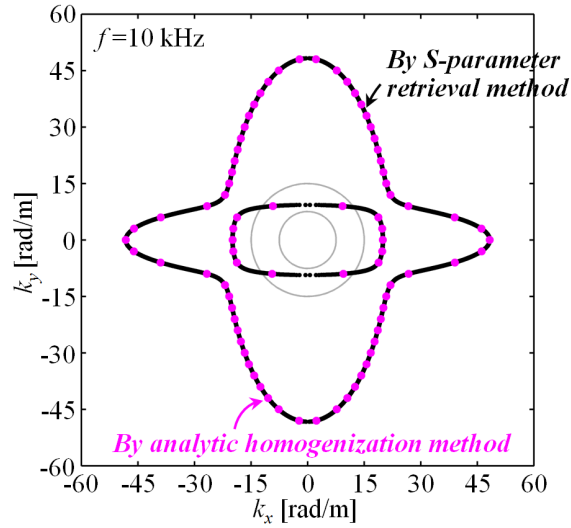


Figure 4.5 The EFCs for (a) Model 1 and (b) Model 2, obtained by using the analytic homogenization method (magenta dots) and the S-parameter retrieval method (black solid lines)

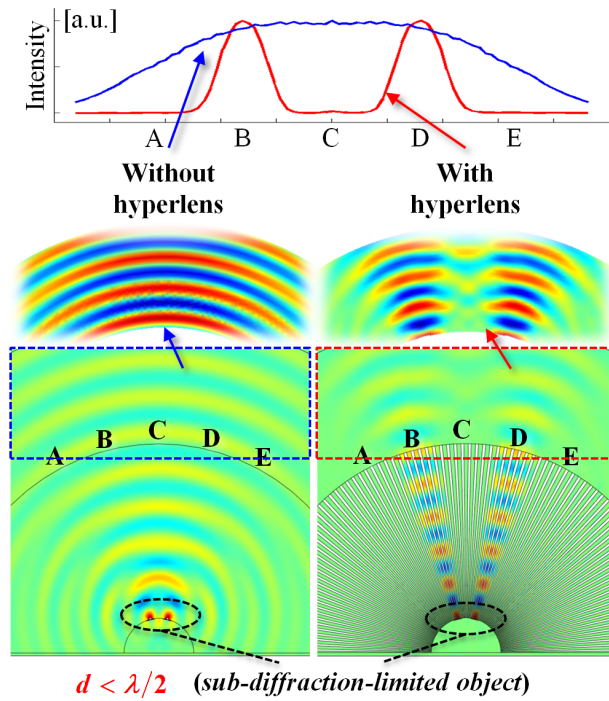


Figure 4.6 The FEM simulation results for the radial stress distributions without (bottom-left) and with (bottom-right) the hyperlens, and the intensity distributions (top)

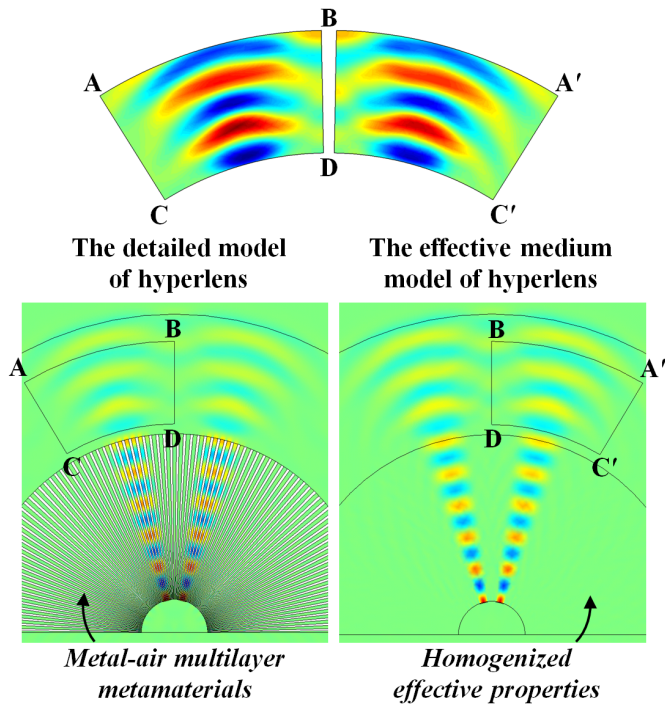


Figure 4.7 The FEM simulation results for the radial stress distributions analyzed by the detailed (bottom-left) and the effective medium (bottom-right) models with the zoomed views (top) in the regions of A-C-D-B and A'-C'-D-B

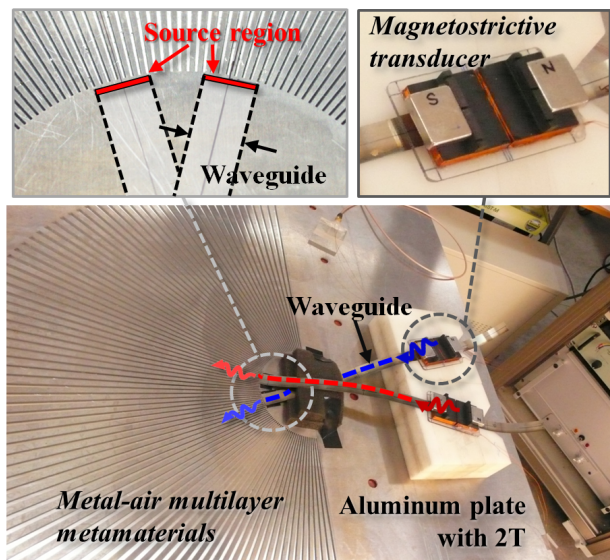
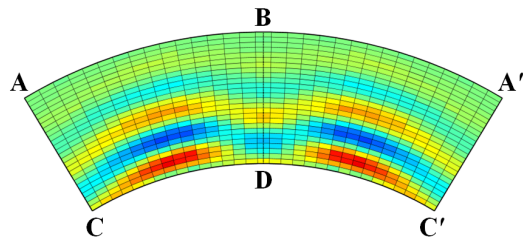


Figure 4.8 The photos of the fabricated elastic hyperlens and the experimental setups

(a) Radial stress distribution



(b) Squared radial stress distribution

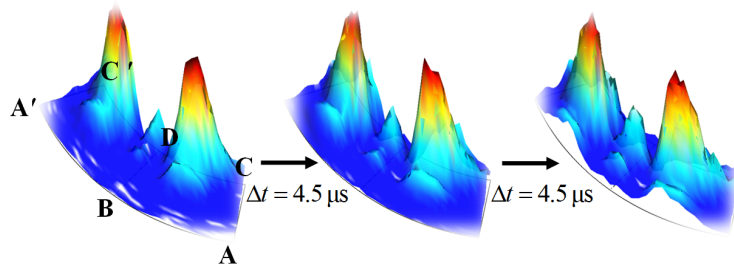


Figure 4.9 The experimental results for (a) the radial stress distribution and (b) the squared radial stress distributions with the passage of time

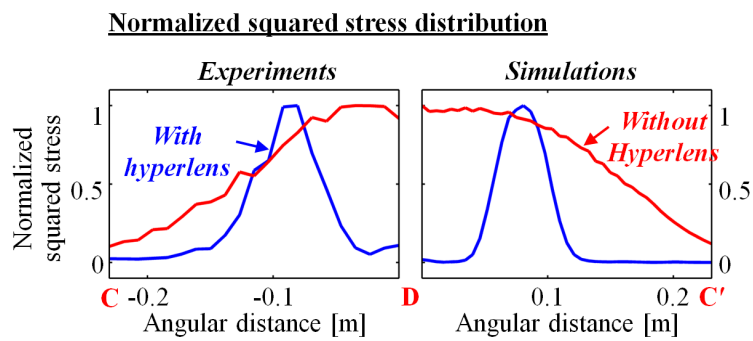


Figure 4.10 The comparisons between the experimental and the simulation results for the normalized squared stress distributions with and without the hyperlens

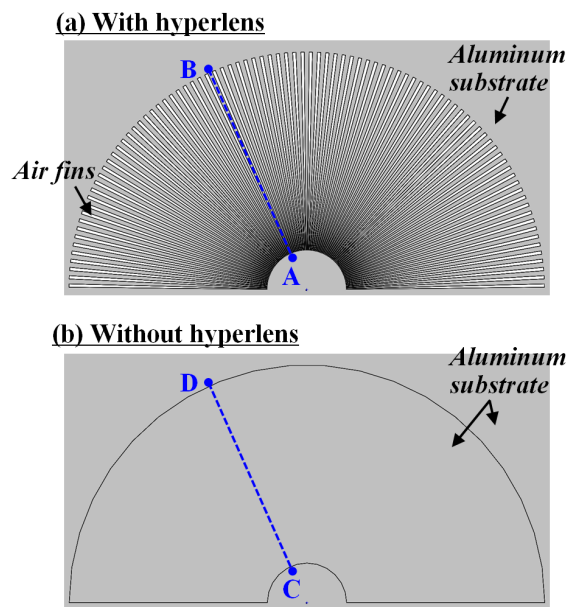


Figure 4.11 The schematic pictures for the definitions of the locations A-D

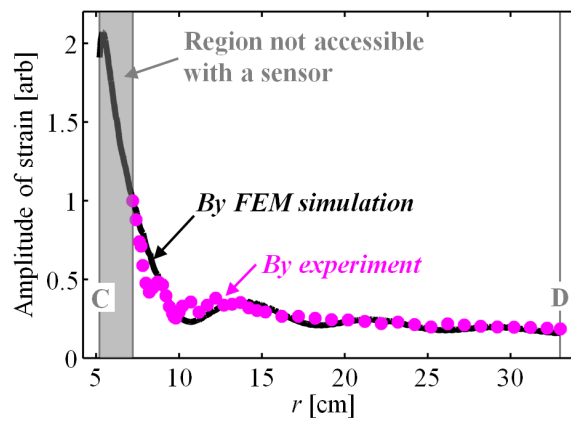


Figure 4.12 The comparisons between the experimental (magenta dots) and the simulation (black solid line) results

CHAPTER 5.

Design of Quasi-Ideal Mechanical Bandpass Filters

by Using Impedance-Only-Varying Elastic Metamaterials

5.1 Quasi-Ideal Bandpass Filters

Over the past few decades, photonic/phononic crystal (PC) structures have received a great attention because of their extraordinary characteristics in wave propagation and energy transmission [56, 58, 123-128]. Among these, the Bragg bandgap phenomenon [69, 123, 124, 126, 129] is well-known, which originates from the destructive interference of the scattered waves generated at the periodic lattices when wavelengths are in the order of periodicity scale. An extensive work has been done on the analysis of the Bragg bandgap phenomenon and its applications such as filters [59, 126-128, 130]. Here, the PC structures utilizing the bandgap phenomenon will be referred to as photonic/phononic bandgap (PBG) structures as in earlier works.

While PBG structures can be fundamentally used as bandstop reflection filters as well as bandpass filters because of their intrinsic formations of passband and stopband regions, finite-sized PBG structures cannot exhibit ideal bandpass filter performances due to the resonance-induced fluctuations in their transmission spectra [123, 126, 129, 130]. In order to obtain a transmission passband avoiding the fluctuations, methods utilizing a resonance scheme such as the Fabry-Perot resonance (FPR) in a one-dimensional (1D) PBG structure have been suggested; one can construct a 1D PBG structure by inserting an element of a single quarter-

wave phase-shift in the center of the structure [55, 59, 127] or form a 1D PBG structure consisting of alternating negative-index metamaterial and dielectric slabs [131, 132]. The PBG structure having a single quarter-wave phase-shift can develop a very narrow transmission peak in the middle of a bandgap region owing to the quarter-wave phase-shift, which yields the FPR. The PBG structures employing negative-index metamaterial slabs can also develop multiple sharp transmission peaks at the FPRs within wide bandgap regions. Although such PBG structures achieve non-fluctuating transmission passbands surrounded by stopbands, they cannot be used when wider passbands having the flat tops and steep bandedges are demanded.

To overcome the limitations of the above-mentioned methods, a 1D PBG structure having multiple symmetrically-distributed quarter-wave phase-shift slabs were proposed [55, 56, 58, 133]. If the locations of the multiple phase-shift slabs inside the PBG structure are optimized, the structure can yield a wide passband with the quasi-flat top. But the structure size should be significantly large to get a flattened wide passband and the steep bandedges simultaneously, and the bandwidths of the surrounding stopbands become rather narrow relative to the bandwidth of a passband.

Motivated by the above-mentioned observations, a 1D PBG structure is aimed to be engineered for realizing quasi-ideal bandpass filtering performances: flattened passband, steep bandedges, surrounding wide and deep stopbands. To achieve the goal, the half-quarter-wave stack (HQWS) structure [69] is adopted here with the following propositions: (1) while keeping the material parameters of constituent layers unchanged, only the characteristic (acoustic) impedances of half-wave layers

are varied, and (2) the impedance-varying half-wave layers are realized by using positive-index elastic metamaterials.

The HQWS structure is chosen here because it intrinsically exhibits a bandpass-filter-like transmission spectrum; the existence of half-wave layers contributes to a FPR formation while the coexistence of half- and quarter-wave layers contributes to the formation of two Bragg bandgaps symmetrically around the FPR locations [69]. Because the passbands formed around the FPRs are known to suffer from fluctuations when the structure gets the finite size, the structure itself cannot be an ideal bandpass filter. As a means to suppress the undesirable fluctuations in the passbands and achieve a flattened transmission passband, the novel scheme that is varying the characteristic impedances of half-wave layers while keeping the phase-shifts in the layers unchanged is proposed. Note that the scheme is totally different with the conventional geometric (thickness) variation scheme [134-139]. And, in order to realize the impedance-only-variation scheme, another scheme that is using positive-index elastic metamaterials is proposed.

The organization of this chapter is as follows. The effects of the proposed impedance variation are studied for finite PBG structures in Section 5.2.1, and specific impedance distributions will be investigated for achieving a quasi-flat-top passband and the steep bandedges in Section 5.2.2. After proposing the impedance-only-varying elastic metamaterials in Section 5.3, the realization of the impedance-varying HQWS structure will be shown in Section 5.4. The findings from this study are summarized in Section 5.5.

5.2 Proposition of Impedance-Varying Phononic Bandgap Structures

for Bandpass Filters

In this section, the effects of the characteristic-impedance variation imposed on a PBG structure will be investigated by theoretically analyzing the transmission characteristics, and a quasi-ideal bandpass filter will be achieved by utilizing the impedance variation. The proposed impedance variation scheme has not been utilized and even studied until now to the best of our knowledge.

The impedance variation scheme shows distinctively different effects on the transmission characteristics of PBG structures compared to them by the conventional thickness variation scheme. While the conventional one induces the localization effects in the neighborhoods of the Bragg bandgaps and disturbs the phase coherence among the constituent unit cells in PBG structures in an overall frequency range [134-138], the proposed one induces the localization effects just in the neighborhoods of the Bragg bandgaps while preserving the phase coherence at the Bragg bandgap and FPR frequency regions. When considering the utilization of a PBG structure is mainly for obtaining the Bragg bandgaps or the FPRs, the capability of preserving the intrinsic features gives a great strength for the impedance variation scheme.

5.2.1 Theoretical analysis on the impedance variation

To begin with, it is emphasized that the proposed approach varying characteristic impedances while keeping phase shifts unchanged in the constituent layers of a PBG structure is conceptually different from the conventional technique perturbing layer thicknesses. In order to demonstrate it clearly, the transfer matrix \mathbf{T} dealing with the longitudinal wave propagation in a 1D PBG structure is considered here.

The transfer matrix \mathbf{T} relates the x -directional velocity (v) and the normal stress (σ) at the right side of the $(m-1)$ -th cell and those at the right side of the m -th cell as

$$\begin{Bmatrix} v \\ \sigma \end{Bmatrix}_m = \mathbf{T} \begin{Bmatrix} v \\ \sigma \end{Bmatrix}_{m-1}. \quad (5.1)$$

If each unit cell is assumed to consist of two layers made of Materials 1 and 2, \mathbf{T} can be written as a product of two similar matrices:

$$\mathbf{T} = \begin{bmatrix} \cos \varphi_2 & -(j/z_2) \sin \varphi_2 \\ -jz_2 \sin \varphi_2 & \cos \varphi_2 \end{bmatrix} \begin{bmatrix} \cos \varphi_1 & -(j/z_1) \sin \varphi_1 \\ -jz_1 \sin \varphi_1 & \cos \varphi_1 \end{bmatrix} \quad (j = \sqrt{-1}) \quad (5.2)$$

where z_i represents the characteristic (acoustic) impedance of Material i specifically for a longitudinal wave mode and φ_i , the phase shift in the layer made of Material i , which can be defined as $\varphi_i = k_i d_i$ with $i=1, 2$ (k : longitudinal wavenumber, d : layer thickness). As seen in Eq. (5.2), the transfer matrix \mathbf{T} can be characterized by the two parameters, φ and z only. While the conventional approach is to vary d , i.e., φ without changing z , the proposed approach is to vary z without changing φ .

Now, the effects of impedance variation on transmission characteristics will be demonstrated after employing the simplest PBG structure, a quarter-wave stack (QWS) structure [126, 129] commonly used as a Bragg reflector [55, 95]. As illustrated in Figure 5.1(a), a 2-period QWS structure is inserted in an infinite medium with the characteristic impedance z_b . The impedances of low-impedance layers are denoted by $z_a^{(m)}$ (period number $m=1, 2$) while those of high-impedance

layers, by z_b with $z_a^{(m)} < z_b$. And, the phase shifts in the low- and high-impedance layers are represented by $\varphi_a^{(m)}$ and φ_b respectively where $\varphi_a^{(m)} = k_a^{(m)} d_a^{(m)} = \varphi_b = k_b d_b = \pi/2$ specifically at $\hat{f} = 1$ (\hat{f} is the frequency normalized by the center frequency of the first Bragg bandgap). For subsequent discussion, the low- and high-impedance layers shall be simply referred to as Layer A and Layer B, respectively.

Figures 5.1(b, c) show the effects of the impedance variation imposed in Layers A on the Bloch phase curve β [126, 127, 129] and transmittance T , respectively. Four cases are considered; $c = 1, 1.5, 3,$ and 5 for Cases 1-4 respectively where c denotes the impedance contrast ratio between two Layers A as $c = z_a^{(1)} / z_a^{(2)}$. In all the cases, the average of the impedances of Layers A, $(z_a^{(1)} + z_a^{(2)}) / 2$ remains unchanged to be $0.13z_b$. Note that present Bloch phase curves in Figure 5.1(b) (only the real values are shown here) are derived after regarding the whole (2-period) QWS structure as a unit superlattice [140]. The curves may not explain the detail characteristics of the present finite impedance-varying structure, but they should give easy interpretations for the variation effects.

Before interpreting the results in detail, briefly reviews on the fundamental phenomena observed in Case 1 (unperturbed-QWS case with $z_a^{(1)} = z_a^{(2)} = 0.13z_b$; marked by black lines) will be presented. In the case, the Bloch phase curve is folded specifically at $\hat{f} = 0.3, 1.7, 2.3,$ and 3.7 because the curve is calculated under the superlattice assumption as previously mentioned [140, 141]. At $\hat{f} = 2$, the Bragg and Fabry-Perot resonating conditions are simultaneously satisfied (but

the Fabry-Perot resonating condition dominates [132]). The Bragg bandgaps centered at $\hat{f}=1$ and 3 in the transmittance curve are nearly fully developed owing to the large impedance contrast between Layers A and B. Several peaks located at $\hat{f}=0.3, 1.7, 2.3,$ and 3.7 are the resonance peaks satisfying the $\sin \beta / \sin(\beta/2) = 0$ condition [123, 126, 129] where $\beta = k_{\text{eq}} d_{\text{eq}}$ (k_{eq} : effective wave number in the QWS structure, $d_{\text{eq}} = d_a^{(1)} + d_a^{(2)} + 2d_b$) while the peak at $\hat{f}=2$, one satisfying the $\varphi_a^{(1)} = \varphi_a^{(2)} = \varphi_b = \pi$ condition. We shall refer to the resonance related with the former as the “finite resonance” in this study in order to differentiate it with the FPR related with the latter.

Now, examine the results for the impedance varying cases as

Case 2: $c = 1.5$ ($z_a^{(1)} = 0.16z_b, z_a^{(2)} = 0.11z_b$; marked by red line),

Case 3: $c = 3$ ($z_a^{(1)} = 0.20z_b, z_a^{(2)} = 0.07z_b$; blue line),

Case 4: $c = 5$ ($z_a^{(1)} = 0.22z_b, z_a^{(2)} = 0.22z_b$; green line).

In the results, following observations can be remarked:

Observation 1: regardless of the value of c , the Bragg bandgaps located at $\hat{f}=1$ and 3 with their centers are perfectly preserved,

Observation 2: regardless of the value of c , the FPR located at $\hat{f}=2$ is also perfectly preserved and the value of transmittance remains to be unity,

Observation 3: as the value of c increases, the variation effects become significant at other frequency zones; the Bloch phases get perturbed from them in Case 1 and the magnitudes of transmittance considerably

decrease.

To theoretically support Observations 1 and 2, the transfer matrix $\mathbf{T}^{(m)}$ for the m -th unit cell consisting of Layers A and B is considered, which can be derived from Eq. (5.2) as

$$\mathbf{T}^{(m)} = \begin{bmatrix} \cos \varphi_b & -(j/z_b) \sin \varphi_b \\ -jz_b \sin \varphi_b & \cos \varphi_b \end{bmatrix} \begin{bmatrix} \cos \varphi_a^{(m)} & -(j/z_a^{(m)}) \sin \varphi_a^{(m)} \\ -jz_a^{(m)} \sin \varphi_a^{(m)} & \cos \varphi_a^{(m)} \end{bmatrix}. \quad (5.3)$$

Substituting $\varphi_a^{(1)} = \varphi_a^{(2)} = \varphi_b = \pi/2$ into Eq. (5.3) for investigating $\mathbf{T}^{(m)}$ at $\hat{f} = 1$ (the center frequency of the first Bragg bandgap) yields

$$\mathbf{T}^{(m)} \Big|_{\hat{f}=1} = \begin{bmatrix} -z_a^{(m)}/z_b & 0 \\ 0 & -z_b/z_a^{(m)} \end{bmatrix}, \quad (5.4)$$

which implies that the phase shift in a unit cell at $\hat{f} = 1$ remains to be π regardless of the value of $z_a^{(m)}$, leading the Bragg bandgaps to be preserved regardless of the impedance variation. And for $\varphi_a^{(1)} = \varphi_a^{(2)} = \varphi_b = \pi$ at $\hat{f} = 2$ (the FPR frequency), $\mathbf{T}^{(m)}$ becomes

$$\mathbf{T}^{(m)} \Big|_{\hat{f}=2} = \begin{bmatrix} -1 & 0 \\ 0 & -1 \end{bmatrix} \begin{bmatrix} -1 & 0 \\ 0 & -1 \end{bmatrix} = \begin{bmatrix} 1 & 0 \\ 0 & 1 \end{bmatrix}, \quad (5.5)$$

which implies that the phase shift in a unit cell at $\hat{f} = 2$ remains 2π and the full transmission performance is preserved regardless of the impedance values of constituent bilayers. The proposed impedance-only-variation scheme is found to not disturb the phase coherence among the constituent unit cells in a QWS structure at all specifically at the Bragg bandgap and FPR frequency zones.

From Observations 1 through 3, one can see the novelty of the impedance variation scheme: (1) while preserving the intrinsic transmission characteristics of a PBG

structure (Bragg bandgap formation and full transmission at the FPR), inducing variation effects (the localization in the present case) just at the frequency zones nearby the Bragg bandgaps are possible (2) regardless of the variation amount (specifically the value of c here) and the period number of a PBG structure. Note that the conventional geometric variation cannot preserve the intrinsic transmission characteristics especially when a large amount of the variation is introduced into a PBG structure having the relatively small period number because it induces variation effects over an entire frequency range while disturbing the phase coherence among the unit cells [136, 137, 139].

Now, investigate the effects of the impedance variation when imposed in a half-quarter-wave stack (HQWS) structure. In the case, a gradual arrangement of the variation will be used over the constituent layers. As depicted in Figure 5.2(a), a 5-period HQWS is considered. As done in the previous QWS case, the phase shifts in the low-impedance half-wave layers (denoted by Layers A) and the high-impedance quarter-wave layers (Layers B) will remain unaltered regardless of the variation as $\varphi_a^{(m)} = k_a^{(m)} d_a^{(m)} = \pi$ ($m=1, 2, \dots, 5$) and $\varphi_b = k_b d_b = \pi/2$ specifically at $\hat{f} = 1$ where \hat{f} is the frequency normalized to the first FPR frequency. The impedances of (half-wave) Layers A are varied as $z_a^{(m)} = z_a^{(1)} / (1 + \Delta(m-1))$ while the those of (quarter-wave) Layers B unvaried where Δ represents the degree of the variation, implying no variation if $\Delta = 0$. The impedance value of Layer A appearing at the first period is chosen to be $z_a^{(1)} = 0.4z_b$. The present variation induces a gradual impedance decrease from the left to the right in the HQWS below the value of $z_a^{(1)} = 0.4z_b$.

Figures 5.2(b, c) show how the Bloch phase and transmittance are affected by the degree of the impedance variation. Specifically, the results for $\Delta = 0, 0.1,$ and 1 are presented here; the larger value of Δ is the larger amount of the impedance variation in Layers A. In the plots, the center frequencies of the first and second Bragg bandgaps in the unperturbed case (when $\Delta = 0$), $\hat{f} = 0.65$ and 1.35 , and the frequency of the first FPR, $\hat{f} = 1$, are indicated by black dashed lines. Note that the present Bloch phase curves are calculated after regarding the whole (5-period) HQWS structure as a unit superlattice as done in the QWS case.

The phenomena that can be observed in the present HQWS case are similar to those already seen in the QWS case, so brief remarks shall be made here. First of all, regardless of the value of Δ , the preservation of the Bragg bandgaps at around $\hat{f} = 0.65$ and 1.35 are achieved (the preservation of the Bloch phase values at around $\hat{f} = 0.65$ and 1.35 clearly signifies that the original Bragg bandgaps are never disturbed by the variation). Secondly, regardless of Δ , the FPR at $\hat{f} = 1$ is perfectly preserved with a unity transmittance value. Thirdly, variation effects (the localization in the present case) get significant in the other frequency zones as Δ increases. Note that the Bragg bandgaps around $\hat{f} = 0.65$ and 1.35 are observed to get broadened as the value of Δ increases unlike them in the previous QWS case because the average of the impedances of Layers A decreases, or rather, the average of the impedance contrast between the bilayers increases while the phase coherence among the cells fairly remain undisturbed around the frequency zones. Here, another novelty of the proposed impedance-only-variation scheme is found, that is varying impedances do not necessarily be periodic on average to preserve

the locations and the performances of the Bragg bandgaps (while varying thicknesses should be in the conventional geometric variation) even with any distribution type. The novelty may help delicately tailor the transmission characteristics of a PBG structure for various applications while perfectly preserving the Bragg bandgap formation.

5.2.2 Theoretical analysis on the symmetrically impedance-varying phononic bandgap structures

In the previous section, the proposed impedance variation scheme is investigated to effectively tailor the transmission characteristics of a PBG structure while preserving the intrinsic features including the FPR and Bragg bandgap formations. Motivated by the positive consequence of the impedance variation scheme, now the specific impedance distributions in a PBG structure will be investigated which yield a virtually-flattened passband and wide surrounding bandgaps simultaneously. A HQWS structure is employed here because of their intrinsic transmission characteristics: the passband formation around the FPR and the stopband formation symmetrically around the passband.

Begin with a 3-period HQWS structure for investigating the effects of the impedance variation with the symmetric arrangement. The schematic of the structure is depicted in Figure 5.3(a). Only the impedances of half-wave layers, Layers A, are varied while the high-impedances of quarter-wave layers, Layers B, remains unvaried just as before, but with $z_a^{(1)} = z_a^{(3)}$ for the symmetric arrangement.

The specific variations are given by $(z_a^{(1)} + z_a^{(2)} + z_a^{(3)})/3 = 0.12z_b$ and $z_a^{(1)} = z_a^{(3)}$

$= cz_a^{(2)}$ while $1 \leq c \leq 3$. The phase shifts in Layers A and B remain unchanged as $\varphi_a^{(m)} = \pi$ ($m=1, 2, 3$) and $\varphi_b = \pi/2$ respectively at $\hat{f} = 1$ (the normalized frequency with respect to the first FPR frequency) regardless of the c value.

In Figure 5.3(b), variation effects are evaluated specifically on the flatness and steepness of the passband formed around $\hat{f} = 1$ for the varying value of c . For the flatness evaluation, the transitions of T_{dip} (blue open circles) and \hat{f}_{dip} (red crosses) along the c value are investigated in the left plot where T_{dip} refers to the transmittance value at a dip in the passband and \hat{f}_{dip} , the normalized frequency of the dip below $\hat{f} = 1$ (see the leftmost plot in Figure 5.3(c) for the definitions of T_{dip} and \hat{f}_{dip} illustrated in the transmittance curve for $c = 1$). The flatness of the passband is quantified by the ripple factor Q_R (blue open circles) in the right plot in Figure 5.3(b) while the steepness of the passband, by the factor Q_S (red crosses), which are defined as

$$Q_R = \frac{T_{\text{max}} - T_{\text{dip}}}{T_{\text{max}} + T_{\text{dip}}}, \quad Q_S = \frac{B_{-1 \text{ dB}}}{B_{-10 \text{ dB}}} \quad (5.6)$$

where T_{max} indicates the maximum transmittance value in the passband (always unity owing to the non-vanishing FPR at $\hat{f} = 1$) and $B_{-1 \text{ dB}}$ ($B_{-10 \text{ dB}}$), the bandwidth of the passband at the transmittance value of -1 dB (-10 dB). The definitions of T_{max} , $B_{-1 \text{ dB}}$, and $B_{-10 \text{ dB}}$ are also graphically illustrated in the leftmost plot in Figure 5.3(c). In the ideal situation when the passband exhibits a rectangular transmittance curve with the flat top, Q_R will become 0 while $Q_S = 1$.

See the results in Figure 5.3(b). When $c = 1$ (no variation), the passband exhibits

distinct ripples at the top with $T_{\text{dip}} = -0.12$ dB and $\hat{f}_{\text{dip}} = 0.98$ (as seen in the leftmost plot in Figure 5.3(c)) and the evaluation factors are $Q_{\text{R}} = 1.38$ while $Q_{\text{S}} = 0.65$. From the transitions along c , two important findings can be remarked. First of all, T_{dip} reaches its maximum value and \hat{f}_{dip} approaches $\hat{f} = 1$ as the value of c increases, which means that dips get lifted up while moving to the FPR peak at $\hat{f} = 1$ as the variation amount increases (dips completely disappear when $c \geq 2$). Secondly, therefore Q_{R} reaches its minimum value as c increases but the value of Q_{S} decreases, which means that there should be a tradeoff between Q_{R} and Q_{S} performances for making the passband get a flat top and the steep bandedges simultaneously; in this case, an optimal performance for a bandpass filter may be found at $c = 1.5$ when dips are regarded negligible when $T_{\text{dip}} > -0.01$ dB.

It will be interesting to see the detail transmittance curves for the passband formed around $\hat{f} = 1$ for the varying c value. They are shown in Figure 5.3(c): the curve for $c = 1$ (unperturbed case) is shown in the leftmost while the curves specifically for $c = 1.25, 1.5, 1.95,$ and 2.5 , in the center (marked by red lines) with their zoomed views on the passband top beside. In every impedance-varying cases, the curve for $c = 1$ is also shown with black line for the comparison. In the results, the passband is observed to preserve the unity transmittance value at $\hat{f} = 1$ (the FPR frequency) regardless of c owing to the novel consequence of the impedance variation scheme as previously demonstrated. Here, an interesting transition is found along the varying c value: the finite resonant peaks located at the bandedges

approach the FPR peak at $\hat{f}=1$ as c increases while maintaining the unity transmittance values, which leads the dips located approximately in the middles of finite resonant peaks and the FPR peak to be gradually lifted up. Furthermore for $c > 2$, the three peaks completely gather together and the dips consequently vanish in the passband (but the FPR peak at $\hat{f}=1$ still survive with the unity magnitude). Here, emphasis on the unique effects of the symmetrically-arranged impedance variation should be made. While the gradual arrangement contributes to inducing the localization effects in the neighborhoods of the Bragg bandgaps just as the conventional disorder does [135-137], the symmetric arrangement is observed to contribute to shifting the finite resonant peaks in the direction away from the bandgaps while maintaining their unity transmittance values. Such a role of the symmetric variation is understandable when considering the symmetrically-built structures in earlier works [55, 56, 58, 133]. The novel consequence will help make a passband virtually be flattened.

Now, investigate if the passband-flattening performance can be achieved in a general symmetric impedance-varying HQWS structure with the more than 3-period numbers. Specifically, a 5-period HQWS is considered here as depicted in Figure 5.4(a). Following the impedance variation scheme explained in the 3-period case, we simply write down the values of impedances in half-wave layers (Layers A) as

$$\sum_{m=1}^5 z_a^{(m)} / 5 = 0.13z_b \quad \text{and} \quad z_a^{(1)} = z_a^{(5)} = c_1 z_a^{(3)}, \quad z_a^{(2)} = z_a^{(4)} = c_2 z_a^{(3)} \quad (0 < c_2 \leq c_1 < 10).$$

Following four cases are examined:

$$\text{Case 1: } c_1 = 2.50, \quad c_2 = 1.19, \quad \text{Case 2: } c_1 = 3.64, \quad c_2 = 1.48,$$

Case 3: $c_1 = 5.13$, $c_2 = 1.91$, Case 4: $c_1 = 7.69$, $c_2 = 2.70$.

The transmittance curves for the cases are plotted in Figure 5.4(b) and they are also compared with that for the impedance-unperturbed case (the periodic case with $c_1 = c_2 = 1$). Note that the above four cases are selected among the perturbed cases which exhibit negligible ripples ($Q_R < 1.2 \times 10^{-3}$; $T_{\text{dip}} > -0.01$ dB) in the passbands formed around $\hat{f} = 1$ through the analysis following the similar procedure shown in the 3-period case.

Although it is not shown here in detail, four finite resonance peaks in the passband around $\hat{f} = 1$ tend to approach the FPR peak at $\hat{f} = 1$ as the c_1 and/or c_2 values increase just as observed in the 3-period case. At the specific values of c_1 and c_2 (about 2.50 and 1.19 respectively in the present case; Case 1), the finite resonance peaks are observed to be located at the quite adjacent frequencies to the FPR peak, leading to the existence of negligible ripple in the passband (see the zoomed curve on the passband top around $\hat{f} = 1$ for Case 1). As c_1 and c_2 increase above them in Case 1, finite resonance peaks and the FPR peak gather together and ripples completely disappear in the passband as seen in results for Cases 2-4 while the slopes of bandedges decrease ($Q_S = 0.75$, 0.66, 0.57, and 0.43 for Cases 1 to 4, respectively). The phenomena observed here well follow them in the previous 3-period case, and the symmetrically-arranged impedance-variation scheme on a HQWS is confirmed to yield a quasi-ideal bandpass filter performance when the distribution is suitably selected.

It may be worth noting on the period number of a symmetrically-varying HQWS structure. First, with the more period numbers, there exist more freedoms to vary

the distributions of the impedance variation. Specifically, two parameters c_1 and c_2 are available in the present case dealing with the 5-period case while only one parameter, c in the 3-period case. Therefore, it is possible to delicately tailor the transmittance characteristics (such as convexness of the passband) by tuning the distributions when more period numbers than three are used. Secondly, with the more period numbers, more finite resonance peaks should exist in the passband formed around $\hat{f}=1$, leading the peaks to span a wider frequency range in the passband. Therefore, it is possible to get steeper bandedges with the flattened top. Specifically, the best value of Q_s shown in the present 5-period case is 0.75 while that for the previous 3-period case, 0.60. This argument may be also supported by Figure 5.5, which compares the bandpass filtering performances of symmetric impedance-varying HQWS structures with the period numbers varying from 3, 5 to 7. In each case, the distributions of the impedance are optimally selected to yield a good filter performance while the minimum impedance values for half-wave layers ($z_a^{(2)}$, $z_a^{(3)}$, and $z_a^{(4)}$ for the 3-, 5-, and 7-period cases, respectively) are all set to be $0.08z_b$ (the minimum value which can be obtained by using the proposed metamaterial in the following section). The detailed impedance distributions are as follows:

$$\text{3-period case: } c = 1.67, \quad \text{5-period case: } c_1 = 2.38, \quad c_2 = 1.19,$$

$$\text{7-period case: } c_1 = 2.5, \quad c_2 = 1.28, \quad c_3 = 1 \quad (c_m = z_a^{(m)} / z_a^{(4)}; m=1, 2, 3)$$

The cases achieve virtually flattened tops with negligible ripples ($Q_R < 1.2 \times 10^{-3}$; $T_{\text{dip}} > -0.01$ dB) in the passbands around $\hat{f}=1$ as well as the wide and deep surrounding bandgaps in common while exhibiting the varying values of Q_s such

as 0.58, 0.77, and 0.86 for the 3-, 5-, and 7-period cases respectively. The present bandpass-filter-performing HQWS structures will be realized through using elastic metamaterials in the following section.

5.3 Proposition of Impedance-Only-Varying Elastic Metamaterials

It is not easy to realize an impedance-varying HQWS structure through using solid materials in nature because characteristic impedance depends on wave velocity so tuning the values of impedance and phase shift in a material slab independently is not possible. Even though tuning the value of phase shift only while maintaining the impedance value can be realized through adjusting the thickness of a layer, it is still impossible to apply the scheme for realizing a bandpass filter using the HQWS structure because the performance cannot be unrestrictedly controlled.

So, metamaterials alone should be the scheme to realize the proposed impedance-varying HQWS structures. They can possess a large variety of impedances while exhibiting the specific value of phase shift simply by designing the suitable constituent elements of metamaterials. Furthermore the use of metamaterials instead of materials in nature leads to the simple fabrication of a stratified structure. In this section, simply-configured metamaterials will be proposed which exhibit impedance-only-varying behaviors, and the impedance-varying HQWS structures will be realized by using the metamaterials. The S-parameter retrieval method [35, 36] is adopted here for the characterization of the metamaterials.

5.3.1 Configurations of the proposed metamaterials

See Figure 5.6, which shows the schematic of the proposed metamaterial slab

doing a role as a homogeneous layer. It is constructed by using slit-shaped void inhomogeneities into an aluminum substrate (mass density $\rho = 2700 \text{ kg/m}^3$, Young's modulus $E = 71 \text{ GPa}$, Poisson's ratio $\nu = 0.33$). The imaginary boundaries of the unit cell composing the slab are marked by black dashed line, and the zoomed view is shown in the right side with the design parameters also illustrated: L_x and L_y are the lattice constants along the x - and y -directions respectively while w and h , the slit width and the height respectively and s , the separation distance of the slits with their centers in the x -direction. For a simple design, the lattice constant in the y -direction L_y , the slit width w , and the separation distance s are fixed as 6.3, 0.2, and 0.5 mm, respectively.

Note that the lattice constant in the x -direction, L_x is employed as a varying parameter in addition to the slit height, h in order to achieve a wide variety of effective properties while constructing the metamaterials just with the slit-shaped inhomogeneities (see Figure 5.7 specifically for the impedances of the metamaterial having the varying values on the parameters L_x and h , relative to that for aluminum). In usual metamaterial designs [90, 104, 142], only the constituent elements in a unit cell are targeted to be designed while the lattice constants are fixed, which usually leads to the complex configuration for the elements. In this study, on the other hand, the constituents are set to be slit-shaped except the height h while using the varying lattice constants in the x -direction, leading to the simple configuration.

In order to verify that the proposed metamaterial slabs are capable of doing roles as half-wave slabs, the effective properties are investigated for the varying values of

the design parameters including L_x and h in Figure 5.7. Specifically, the relative impedance value of the metamaterial at $f = 100$ kHz (the targeted center frequency of a flattened passband) is shown with respect to the value of aluminum. The design parameters satisfying the half-wave condition when a single metamaterial slab is doubly disposed ($n(2L_x) = \lambda_0/2$ where n : refractive index of a metamaterial slab at $f = 100$ kHz, λ_0 : the wavelength in aluminum) are indicated by black line and the parameters falling in the boundary of the Bragg regime of metamaterials [95], by white line. The parameters for the metamaterial slabs (MM-I to MM-III) composing the 5-period HQWS structure, which will be shown in Figure 5.11, are also marked by black circles.

Despite only the two varying design parameters (h and L_x) are used even with the simple configuration, the proposed metamaterial is shown to possess a wide variety of impedances from the comparable value to it of aluminum (z_b) up to a somewhat extreme value while maintaining the value of phase shift to be π (see black solid line). It signifies that the employment of L_x as a varying parameter contributes to achieving a wide variety of impedances while satisfying the required values of refractive indices specifically for half-wave layers. Referring to the continuous distribution for the half-wave candidates, it is now possible to delicately tune the impedance of a half-wave layer by using the proposed metamaterial slab.

5.3.2 Effective-property characterization by the S-parameter retrieval method

In order to determine the effective properties of the proposed metamaterial, the S-

parameter retrieval method is employed here. Since the present case deals with the wave propagation of a longitudinal wave just in the x -direction, the conventional method can be used specifically for yielding the normal stiffness component in the x -direction, C_{11} and mass density, ρ .

A brief comment on how to confirm the bulk property [93, 94] of the present half-wave metamaterial will be briefly made here. The bulk property should be confirmed specifically in the present case where the lattice constant L_x is employed as a varying design parameter because the bulk property cannot be guaranteed especially when L_x is significantly small. The usual method confirming it after comparing the effective properties of a single and multiple cells [93, 94], however, cannot be adopted here because the effective properties cannot be retrieved at the FPR frequency [36].

Recall Eq. (3.26), which shows the way that the effective impedance is derived from the S-parameters:

$$\left(\frac{z^\alpha}{z_0^\alpha}\right)^2 = \frac{(1 + RLL)^2 - SLL^2}{(1 - RLL)^2 - SLL^2}$$

If RLL approaches 0 while SLL , 1, the impedance value becomes unstable and meaningless. The phenomenon occurs at the FPR frequency. So instead of the usual method using the effective properties, the method evaluating the S-parameters [36] is adopted here. Even though the results are not shown here, the proposed metamaterial is found to exhibit fairly good bulk property even for $L_x = 1.8$ mm.

The detail effective properties are shown in Figure 5.8 specifically for the metamaterial slabs (MM-I to MM-III) whose design parameters are already shown in Figure 5.7: impedance relative to it of aluminum (z_a/z_b) in the top-left,

refractive index (n_a) in the top-right, mass density (ρ_a) in the bottom-left, the normal component of stiffness (C_a) in the bottom-right. Here, only the real values are presented below the Bragg regimes of the metamaterials and the imaginary values are negligibly small in the present frequency range.

Here, it may worth noting on the different characteristics of (positive-index) elastic metamaterials compared with them of acoustic metamaterials [51, 92, 142]. See the results for ρ_a and C_a where the following observations can be made:

Observation 1: in the low frequency region far below the Bragg regime, the value of stiffness is significantly small relative to that for aluminum ($C_b = 105$ GPa) while the mass density is rather comparable ($\rho_b = 2700$ kg/m³)

Observation 2: for MM-I to MM-III, the stiffness values largely vary among each other while the mass density values do not.

The observations signify that the present model achieves extreme properties mainly from the stiffness, and stiffness does a crucial role in determining the characteristics of metamaterials in the elastic regime while mass density does in acoustics [51, 92, 104].

5.3.3 Realization of the impedance-varying HQWS structures

By using the proposed metamaterial slabs for impedance-varying half-wave layers while an aluminum substrate for quarter-wave layers, an effective HQWS is built as illustrated in Figure 5.9 (the structure is periodically disposed in the y -direction). The imaginary boundaries of a half- and a quarter-wave layers are indicated by red

dashed lines while the boundary between two unit metamaterial cells by black dashed line. Note that two cells are used here for designing a half-wave layer because of the Bragg regime of metamaterials [95].

In order to verify that the metamaterial slabs are capable of doing roles as half-wave slabs while exhibiting the impedance-only-varying behaviors in an overall working frequency range, the phase shifts in the slabs (a) and the impedances normalized to each value at 100 kHz (b) are investigated in Figure 5.10 after employing the slabs MM-I to MM-III, whose detail properties are already shown in Figure 5.8. The properties for MM-I to MM-III are indicated by blue, red, and green dots respectively while the targeted properties, by black lines.

Some discrepancies are found between the properties realized by using the metamaterial slabs and the target properties. When considering the present metamaterial slab covers a fairly broad frequency range, however, the discrepancy due to the dispersions in the effective properties is rather natural. In spite of the dispersions, the designed slabs are found to well work as half-wave layers in a broad frequency range around the target frequency, 100 kHz while yielding the fairly identical behaviors among each other. The identical behaviors indicate that the slabs MM-I to MM-III exhibit the property variations just in their impedances while do not in the phase shifts surprisingly in a broad frequency range and the impedance variation ratio is also well maintained along the frequency.

The achievement of the impedance-only-varying behaviors may be owing to the simple configuration of the proposed metamaterials, whose geometries do not differ that much along the design parameters. It is accomplished without any help of an optimization scheme to fit the behaviors of metamaterials with each other.

5.4 Design of Quasi-Ideal Bandpass Filters

In the previous sections, the proposed impedance-variation scheme is investigated to effectively tailor the transmission characteristics of PBG structures while preserving the intrinsic features including the FPR and Bragg bandgap formations. Motivated by the positive consequence of the impedance variation scheme, quasi-ideal bandpass filters are proposed after designing specific impedance-varying PBG structures which have virtually-flattened passband tops and wide surrounding bandgaps simultaneously.

In this section, the theoretically developed impedance-varying HQWS structures will be realized through using the proposed metamaterial slabs and the performances will be investigated. The validity of employing the metamaterial slabs for realizing the impedance-varying HQWS structures will be shown.

5.4.1 Validation of the performance by FEM simulations

Here, the performances of designed metamaterial-based impedance-varying HQWS structures will be analyzed and the bandpass-filtering performances will be compared with the theoretically estimated ones studied in the previous section.

In Figure 5.11, the 3-, 5-, and 7-period cases are examined after adopting the detail arrangements of impedance variations from each case shown in Figure 5.5 but with the minimum impedance value as $z_a^{(m)} = 0.10z_b$ ($m = 2, 3, 4$ for the 3-, 5-, 7-period cases respectively). The detailed configurations of the designed HQWS structures are depicted in Figure 5.11(a) and their transmittance curves, in Figure

5.11(b) with red dots (theoretical curves simulated by using homogeneous target materials with blue solid lines). Note that the geometries of the constituent metamaterials are derived on the basis of their effective properties at the target frequency, $f = 100$ kHz (the FPR frequency) because the properties are dispersive along frequency as already mentioned. The selected design parameters for the metamaterials are as follows: $L_x = [3.5, 2.2, 3.5]$ mm, $h = [3.4, 3.6, 3.4]$ mm along the period in the 3-period case, $L_x = [4.8, 2.6, 2.2, 2.6, 4.8]$ mm, $h = [3.3, 3.5, 3.6, 3.5, 3.3]$ mm in the 5-period case, and $L_x = [5.1, 2.8, 2.2, 2.2, 2.2, 2.8, 5.1]$ mm, $h = [3.3, 3.5, 3.6, 3.6, 3.6, 3.5, 3.3]$ mm in the 7-period case.

See the transmittance curves in Figure 5.11(b). The designed metamaterial-based structures exhibit the virtually flat tops in the passband formed around $f = 100$ kHz (the minimum value of T_{dip} is -0.012 dB (0.997) in the 3-period case while $T_{\text{dip}} > -0.01$ dB in the 5- and 7-period cases) and the wide surrounding bandgaps simultaneously. While the curves fairly correspond to the theoretically estimated ones in respect to the steepness of the passband: $Q_s = 0.57, 0.76, 0.86$ in the 3-, 5-, 7-period metamaterial models respectively while $0.57, 0.75, 0.85$ in the target models), some discrepancies are found between the results, which can be summarized in the following three statements. First, the passband around $f = 100$ kHz is narrower in the metamaterial model than that in the target model (about 2 kHz narrower in average for the three cases at the transmittance value of -3 dB). Secondly, the lower bandedge frequency for the first bandgap (located at the left side with respect to $f = 100$ kHz) is higher in the metamaterial model (about 17.8 % higher in average at the -3 dB transmittance). Thirdly, there is no

specific bound for the upper bandedge of the second bandgap in the metamaterial model. The main reason for the discrepancies should be the dispersions in the effective properties of the metamaterials, and it shall be demonstrated in the following few paragraphs in more details. In spite of the discrepancies, the metamaterial-based structures yield quasi-ideal bandpass-filter performances as theoretically estimated. It is a remarkable achievement because the present metamaterials cover a quite broad frequency range so the dispersions in their effective properties are natural.

Now, the performances of the designed structures will be analyzed in more detail by looking at the scattering parameters, specifically S_{12} of the constituent half-wave metamaterial slabs. Only the 5-period case in Figure 5.11 is considered here. Figure 5.12 shows the magnitudes (in the left column) and phases (right column) of S_{12} for MM-I to MM-III with red dots while those for the target slabs, with black lines. Before interpreting the results, remind that the targeted properties for MM-I to MM-III are $z_a^{(1)} = 0.238z_b$, $z_a^{(2)} = 0.119z_b$, and $z_a^{(3)} = 0.100z_b$ respectively while $\varphi_a^{(1)} = \varphi_a^{(2)} = \varphi_a^{(3)} = \pi$ at $f = 100$ kHz.

All the slabs are observed to exhibit the FPRs exactly at $f = 100$ kHz while MM-II yields the more sticking-out peak than MM-I does and MM-III, than MM-II. It means that the designed slabs fairly work as impedance-varying half-wave layers as targeted. Then, see the asymmetric responses appearing in the S_{12} curves with respect to $f = 100$ kHz, which can be demonstrated by employing the results for phase shifts and impedances of the slabs already shown in Figure 5.10. In the low frequency zone ($f < 100$ kHz), the fact that the metamaterial slabs possess the

slightly small values of phase shifts compared to the target values while the large values of impedances leads the phases of S_{12} to get slightly small while the magnitudes to get large compared to them of the target. In the high frequency zone ($f > 100$ kHz), on the other hand, the fact that the slabs possess the large values of phase shifts compared to the target values while the small values of impedances below the Bragg regimes leads the phases of S_{12} to get large while the magnitudes to get small compared to them of the target.

The asymmetric responses of the metamaterial slabs yield the discrepancies in the transmittance curves between the metamaterial and target models as shown in Figure 5.11. More precisely speaking, they lead the first bandgap to develop at a slightly higher frequency region than that from the target model with the smaller bandwidth and the second bandgap to develop at the lower frequency region with the larger bandwidth.

The performances of the designed structures are also analyzed by the effective medium models, and the result specifically for the 5-period case is presented in Figure 5.13. Figure 5.13(a) shows the transmittance curves obtained from the detailed (blue solid line) and the effective medium (red dots) models and Figure 5.13(b), the x -directional velocity fields (v_x) in the two models at the center frequency of the passband ($f = 100$ kHz). The detail magnitudes of v_x along the mid-plane aligned in the x -direction are compared in the bottom plot. The index λ_0 in the figure denotes the wavelength at $f = 100$ kHz in aluminum ($\lambda_0 = 6.24$ cm). The results from the two models are well matched with each other, meaning that the metamaterial slabs successfully do roles as homogeneous materials. Note that the confinement of propagating waves in specific metamaterial slabs (slabs at the

second and fourth periods in the present case) indicates that the slabs will yield the FPRs as targeted.

5.4.2 Tailoring of the bandpass-filter performance

One of the strengths of the proposed design scheme using impedance-varying HQWS structures for bandpass filters lies on the fact that the bandwidth of a targeted passband can be flexibly controlled by adjusting the average of impedance contrasts between the constituent half- and quarter-wave layers just as in the conventional PBG structures [69, 129]. The flexible control can be accomplished by the help of our proposed metamaterials, which can possess a wide range of impedances. The argument can be supported by the transmittance curves in Figure 5.14 for the impedance-varying HQWS structures constructed with the metamaterial slabs yielding the varying value of z_{avg} where z_{avg} indicates the average of the effective impedances defined as

$$z_{\text{avg}} = \frac{\sum_{m=1}^N z_a^{(m)}}{N} \quad (5.7)$$

with the period number, N .

The 5- and 7-period cases are examined in Figures 5.14(a, b) respectively after employing the detail arrangements of impedance variations from the each case presented in Figure 5.11 but with the varying value of z_{avg} . Performances of the 5-period cases are examined first specifically for $z_{\text{avg}} = 0.13z_b$, $0.20z_b$, and $0.26z_b$ (z_b : impedance of aluminum). As the value of z_{avg} increases, or rather, the impedance contrast between the constituent bilayers decreases in average, the

bandgaps surrounding the targeted passband get narrower and consequently the passband get wider. So, the values of Q-factors [59] distinctively vary from case to case as 13.3 (for $z_{\text{avg}} = 0.13z_b$), 9.1 ($0.20z_b$), and 7.0 ($0.26z_b$). The factors Q_R and Q_S , on the other hand, are observed to be similar among each case as $Q_R \ll 0.01$ (the minimum value of T_{dip} is above 0.997; -0.014 dB) while $Q_S \approx 0.74$ for the cases. The phenomena observed in the 7-period cases also follow them in the 5-period cases while the Q-factors are 13.7, 9.3, and 7.2 for $z_{\text{avg}} = 0.12z_b$, $0.18z_b$, and $0.24z_b$ respectively and $Q_S \approx 0.84$ regardless of z_{avg} .

The capability of tailoring the bandwidth of a passband in a very simple way, just by tuning the value of z_{avg} , is accomplished owing to the novel consequence of the proposed impedance-variation scheme, which preserves the intrinsic formation of the Bragg bandgaps regardless of the variation.

5.5 Summary

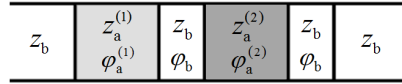
In this study, a novel methodology for designing a quasi-ideal bandpass filter is suggested, which is varying the characteristic impedances of half-wave layers in a HQWS structure with the symmetric arrangement while keeping the phase shifts unchanged. Beyond the theoretical analysis on it, the bandpass filters are realized by using the simply-configured elastic metamaterials.

The impedance-only-variation scheme shows unique consequences compared to the conventional thickness variation scheme. Because it preserves the phase coherence among the cells specifically at the Bragg bandgap and FPR frequency

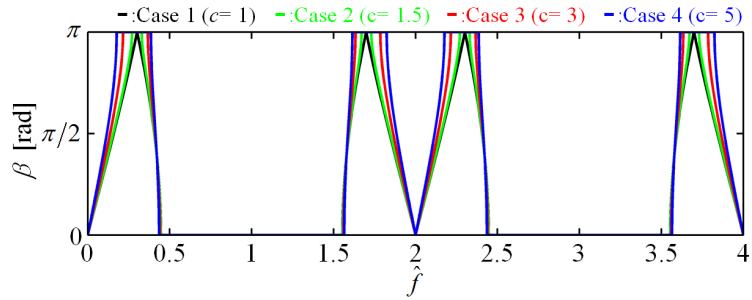
regions while disturbing them only at other frequency zones, the impedance-varying structures can still exhibit the intrinsic formation of the Bragg bandgaps and FPRs while achieving the variation effects in the neighborhoods of the Bragg bandgaps. This positive consequence helps effectively tailor the transmission characteristics of a PBG structure through tuning the arrangement and amount of the variation. Especially for the symmetric arrangement into a HQWS structure, the variation scheme surprisingly contributes to flattening the passbands forming around the FPRs, through shifting the finite resonance peaks to a FPR peak while maintaining their unity transmittance values. Implementing the symmetrically-arranged variation scheme by using the positive-index elastic metamaterials, quasi-ideal bandpass filters are successfully realized. They achieve the distinct formations of a passband and the wide surrounding bandgaps with the virtually flattened tops at the passband as well as the steep bandedges.

The proposed elastic bandpass filters and the design methodology are expected to be utilized specifically for non-destructive evaluation and medical imaging devices. Furthermore, the impedance variation scheme may give a great contribution to tailoring and improving the performance of a PBG structure.

(a) Impedance-varying 2-period QWS



(b) Bloch phase



(c) Transmittance

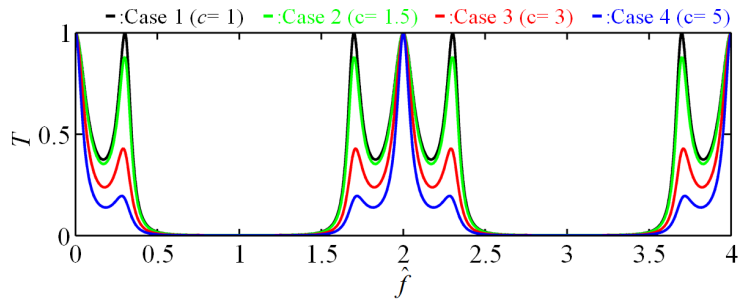
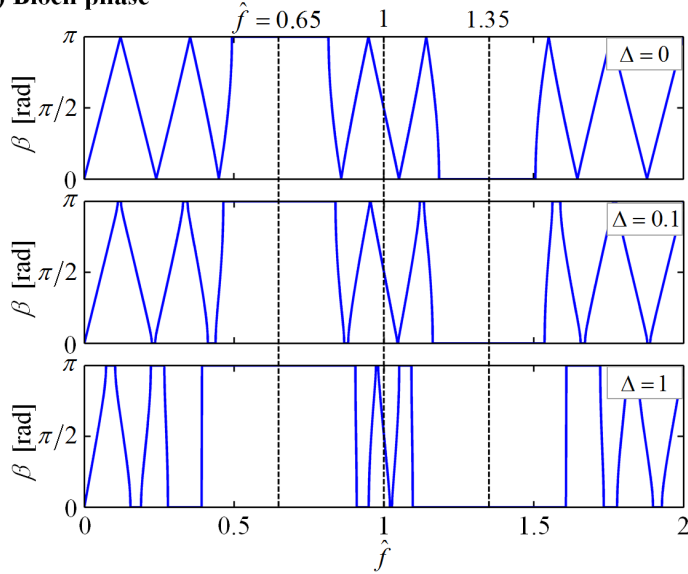


Figure 5.1 (a) The schematic of an impedance-varying 2-period QWS structure and (b) the Bloch phases and (c) the transmittances for the varying value of c

(a) Impedance-varying 5-period HQWS



(b) Bloch phase



(c) Transmittance

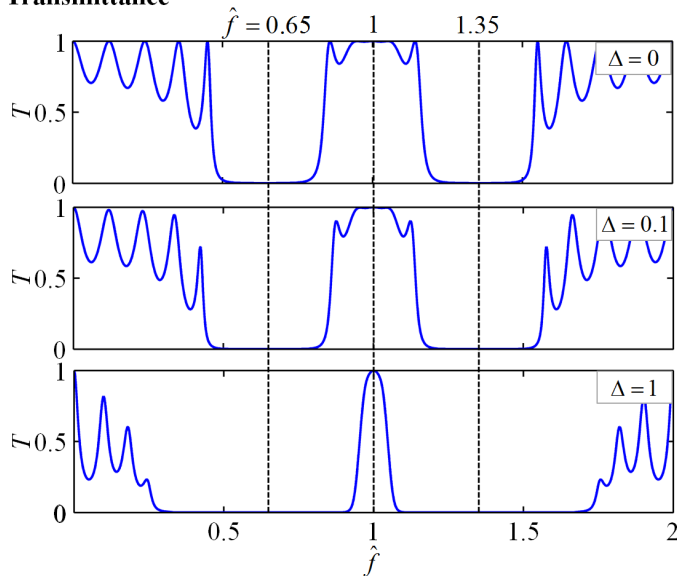
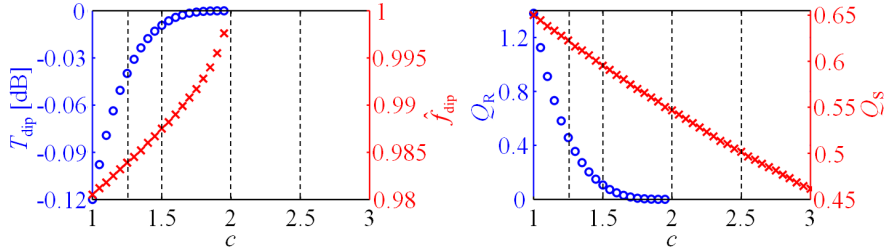


Figure 5.2 (a) The schematic of an impedance-varying 5-period HQWS structure and (b) the Bloch phases and (c) the transmittances for the varying value of Δ

(a) Symmetrically impedance-varying 3-period HQWS

$Z_a^{(1)}$	Z_b	$Z_a^{(2)}$	Z_b	$Z_a^{(3)}$	Z_b
$\varphi_a^{(1)}$	φ_b	$\varphi_a^{(2)}$	φ_b	$\varphi_a^{(3)}$	φ_b

(b) Variation effects



(c) Transmittance

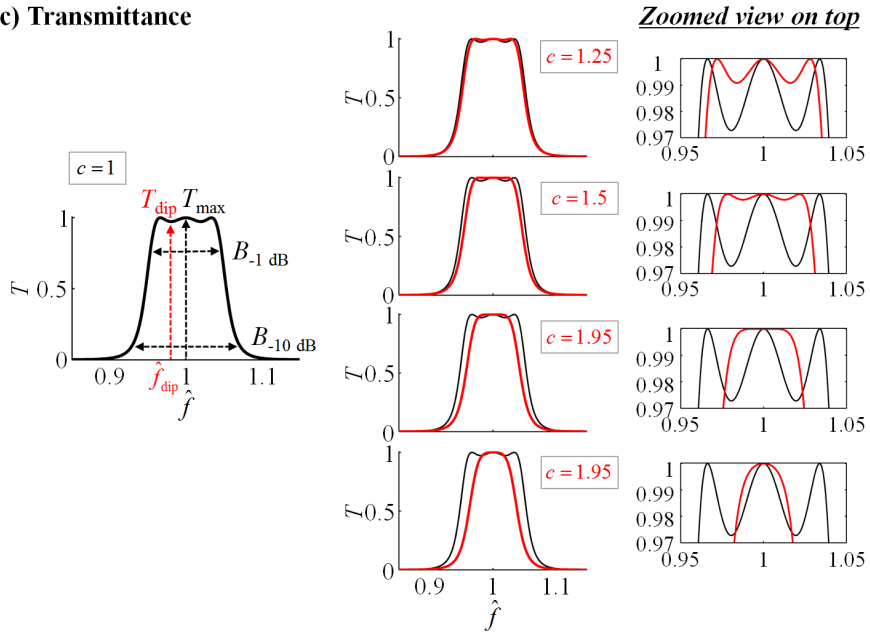


Figure 5.3 (a) The schematic of a symmetrically impedance-varying 3-period HQWS structure, (b) the transitions of T_{dip} , \hat{f}_{dip} , Q_R , and Q_S for the varying value of c , and (c) the transmittance spectra for the specific values of c

(a) Symmetrically impedance-varying 5-period HQWS

$z_a^{(1)}$	z_b	$z_a^{(2)}$	z_b	$z_a^{(3)}$	z_b	$z_a^{(4)}$	z_b	$z_a^{(5)}$	z_b
$\phi_a^{(1)}$	ϕ_b	$\phi_a^{(2)}$	ϕ_b	$\phi_a^{(3)}$	ϕ_b	$\phi_a^{(4)}$	ϕ_b	$\phi_a^{(5)}$	ϕ_b

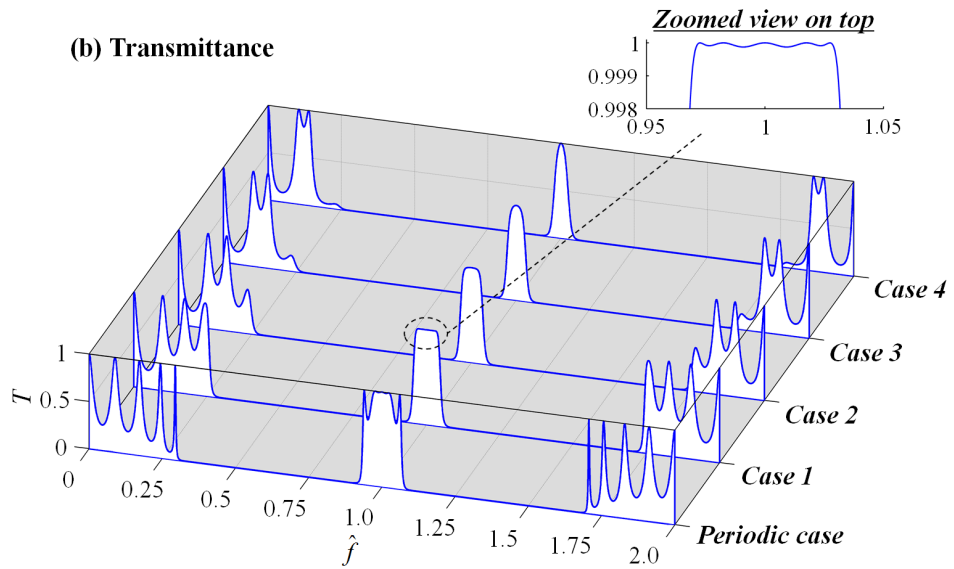


Figure 5.4 (a) The schematic of a symmetrically impedance-varying 5-period HQWS structure and (b) the transmittance spectra for the periodic case and Cases 1-4

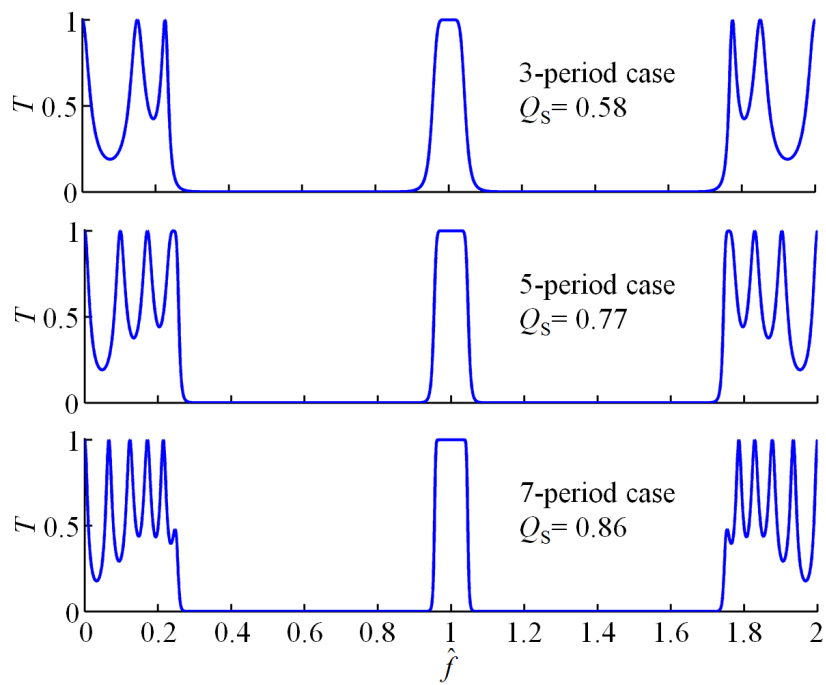


Figure 5.5 The transmittance spectra for the 3-, 5-, and 7-period cases

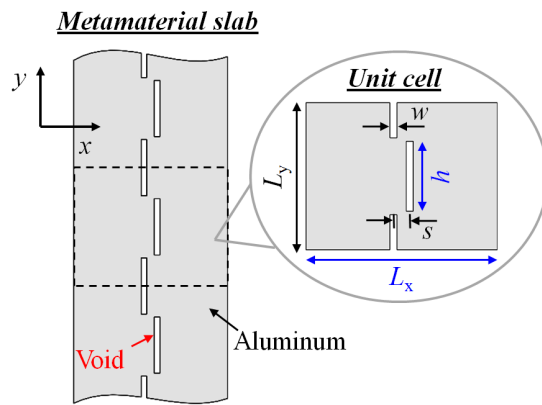


Figure 5.6 The schematic configuration of the proposed metamaterial slab

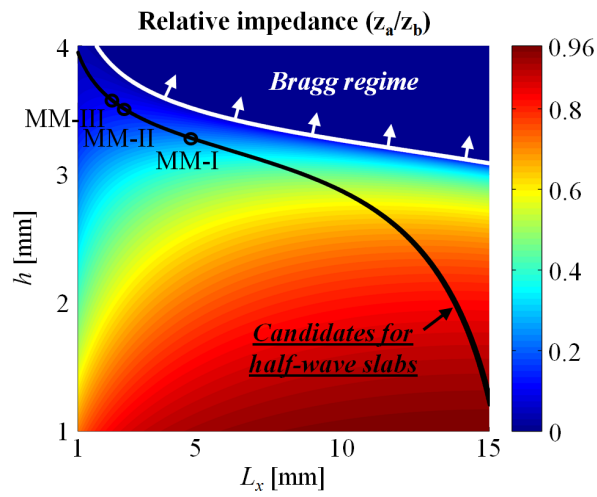


Figure 5.7 The impedances of the proposed metamaterials relative to that of aluminum for the varying design parameters L_x and h

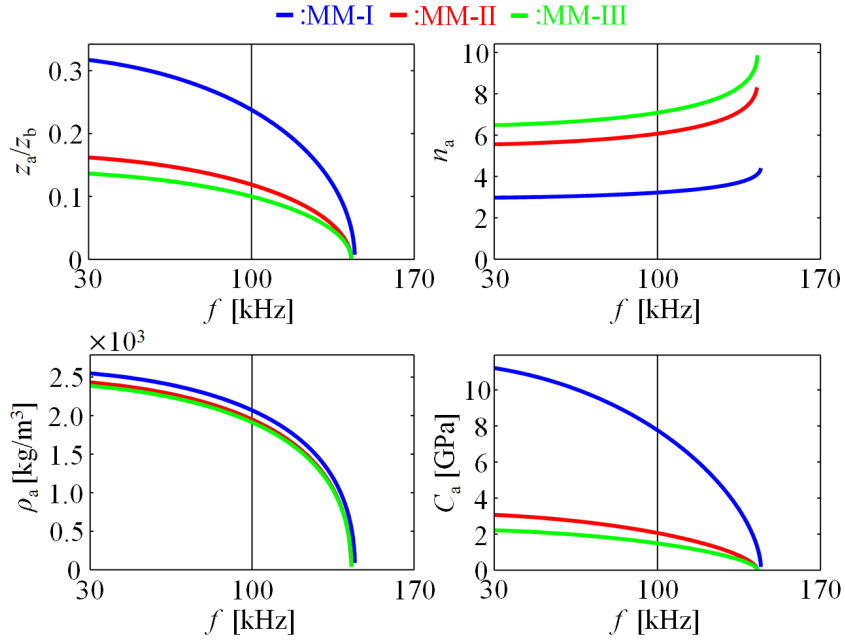


Figure 5.8 The effective properties of MM-I to MM-III: relative impedance (top-left), refractive index (top-right), mass density (bottom-left), and normal stiffness (bottom-right)

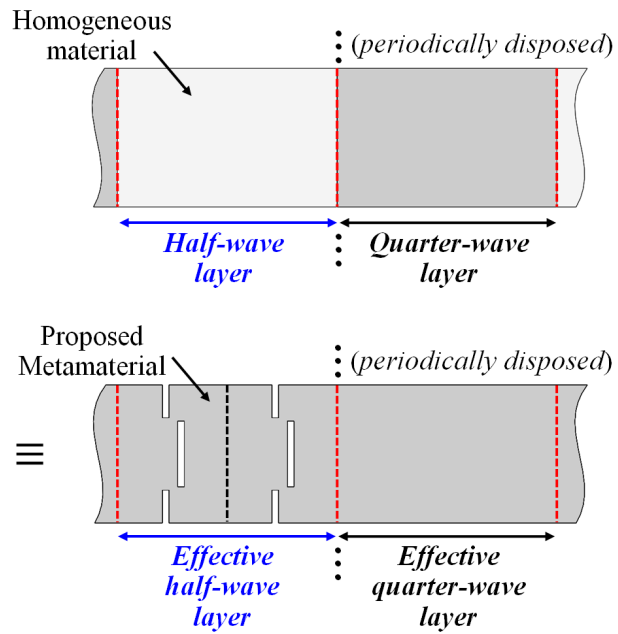
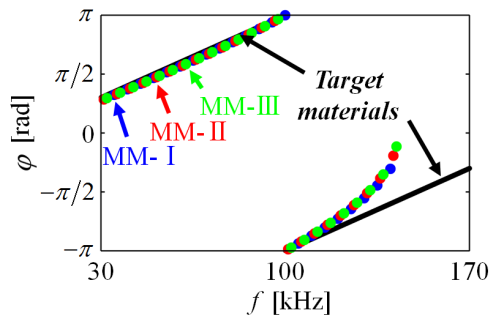


Figure 5.9 The schematic configuration of an effective HQWS realized by using the proposed metamaterial slabs

(a) Phase shift in a half-wave metamaterial slab



(b) Impedance normalized to the value at 100 kHz

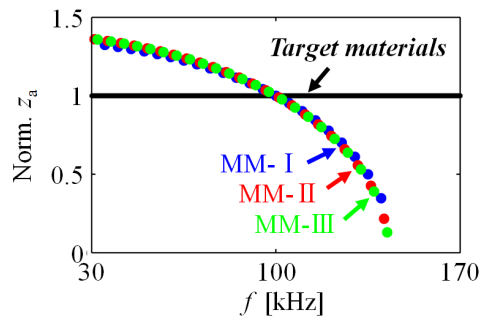


Figure 5.10 (a) The phase shifts in the half-wave metamaterial slabs of MM-I to MM-III and (b) their impedance values normalized to each value at 100 kHz

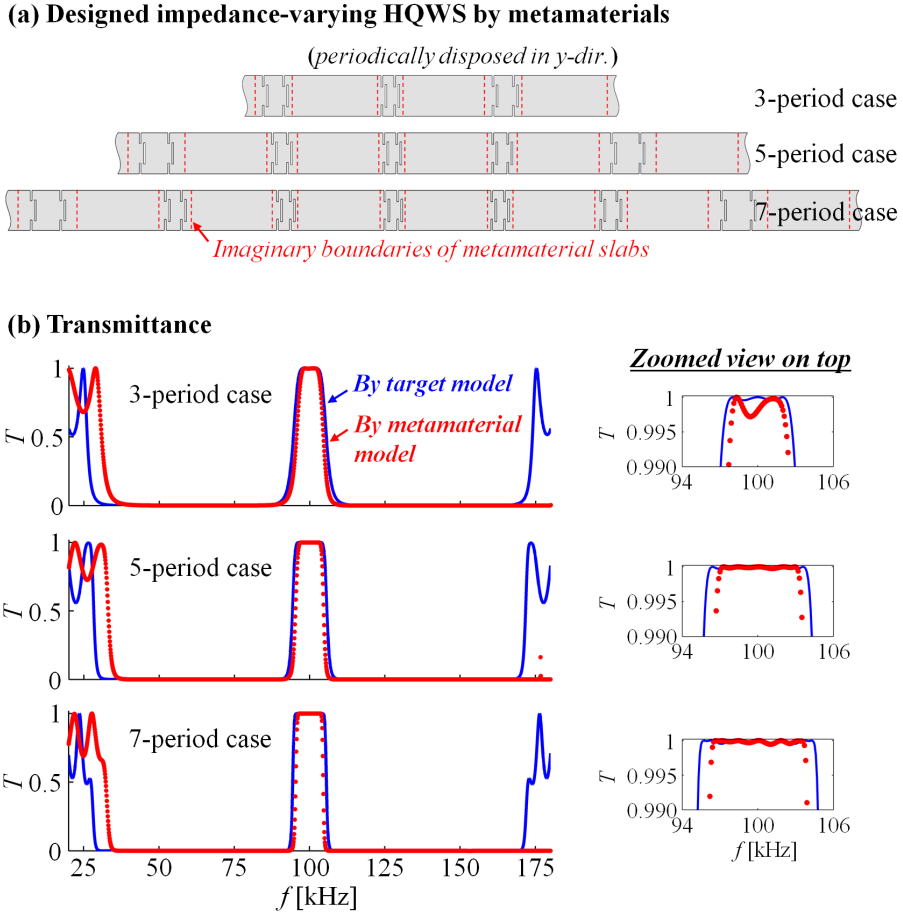


Figure 5.11 (a) The schematic of the symmetrically impedance-varying HQWS structures designed by metamaterials and (b) their transmittance spectra

S_{12} of half-wave metamaterial slabs

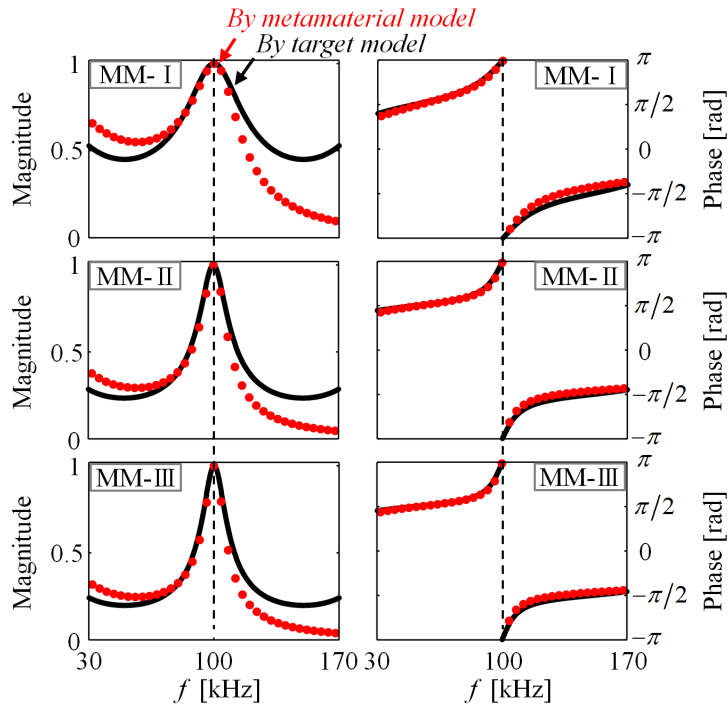


Figure 5.12 The scattering parameters S_{12} of the half-wave metamaterial slabs,

MM-I to MM-III

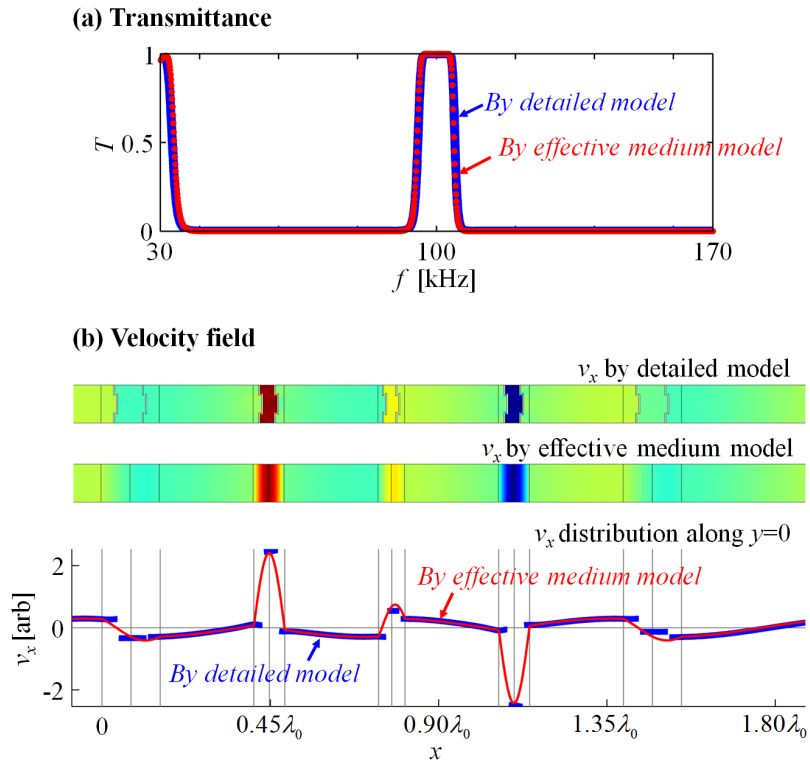


Figure 5.13 (a) The transmittance spectra analyzed by the detailed and the effective medium models and (b) the distributions of the x -directional velocity fields inside the models at 100 kHz

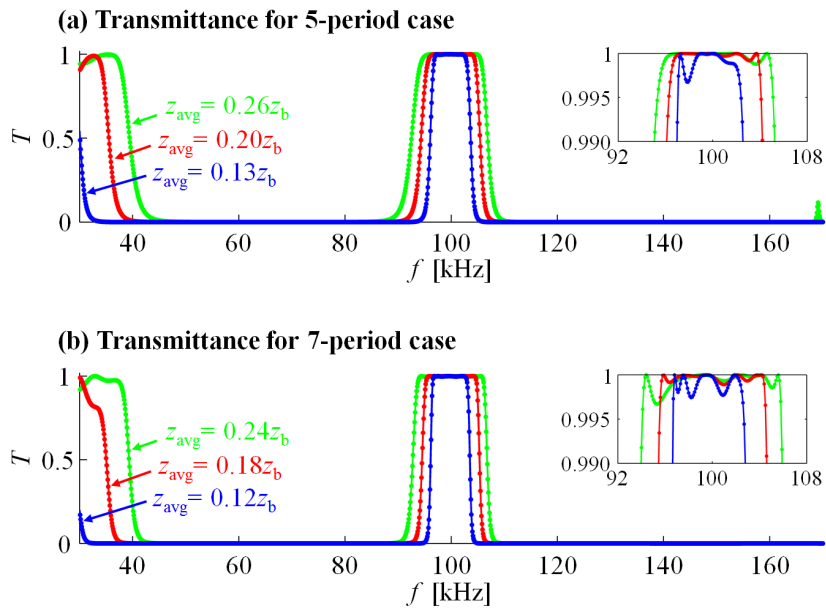


Figure 5.14 The transmittance spectra for the designed (a) 5- and (b) 7-period HQWS structures with the varying value of z_{avg}

CHAPTER 6.

Design of Wave Mode Converters by Using the Elastic Metamaterials Exhibiting Anomalous Polarizations

6.1 Wave Mode Converters

In general bulk isotropic elastic media, there exist two wave modes including longitudinal and transverse (shear) wave modes [47, 48, 64, 65]. The two modes exhibit distinctively different polarizations with each other: a longitudinal mode possesses the parallel particle motion with respect to the propagation direction while a transverse mode, the perpendicular particle motion. Originating from the distinct polarization characteristics, they each are sometimes utilized for specific applications. Specifically, a transverse mode gets some strengths over a longitudinal mode in the nondestructive evaluation (NDE) area, that are it is sensitive to weld defects as well as crack-like defects and its minimum detecting flaw resolution is smaller than that of a longitudinal mode [122, 143-146].

In spite of the strengths of a transverse mode, the use of the mode has some issues: directly generating it into a guided elastic substance is not easy by using the conventional piezoelectric transducers and generating it into a bulk solid at the normal incidence requires the transducer only for the mode [48, 60, 61]. There also exist some issues on the large energy attenuation as well as the slow propagation velocity when a transverse wave is transmitted through a waveguide for diagnosing the structures deeply buried in soil or immersed in water [62, 63, 147]. So, mode converting systems dealing with the conversion of a longitudinal mode to a

transverse mode is highly demanded specifically in the NDE area.

In order to realize the mode converter yielding a pure transverse wave as the output, one can utilize the critical angle scheme [48, 60, 61, 148], which is the most well-known and widely-used technique in the NDE area. The technique works at the boundary between two different materials (one should be stiffer than the other) when transferring a longitudinal wave to the boundary at a specific oblique incident angle whose tangential wavenumber should be greater than it of a longitudinal wave in the other stiffer material while lesser than it of a transverse wave. The critical-angle-based converting technique, however, has some limitations: (1) the incident angle of a longitudinal wave should be a lot carefully chosen and adjusted for yielding a transverse wave at a specific angle as the output, (2) the incident angle for the transverse wave output at a specific angle differs case by case depending on the properties of the two materials, (3) the two material properties should be significantly differ for achieving the critical-angle condition, which leads (4) the converting ratio usually to be small as the incident angle increases, and (5) the transverse wave output at the normal to the boundary cannot be achieved through using the technique.

In earlier studies on phononic crystals (PCs), several works have shown a possibility that mode conversion can be achieved by employing the asymmetrically-configured structures [149, 150]. However, the structures themselves cannot yield pure wave mode conversion due to the existence of coupling phenomenon between two wave modes in the structures, so additional systems are required for sorting out a pure wave mode, which usually leads the systems to have the large dimensions.

In this study, a novel methodology is suggested for achieving wave mode converting systems which deal with a pure transverse wave as the output for a longitudinal wave incidence while yielding the output at the normal to the system surface. The proposed mode converter is realized through using the three major schemes: (1) an anomalous polarization characteristic, (2) wave refraction at the surface of systems, and (3) elastic metamaterials. In general bulk anisotropic solid materials, wave modes usually can be classified into two as a quasilongitudinal and a quasitransverse modes by using the EFC profiles (when only the waves exhibiting the in-plane motions are considered): the EFC profile having smaller wavenumbers usually corresponds to a quasilongitudinal mode while the profile having larger wavenumbers, a quasitransverse mode [47, 48]. For a specific material, however, such a classification of the wave modes is not available [151-153]. When a material possesses the larger value of shear stiffness than one of the normal stiffness components, the relative angle between a polarization and a propagation (\mathbf{k}) directions changes from 0 to 90 degrees in each EFC, which means that wave mode transitions develop in each EFC from a purely longitudinal (transverse) to a purely transverse (longitudinal) modes along the propagation direction. By employing the materials exhibiting such an anomalous polarization characteristic, novel wave mode converters are proposed with the scheme of wave refraction [47, 48, 91], which enables wave mode to switch from a purely longitudinal to a purely transverse modes. Then the proposed methodology for mode converters is realized through using positive-index elastic metamaterials. The present chapter consists of two main parts. One introduces the elastic metamaterials exhibiting the anomalous polarization characteristic and the other

shows the performances of designed mode converters consisting of the proposed metamaterials, which will be shown in Sections 6.2 and 6.3 respectively. Section 6.4 deals with the summary of the chapter.

6.2 Proposition of Elastic Metamaterials Exhibiting Anomalous Polarizations

In this section, elastic metamaterials exhibiting an anomalous polarization characteristic will be proposed. Earlier studies have shown that an orthotropic or a transversely isotropic material can possess an anomalous polarization characteristic when the shear stiffness component is larger than one of the normal components, which yields the wave mode transitions to develop between a purely longitudinal and transverse wave modes at the EFC profiles [151-153]. An issue exists on the actual realization of the materials satisfying the unusual material properties (large shear stiffness compared to the normal stiffness). Several studies report on the realization schemes but just give the theoretical possibilities: one can realize the material through a fiber-reinforced composite when adjusting the volume fraction of constituent fibers and their elastic constants, one can through a stratified structure when adjusting the Poisson's ratios, thicknesses, and rigidities of the constituents [151, 153].

Here, materials exhibiting the anomalous polarization characteristic will be realized through using very-simply-configured metamaterials. The designed metamaterials will be shown in this section with their marvelous properties.

6.2.1 Configurations

The schematic of the proposed metamaterial is depicted in Figure 6.1. Slit-shaped void inhomogeneities are designed into an aluminum substrate with the periodic arrangements. In the z -direction, the present configuration in the x - y plane is extended (under the plane strain condition). The zoomed view on the unit cell is also shown in the right side with the design variables: L_x and L_y denote the lattice constants in the x - and y -directions respectively while w and h are the width and height of a constituent slit respectively and s , the separation distance between the adjacent slits. The variables except h are fixed as $L_x = L_y = 6 \text{ mm}$, $w = 0.01 \text{ mm}$, and $s = 1 \text{ mm}$.

It may worth noting on how come the configuration of metamaterial is derived. There are two reasons, one for achieving the high contrast between the normal stiffness components ($C_{22} > C_{11}$ in the present case) and the other for achieving the large value of shear stiffness compared with the value of one of the normal components ($C_{66} > C_{11}$ in the present case), which are the conditions for the anomalous polarization characteristic [153]. For satisfying the condition ($C_{22} > C_{66} > C_{11}$) at the same time, slit-shaped inhomogeneities aligned along the y -direction are adopted, which should significantly disturb a wave flow in the x -direction especially for a longitudinal wave rather than for a transverse wave since a longitudinal wave is known to be sensitive to the length of a inhomogeneity aligned perpendicular to the propagation direction rather than a transverse wave [143, 144]. If the height of a slit h is sufficiently large, the disturbance of an x -directional longitudinal wave by the inhomogeneities will be significant and it should lead to the very low value of C_{11} compared with the values of C_{22} and

C_{66} .

The achievement of the condition $C_{22} > C_{66} > C_{11}$ by using the present metamaterial will be validated in the following section after determining the detail effective properties.

6.2.2 Effective-property characterization by the S-parameter retrieval method

In order to investigate that the anomalous condition for material properties $C_{22} > C_{66} > C_{11}$ is achievable through using the proposed metamaterial with adjusting the slit height h , the effective properties are characterized by employing the S-parameter retrieval method.

Three cases are considered here for $h = 2.5, 3.4,$ and 4.0 mm, and the effective properties for each case are shown in Figures 6.2(a-c) respectively: the first plots in each figure show mass density ρ while the second plots, C_{11} and C_{66} retrieved from the normal incidences of a longitudinal and a transverse waves respectively and the third plots, C_{12} and C_{22} from the oblique incidence of a longitudinal wave specifically at 50° with respect to the x -axis. The effective properties specifically at 30 kHz are as follows:

$$\rho = 2689 \text{ kg/m}^3 \quad \text{and} \quad \mathbf{C} = \begin{bmatrix} 4.84 & 2.39 & 0 \\ 2.39 & 9.12 & 0 \\ 0 & 0 & 2.20 \end{bmatrix} \times 10^{10} \text{ N/m}^2 \quad \text{for } h = 2.5 \text{ mm},$$

$$\rho = 2674 \text{ kg/m}^3 \quad \text{and} \quad \mathbf{C} = \begin{bmatrix} 2.03 & 1.01 & 0 \\ 1.01 & 8.37 & 0 \\ 0 & 0 & 1.89 \end{bmatrix} \times 10^{10} \text{ N/m}^2 \quad \text{for } h = 3.4 \text{ mm},$$

$$\rho = 2654 \text{ kg/m}^3 \quad \text{and} \quad \mathbf{C} = \begin{bmatrix} 1.07 & 0.54 & 0 \\ 0.54 & 8.03 & 0 \\ 0 & 0 & 1.62 \end{bmatrix} \times 10^{10} \text{ N/m}^2 \quad \text{for } h = 4.0 \text{ mm}$$

while the properties for aluminum are

$$\rho = 2700 \text{ kg/m}^3 \quad \text{and} \quad \mathbf{C} = \begin{bmatrix} 10.52 & 5.18 & 0 \\ 5.18 & 10.52 & 0 \\ 0 & 0 & 2.67 \end{bmatrix} \times 10^{10} \text{ N/m}^2.$$

The proposed metamaterials are observed to exhibit the high contrast between the normal stiffness components even for the small value of h . As h increases, the value of C_{11} largely decreases from that of aluminum, and the contrast becomes significant as $C_{22}/C_{11} = 1.88$, 4.12 , and 7.50 for $h = 2.5$, 3.4 , and 4.0 mm respectively while the values of C_{22} and C_{66} do not change that much with respect to the values for aluminum. See the transition for the value of C_{11} compared with the value of C_{66} as h increases. When h is small, C_{11} is larger than C_{66} as observed in general materials. As h decreases below a specific value ($h \approx 3.4$ mm), however, the value of C_{11} significantly decreases while the value of C_{66} is relatively preserved, which yields the targeted anomalous material property as $C_{22} > C_{66} > C_{11}$.

Note that the anomalous property is not achievable through using isotropic materials (even metamaterials). When considering Poisson's ratio ν usually ranges from -1 to 0.5 in isotropic materials and the normal (C_{11}) and shear (C_{66}) stiffness components under the plane strain condition can be expressed in terms of Young's modulus E and Poisson's ratio [48, 49] as

$$C_{11} = \frac{E}{1+\nu} \frac{1-\nu}{1-2\nu} \quad (6.1)$$

and

$$C_{66} = \frac{1}{2} \frac{E}{1+\nu}, \quad (6.2)$$

the ratio between the stiffness components C_{11}/C_{66} should be always above unity, signifying always $C_{11} > C_{66}$ in isotropic materials. Therefore, the material property with $C_{22} > C_{66} > C_{11}$ should be only achievable through using anisotropic materials, and the proposed metamaterial model is shown to effectively satisfy the property when h is sufficiently large.

The anomalous characteristics originating from the material property will be demonstrated in the following sections in respect to wave propagation velocity in Section 6.2.3 and polarization in Section 6.2.4.

6.2.3 Anomalous wave propagation velocities

The first anomalous characteristic originating from the material property with $C_{22} > C_{66} > C_{11}$ is that the propagation (phase as well as group) velocity of a transverse wave exceeds that of a longitudinal wave specifically in the direction where the shear stiffness component is larger than the longitudinal component [153]. Specifically for the present case where $C_{22} > C_{66} > C_{11}$, the characteristic develops along the x -direction. It should be reasonable when considering the wave velocities of a longitudinal (\mathbf{v}^L) and a transverse (\mathbf{v}^T) waves for the x - and y -directions in homogeneous orthotropic materials are expressed as

$$v_x^L = \sqrt{\frac{C_{11}}{\rho}} \quad (6.3)$$

for the x -direction and

$$v_y^L = \sqrt{\frac{C_{22}}{\rho}} \quad (6.4)$$

for the y -direction while

$$v_{x,y}^T = \sqrt{\frac{C_{66}}{\rho}} \quad (6.5)$$

for the x - and y -directions [47, 48]. When $C_{22} > C_{66} > C_{11}$, a transverse wave velocity anomalously exceeds the longitudinal velocity in the x -direction as $v_x^T > v_x^L$ while does not as $v_y^T < v_y^L$ in the y -direction as in usual materials.

In order to validate the characteristic of the proposed metamaterials, dispersion curves (frequency-wavevector ($f - \mathbf{k}$) relation curve) [48, 67] for $h = 2.5, 3.4,$ and 4.0 mm are shown in Figure 6.3. In each plot, the curves for aluminum are also shown with grey lines, among which the steeper curve corresponds to a longitudinal mode regardless of the direction. Note that the curves for every case exhibit the fairly linear slopes in a frequency range below 50 kHz satisfying the long-wavelength limit, so the phase (\mathbf{v}_p) and group (\mathbf{v}_g) velocities are almost identical to each other, which are generally expressed in the following equation forms [47, 48] respectively:

$$\mathbf{v}_p = \frac{2\pi f}{\mathbf{k}} \quad (6.6)$$

and

$$\mathbf{v}_g = \frac{\partial(2\pi f)}{\partial \mathbf{k}} \quad (6.7)$$

For $h = 2.5$ mm, the curve for a longitudinal wave (blue line) is steeper than that for a transverse wave (red line) in both the x - and y -directions, which indicates that the longitudinal velocity is always faster than the transverse velocity as in usual solid materials. The slopes for longitudinal waves in the x - and y -directions are distinctively different with each other while the slopes for transverse waves are almost identical because the wave velocity of a longitudinal mode is determined by the different normal stiffness components for the direction (C_{11} for the x -direction and C_{22} for the y -direction) while the velocity of a transverse mode, by the same shear stiffness component (C_{66} for the x - and y -directions) as explained in Eqs. (6.3-5). Then, see the result for $h = 3.4$ mm. The longitudinal wave velocity in the x -direction significantly decreases and it even becomes similar to the transverse velocity. For the y -direction, on the other hand, the velocities of both the two wave modes do not change that much with respect to those for $h = 2.5$ mm. In the case of $h = 4.0$ mm, the longitudinal velocity further decreases even below the transverse velocity in the x -direction while it still exhibits the large value compared with the transverse one in the y -direction. The anomalous characteristic on wave velocity is consistently observed over an entire frequency range in the long-wavelength.

The present dispersion curves validate the velocity of a transverse wave can exceed that of a longitudinal wave velocities specifically in the direction where the shear stiffness component exceeds the value of the normal component, and the proposed metamaterial can simply achieve the characteristic with the large value of h .

6.2.4 Anomalous polarization characteristics

The other anomalous characteristic originating from the material property with $C_{22} > C_{66} > C_{11}$ is that wave mode transitions develop in every EFC profile [153]. Figure 6.4 shows the angle of deviation ($\Delta\theta$) between the directions of the wavevector and the polarization vector at a specific wavevector orientation (θ_k), which can be defined as

$$\Delta\theta = |\theta_k - \theta_p| \quad (6.8)$$

where θ_p represents the orientation of the polarization vector at θ_k . Three cases are also considered for $h = 2.5, 3.4,$ and 4.0 mm, and $\Delta\theta$ for the waves corresponding to the outer and inner EFC profiles are indicated by red and blue lines respectively. When $\Delta\theta = 0^\circ$ or 180° , the wave should be purely longitudinal and when $\Delta\theta = 90^\circ$, purely transverse. Mode transition occurs at $\Delta\theta = 45^\circ$ or 135° , which are illustrated by black dashed line in each plot.

See the results for $h = 2.5$ and 3.4 mm. The deviation angles $\Delta\theta$ for the inner and outer EFCs are observed to span the ranges of $0^\circ \leq \Delta\theta \leq 13^\circ$ and $90^\circ \leq \Delta\theta \leq 103^\circ$ respectively in the case of $h = 2.5$ mm while $0^\circ \leq \Delta\theta \leq 37^\circ$ and $90^\circ \leq \Delta\theta \leq 127^\circ$ respectively in the case of $h = 3.4$ mm. For the x - and y -directions, the inner and outer contours are found to represent purely longitudinal and transverse wave modes respectively as in general orthotropic materials. When considering $\Delta\theta$ for the inner and outer contours do not exceed the degrees of 45° and 135° respectively in the both cases, the wave modes corresponding to the contours can be referred to as quasilongitudinal and quasitransverse modes,

respectively. The cases follow the usual polarization characteristics observed in general anisotropic materials.

For $h = 4.0$ mm, on the other hand, an anomalous polarization characteristic is observed not only at the inner but also at the outer contours: the deviation angles at $\theta_k = 0^\circ$ and 90° are $\Delta\theta = 90^\circ$ and 0° respectively for the inner contour while $\Delta\theta = 180^\circ$ and 90° respectively for the outer contour. It means that the inner contour represents a purely transverse mode at $\theta_k = 0^\circ$ but a purely longitudinal mode at $\theta_k = 90^\circ$ while the outer contour, the opposite modes at each degree of θ_k . In the range of $0^\circ \leq \theta_k \leq 90^\circ$, $\Delta\theta$ for the inner and outer contours are observed to gradually decrease from 90° to 0° and from 180° to 90° respectively as θ_k increases, which signifies the mode transitions develop at each EFC profile.

In Figure 6.5, the EFC for the case of $h = 4.0$ mm is shown at 30 kHz with black lines and the directions of the polarization vectors at specific wavevectors are also illustrated. The inner (outer) contour is observed to represent a purely transverse (longitudinal) wave mode when $k_y = 0$ but a pure longitudinal (transverse) mode when $k_x = 0$ as previously demonstrated. Remind that the wavenumber k_x for the inner contour with $k_y = 0$ matches k_y for the outer contour with $k_x = 0$ since the corresponding wave modes are a purely transverse mode, which is totally governed by the shear stiffness C_{66} regardless of the propagation direction.

6.3 Design of Wave Mode Converters

By utilizing the anomalous polarization characteristic achievable with the proposed metamaterial, wave mode converters dealing with the transition from a longitudinal to a transverse modes will be designed in this section. Compared to the conventional converting systems using the critical angle scheme [60, 61], the proposed system has several distinct strengths as follows:

Strength 1: the proposed system is capable of emitting a transverse wave as the output at the normal to the system surface for a longitudinal wave input also normal to the system surface,

Strength 2: owing to Strength 1, the proposed system works regardless of the material properties of a surrounding target material while yielding the consistent output,

Strength 3: the proposed system shows the high converting ratio since the high contrast between the material properties of the system and a target material is not needed at all.

A novel methodology for achieving mode converters will be introduced first, and its robust performance will be validated in the rest of the section.

6.3.1 Methodology for wave mode converters

The proposed methodology for achieving mode converting systems is illustrated in Figure 6.6. See Figure 6.6(a) for the schematic configuration of the proposed mode converter. The converter is built in a triangular formation consisting of an array of the metamaterials presented in Figure 6.1 with $h = 4.0$ mm, which exhibit the anomalous polarization characteristic. The left boundary of the converter, aligned along the y -direction, is for a longitudinal wave input while the upper boundary,

aligned along the x -direction, is for a transverse wave output. The both boundaries are set to meet a homogeneous aluminum substance here for a fundamental study, and waves flow toward and outward the converter in the substance. The other boundary with a specific angle of slope, θ_s exists for converting a wave mode by the wave refraction scheme [47, 50] (details shall be demonstrated in Figure 6.6(b)), and the free-end boundary condition is imposed on the boundary. Note that the inclined boundary is not actually linear when the square-shaped metamaterials are used, but it can be considered to be approximately linear in the long-wavelength limit. The indices k_1 and k_4 illustrated in the figure represent the wavenumbers in the aluminum substance bordering the converter for the x -directional longitudinal wave and the y -directional transverse wave respectively, while k_2 and k_3 , the wavenumbers in the converter for the two wave components respectively.

Before demonstrating the overall methodology, it may worth remarking on the wave refraction scheme used at the inclined free-end boundary in detail. Figure 6.6(b) illustrates the direction of the refracted wave at the inclined boundary with the angle of slope, θ_s for the incidence of a longitudinal wave propagating in the x -direction with the wavenumber k_2 . It is shown in the geometric (left pictures) and wavevector (right) spaces. See the top pictures first. When the longitudinal wave with k_2 just meets the boundary, the wave should be refracted at the angle of θ_R with the magnitude of wavevector, k_R for maintaining the tangential momentum of the incident wave, following the Snell's law [47, 48] as

$$k_2 \cos \theta_s = k_R \cos \theta_R \quad (6.9)$$

where θ_R and k_R can be estimated in the \mathbf{k} -space by the simple constructions of lines aligned along the normal and tangential directions to the boundary as illustrated in the right picture.

For a specific angle of slope, the orientation of the refracted wave can just correspond to the y -direction as illustrated in the bottom pictures as

$$\theta_R = 90^\circ - \theta_S. \quad (6.10)$$

Emphasize that the refracted wave for the case possesses a purely-transverse polarization even though the corresponding wavevector lies in the same branch of EFC with that of the incident longitudinal wave (k_2) owing to the anomalous polarization characteristic of the metamaterial as demonstrated in Figure 6.4(c). So, $k_R = k_3$ in the present case where k_3 denotes the wavenumber of the y -directional transverse wave in the converter. By using the refraction scheme, the mode transition from a purely longitudinal to purely transverse waves can be achieved at the slope without any energy loss. For the design of a mode converter, θ_S is selected to satisfy Eq. (6.10).

Then, the overall methodology will be demonstrated with using the EFCs for the constituent metamaterials in the mode converter (marked by thick lines) and the bordering aluminum substance (thin lines) in Figure 6.6(c). The inner and outer EFC profiles for aluminum represent longitudinal and transverse modes, respectively. In the plot, the wavenumbers k_1 to k_4 corresponding to the wave components illustrated in Figure 6.6(a) are also marked by circular dots.

For the normal incidence of a longitudinal wave with k_1 at the left boundary of the converter, only the longitudinal wave carrying k_2 should be transmitted into

the converter because the wave components with k_1 and k_2 share the same polarization characteristic. When the transmitted longitudinal wave just meets the inclined boundary, the purely transverse wave with k_3 should be refracted and it propagates just along the y -direction as previously demonstrated. Lastly, at the upper boundary of the converter, the transverse wave carrying k_4 should be transmitted. The proposed converter ultimately emits a transverse wave (k_4) only especially at the normal to the surface for a longitudinal wave input (k_1).

6.3.2 Validation of the performance by FEM simulations

In this section, the performance of the proposed mode converter will be validated by using the FEM simulations conducted in COMSOL Multiphysics 3.5a. See Figure 6.7 where the response of the converter is shown for the incidence of a longitudinal wave at 100 kHz. Although the detail configuration of the converter is not shown here, the converter is built in a triangular formation just as previously demonstrated with $\theta_s = 51^\circ$ while $D_x = 2.34\lambda_{al}$ and $D_y = 2.88\lambda_{al}$ where λ_{al} represents the wavelength of a longitudinal wave at 100 kHz in the aluminum substance surrounding the converter. An array of metamaterials presented in Figure 6.1 with $h = 4.0$ mm is set to fill the area of the converter after scaling down the size from $L_x = L_y = 6$ mm to 1.8 mm in order to broadening the working frequency range up to about 160 kHz. The configuration of the converter just near the slope is illustrated beside Figure 6.7(b).

Figure 6.7(a) shows the x -directional velocity field for the incident longitudinal wave ($v_{x,inc}$) exhibiting a sine distribution in the y -direction with the full width at

half maximum (FWHM), $w_s = 0.67D_y$. The formation of the converter is marked with black dashed line in the figure. In Figure 6.7(b), the x -directional velocity field of the scattering waves ($v_{x, \text{scat}}$) developed at the left boundary of the converter is presented while the x - and y -directional velocity fields for the total field ($v_{\text{tot}} = v_{\text{inc}} + v_{\text{scat}}$) are shown in Figures 6.7(c, d), respectively. The color scale used in the plots is shown beside Figure 6.7(d) (several void regions inside the converter exceed the present range).

The observations from the results are listed as follows:

- (1) when seeing the transmitted wave from the converter (propagating in the y -direction) possesses only the x -directional velocity components, the converter emits a purely transverse wave only along the y -direction (see also the wavelength of a transmitted wave, which is about a half of that for the incident longitudinal wave),
- (2) when seeing the magnitude of the reflected wave at the left surface of the converter is significantly small compared to the magnitude of the transmitted wave at the upper surface (Figure 6.7(b)), the conversion ratio should be fairly high: the transmittance of the y -directional-propagating transverse wave ($P_y^{\text{T, transv}} / P_x^{\text{I, longi}}$) is observed to be about 0.66 while the reflectance of the x -directional-propagating longitudinal wave ($P_x^{\text{R, longi}} / P_x^{\text{I, longi}}$) is 0.29 where

$$P_x^{\text{I, longi}} = \left| \text{real} \left(\sigma_{xx}^{\text{I}} \times \text{conj} \left(v_x^{\text{I}} \right) \right) \right|, \quad (6.11a)$$

$$P_y^{\text{T, transv}} = \left| \text{real} \left(\sigma_{xy}^{\text{T}} \times \text{conj} \left(v_x^{\text{T}} \right) \right) \right|, \quad (6.11b)$$

$$P_x^{\text{R, longi}} = \left| \text{real} \left(\sigma_{xx}^{\text{R}} \times \text{conj} \left(v_x^{\text{R}} \right) \right) \right| \quad (6.11c)$$

and $\sigma_{xx}^I (v_x^I)$, $\sigma_{xx}^R (v_x^R)$ indicate the x -directional normal stresses (velocities) of the incident and reflected waves respectively near the left surface of the converter and $\sigma_{xy}^T (v_x^T)$, the shear stress (x -directional velocity) of the transmitted wave near the upper surface.

- (3) there exists energy leakage below 0.05 ($1 - P_x^{R, \text{longi}} / P_x^{I, \text{longi}} - P_y^{T, \text{transv}} / P_x^{I, \text{longi}}$) mainly due to a leaky wave through the right-upper corner of the converter as shown in Figure 6.7(d); the wave may originate from the additional refraction of a quasilongitudinal wave mode at the slope, which shall be demonstrated later in detail,
- (4) the transmitted purely transverse wave from the upper surface of the converter exhibits the slightly-tilted wavefront with respect to the x -axis, which means that the propagation direction of the wave does not actually coincide with the y -direction exactly; the main reason should be the diffraction of the wave transmitted into the converter at the left surface due to a finite incident beam width, which also shall be demonstrated later.

Even though the present mode converter exhibits the energy leakage at the corner as mentioned in Observation 3, the leakage is negligibly small compared to the transmitted energy and the converter successfully works with the high conversion ratio. This remark also can be supported by the results in Figure 6.8, which shows the same simulation results with them in Figure 6.7 but indicating them by the strain energy density fields. The total strain energy density field, $W_{\text{tot}} = W_{xx} + 2W_{xy} + W_{yy}$ is presented in Figure 6.8(a) while each component, in Figures 6.8(b-d) respectively, which are defined as

$$W_{xx} = \sigma_{xx} \varepsilon_{xx}, \quad (6.12a)$$

$$W_{xy} = 2\sigma_{xy} \varepsilon_{xy}, \quad (6.12b)$$

$$W_{yy} = \sigma_{yy} \varepsilon_{yy}, \quad (6.12c)$$

where σ and ε denote stress and strain, respectively. Only the wave fields in the aluminum substance bordering the converter are shown here.

The results distinctively signify that the reflected wave at the left surface of the converter is a x -directional-propagating longitudinal wave and the transmitted wave from the upper surface, a purely transverse wave. The magnitudes of other wave modes are observed to be negligible and the leaky wave at the corner also. Note that each wave component exhibits the halves of the actual wavelengths in the present strain energy density fields since they have the harmonic terms as $\exp(j2\mathbf{k} \cdot \mathbf{r})$ here when $\exp(j\mathbf{k} \cdot \mathbf{r})$ in the velocity or stress field (\mathbf{k} : wavevector, \mathbf{r} : directional vector; $j = \sqrt{-1}$).

The performance of the converter is also examined through using the effective medium model after adopting the effective properties of the metamaterials as

$$\rho = 2654 \text{ kg/m}^3 \quad \text{and} \quad \mathbf{C} = \begin{bmatrix} 1.07 & 0.54 & 0 \\ 0.54 & 8.03 & 0 \\ 0 & 0 & 1.62 \end{bmatrix} \times 10^{10} \text{ N/m}^2.$$

Two cases are considered here: one with the discretized slope at the inclined surface of the converter (just as the slope in the actual detailed model) and the other with the linearized slope. The results, specifically the x -directional velocity fields, are shown in Figures 6.9-10 respectively and they are compared with the result from the detailed model. The velocity fields in the converter region are also presented below each plot.

The result from the effective medium model with the discretized slope (Figure 6.9(b)) is perfectly identical to that from the detailed model. It signifies that the characterization of the effective properties for the metamaterial is successfully implemented and the converter works as the homogeneous structure possessing the anomalous polarization characteristic. The result from the effective medium model with the linearized slope (Figure 6.10(b)) also corresponds to those results, meaning that the discretized slope indeed performs a role as a linear slope and it should refract an incoming wave while converting the wave mode just as intended.

6.3.3 Robust performance for various environmental conditions

Here, the performance of the proposed mode converter will be investigated for various environmental conditions: for incident longitudinal wave sources exhibiting the varying FWHMs (w_s) and for varying working frequencies (f).

The performances along the FWHM of an incident source are presented in Figure 6.11 where four cases are examined at 100 kHz with $w_s = 0.67D_y$, $0.56D_y$, $0.44D_y$, and $0.33D_y$ (D_y : the height of the converter; $D_y = 2.88\lambda_{al}$). The results are shown by the x -directional velocity fields. As w_s decreases, not only the transmitted transverse wave from the upper surface of the converter but also the waves inside the converter exhibit the somewhat tilted wavefronts as well as the tilted propagation directions with respect to the directional axes. It should mainly originate from the diffraction of the wave transmitted into the converter at the left surface before encountering the slope, whose effect becomes significant as w_s decreases. Due to the diffraction, the transmitted wave from the left surface carries

the wavevector components near the wavevector $k_2\hat{x}$ not just the $k_2\hat{x}$ component as illustrated in Figure 6.6(c), which leads the refracted wave at the slope to carry the wavevector components also near the wavevector $k_3\hat{y}$. When considering the wavevector components with the positive k_x near $k_3\hat{y}$ should be dominantly refracted at the slope compared to them with the negative k_x (since a significant portion of the wavevector components with the negative k_y near $k_2\hat{x}$ should be refracted as quasilongitudinal wave modes, whose EFC branch is located at the inner side), the refracted wave should have the refraction angle θ_R smaller than the targeted degree.

Nevertheless, the present converter robustly works regardless of the beam width of an incident longitudinal wave. It can be also supported by the results in Figure 6.12, which shows the energy density fields specifically for the case of $w_s = 0.33D_y$. Despite the energy leakage at the right-upper corner is observed significant compared to that in the case of $w_s = 0.67D_y$ in Figure 6.8, the converter distinctively emits a purely transverse wave at the upper surface as intended. The output power ratios ($P_y^{\text{T, transv}} / P_x^{\text{l, longi}}$) are also calculated for every case shown in Figure 6.11, and they are observed as 0.66 ($w_s = 0.67D_y$), 0.62 ($0.56D_y$), 0.58 ($0.44D_y$), and 0.51 ($0.33D_y$). The decrease in the output power ratios as w_s decreases should originate from the additional refraction of a quasilongitudinal wave at the slope as previously mentioned, leading to the large energy leakage at the corner.

Then, the designed converter is examined for the varying working frequency in

Figure 6.13 for the fixed $w_s = 0.67D_y$. The converter surprisingly exhibits the consistent performance even at $f = 33$ kHz, where the dimension of the converter is even smaller than the wavelength in the surrounding aluminum substance. It is owing to the proposed metamaterial, which exhibits the anomalous polarization characteristic in a very broad frequency range especially with no lower bound. The strain energy density fields specifically at $f = 50$ kHz, shown in Figure 6.14, also validate the working capability of the converter in a broad frequency range.

It may worth remarking on the distorted wave fields appearing near the upper surface of the converter as shown in Figure 6.14. There should be two main reasons: one is the widely-ranged near-field region and the other is the significant leaky waves at the corner. The energy leakage during the refraction at the slope is observed to increase as the working frequency decreases. However, the amount is still fairly small compared to the transmittance of a transverse wave from the converter.

The robustness of the converter on the angle of the inclined slope is also presented in Figure 6.15. The x - and y -directional velocity fields for the angles $\theta_s^* = \theta_s + 5^\circ$ and $\theta_s^* = \theta_s - 5^\circ$ are examined in Figures 6.15(a, b) respectively where the original angle of the slope θ_s is illustrated with grey dashed lines. The converter is still observed to emit a transverse wave as the output regardless of θ_s^* . Even though a leaky wave is observed significant at the corner in the case of $\theta_s^* = \theta_s + 5^\circ$ (because of the additional refraction of a quasilongitudinal wave mode along the slope direction), the transmittance of the transverse wave from the upper surface are still large. The present results implies that the direction of a transmitted

transverse wave can be adjusted by delicately determining the slope angle θ_s , which can be utilized for the applications to a guided structure.

6.4 Summary

The simply-configured metamaterial exhibiting anomalous characteristics is proposed in this section. It possesses the larger value of the shear stiffness component than the value of one of the normal components, which leads to two distinct characteristics: one is that the wave propagation velocity of a transverse wave exceeds that of a longitudinal wave in a specific direction and the other is that the polarizations at each EFC show the dramatic transitions from a purely longitudinal (transverse) mode for one direction to a purely transverse (longitudinal) for the orthogonal direction.

By employing the anomalous characteristics of the metamaterial, a wave mode converter is designed. Here, the refraction scheme is used for implementing the wave mode conversion with the high efficiency. The proposed converter is shown to robustly work not only for the varying beam width of an incident longitudinal wave but also for the varying working frequency while consistently emitting a purely transverse wave as the output at the normal direction to the converter surface. Because the converter does not utilize the critical angle scheme for the conversion, it can also work for the conversion from a transverse to a longitudinal wave modes. The proposed converter is expected to be utilized for various applications especially in the NDE area.

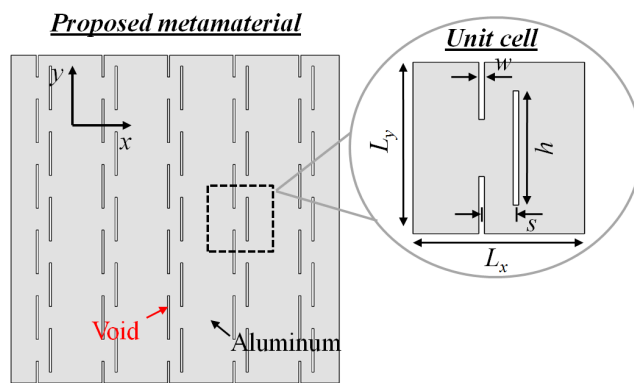
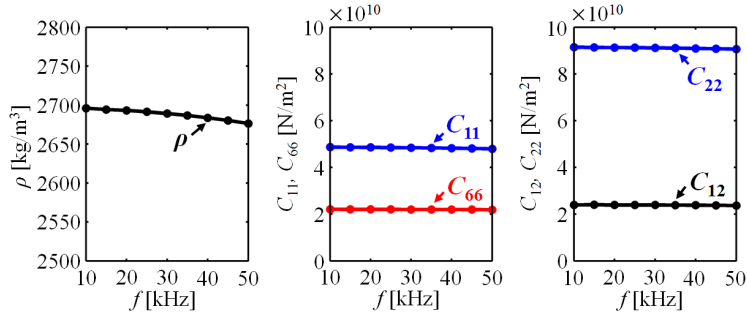
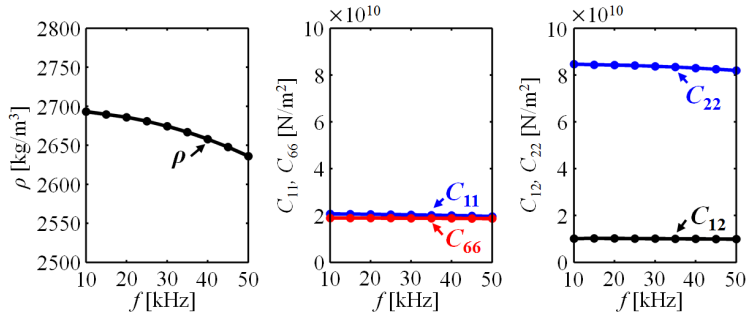


Figure 6.1 The schematic configuration of the proposed metamaterial

(a) Effective properties for $h=2.5$ mm



(b) Effective properties for $h=3.4$ mm



(c) Effective properties for $h=4.0$ mm

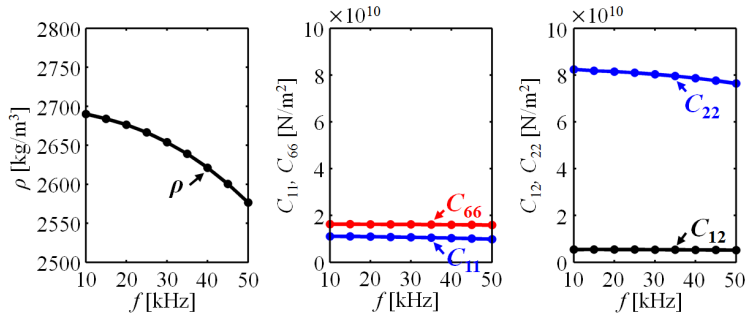
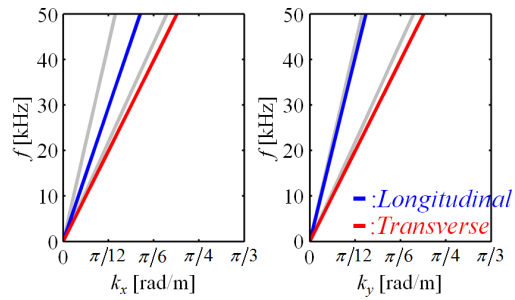
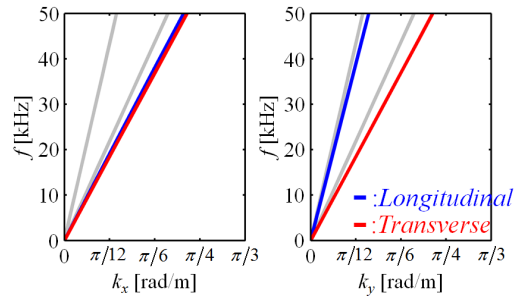


Figure 6.2 The effective properties of the proposed metamaterials for the varying design parameter, h

(a) Dispersion curve for $h=2.5$ mm



(b) Dispersion curve for $h=3.4$ mm



(c) Dispersion curve for $h=4.0$ mm

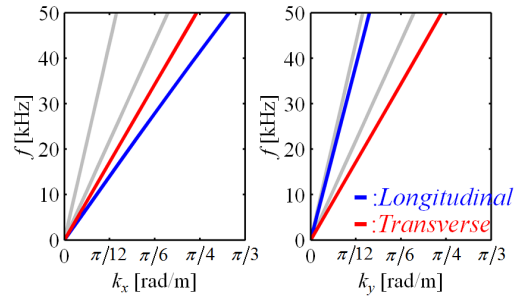


Figure 6.3 The dispersion curves for the proposed metamaterials with the varying design parameter, h

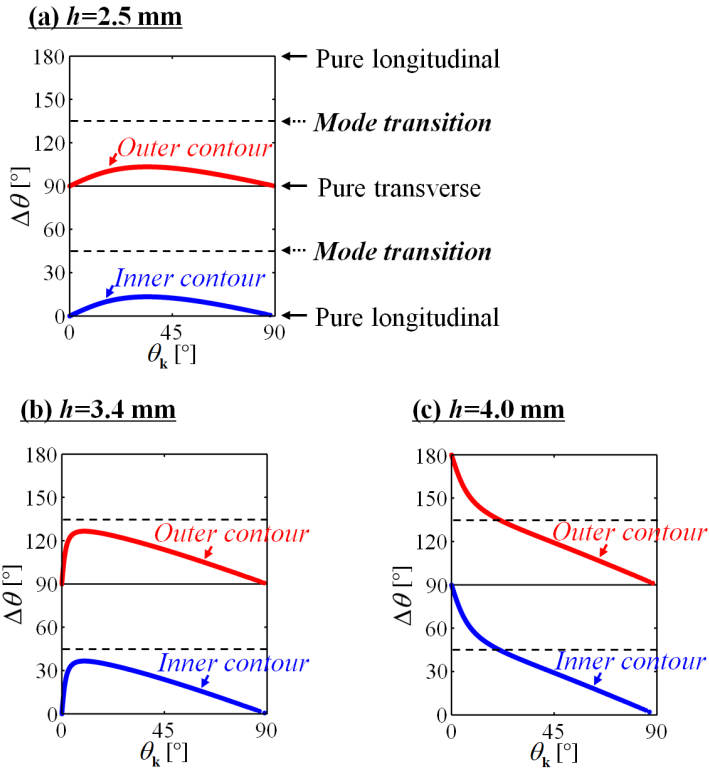


Figure 6.4 The deviation angles for the proposed metamaterials with the varying design parameter, h

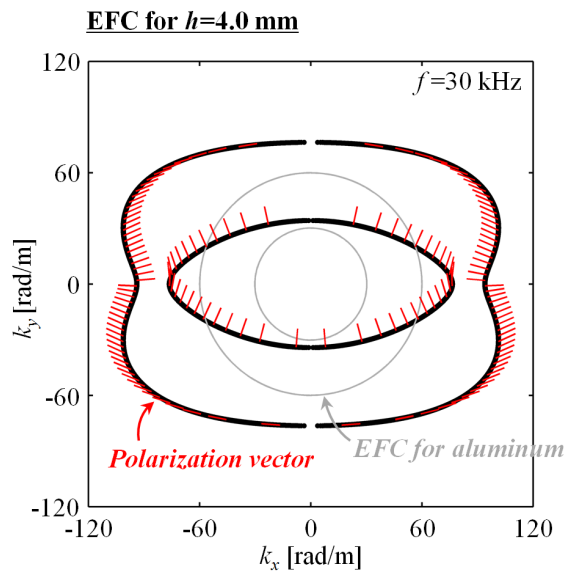


Figure 6.5 The EFC for the proposed metamaterial with $h = 4.0$ mm at 30 kHz

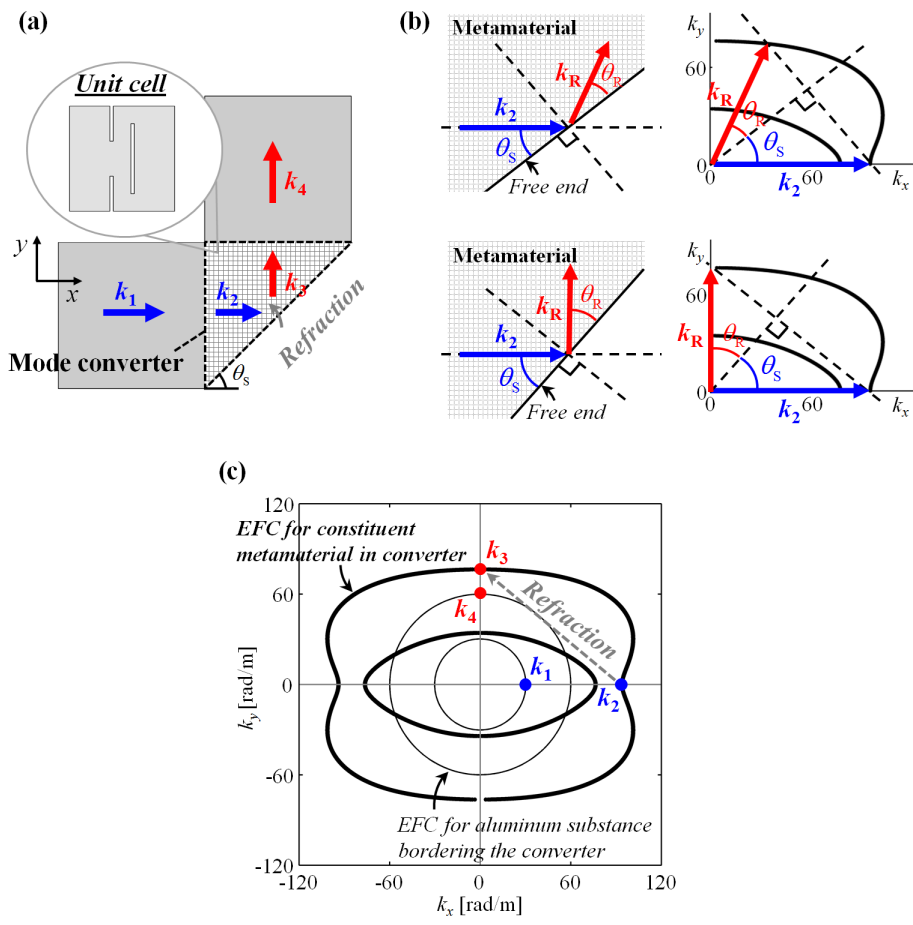


Figure 6.6 (a) The schematic configuration of the proposed mode converter and the setting considered in this study, (b) the schematic pictures for the demonstration on the refraction scheme, and (c) the description of the proposed methodology for mode converters by employing the EFCs

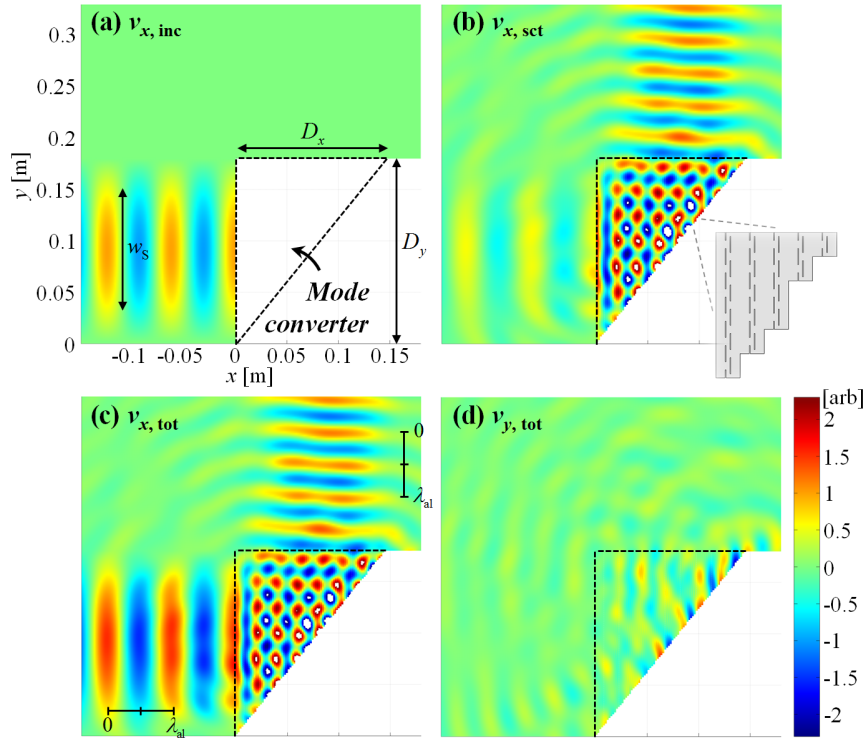


Figure 6.7 The FEM simulation results for the (a) incident, (b) scattered, and (c-d) total wave fields, indicated by the (a-c) x - and (d) y -directional velocities

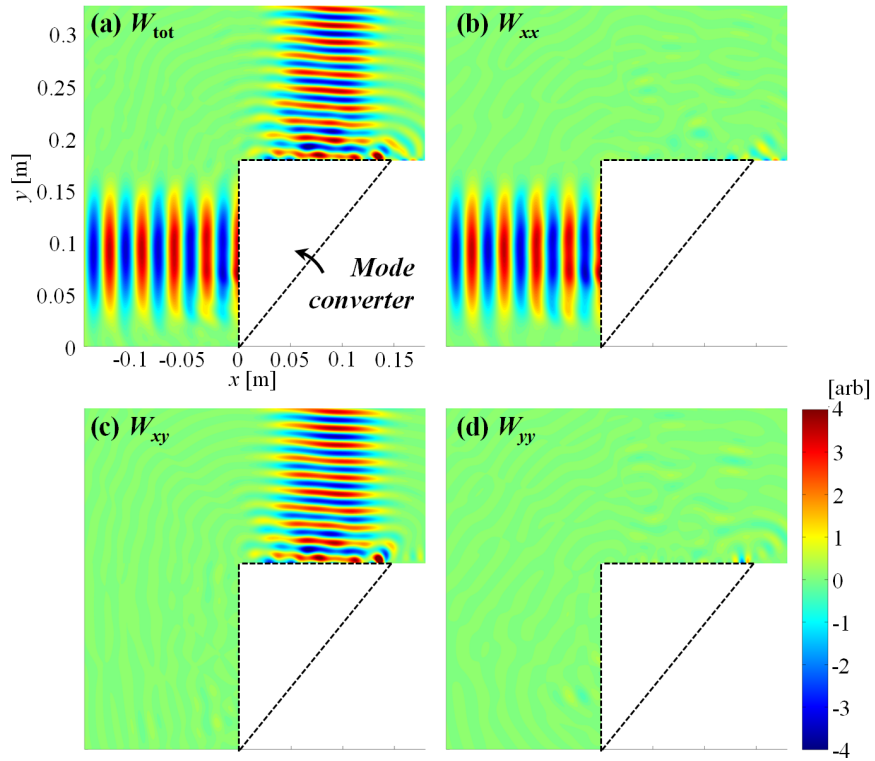


Figure 6.8 The FEM simulation results for the strain energy density fields, indicated by (a) W_{tot} , (b) W_{xx} , (c) W_{xy} , and (d) W_{yy} .

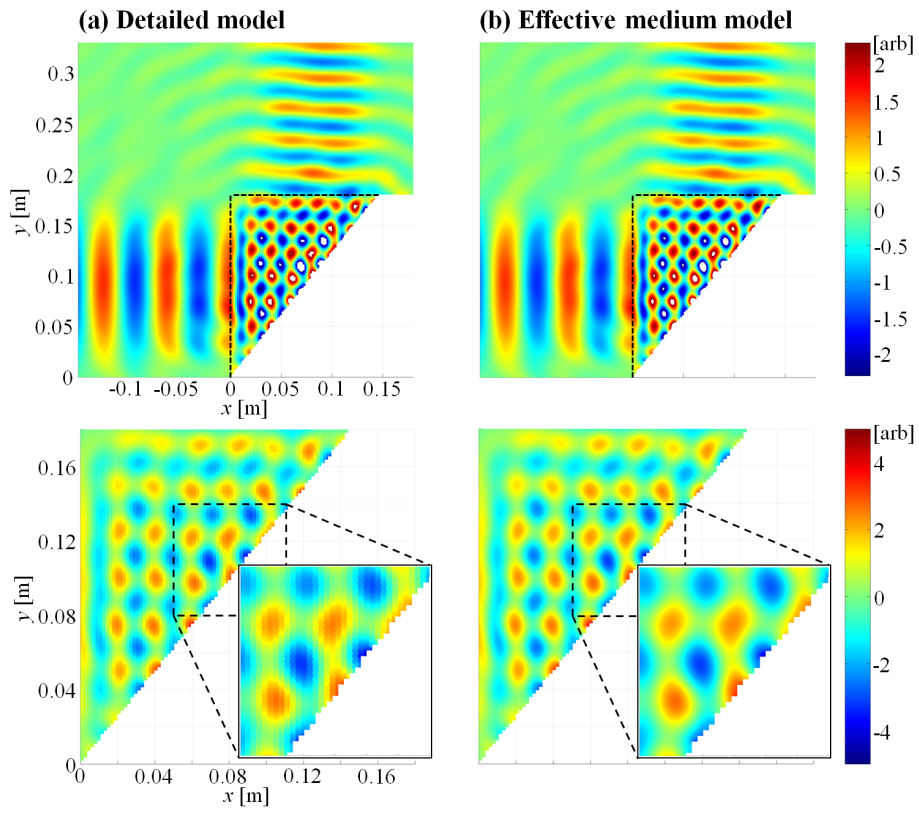


Figure 6.9 The FEM simulation results for the x -directional velocity fields, analyzed by (a) the detailed and (b) the effective medium models with the zoomed views on the converter regions

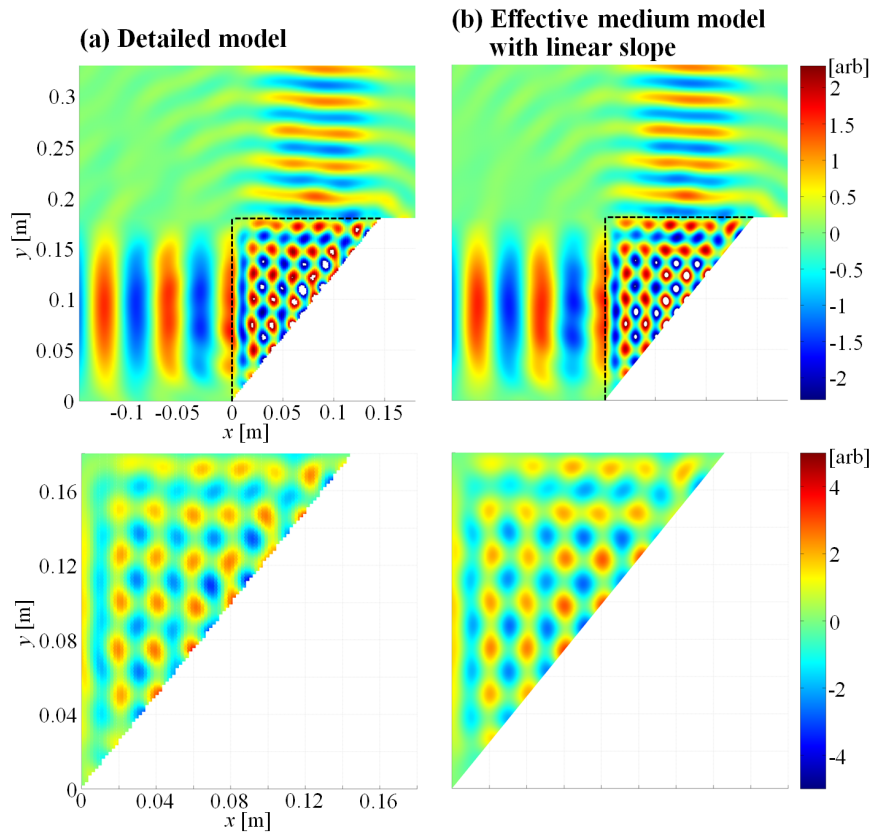


Figure 6.10 The FEM simulation results for the x -directional velocity fields, analyzed by (a) the detailed model and (b) the effective medium model having the linear slope with the zoomed views on the converter regions

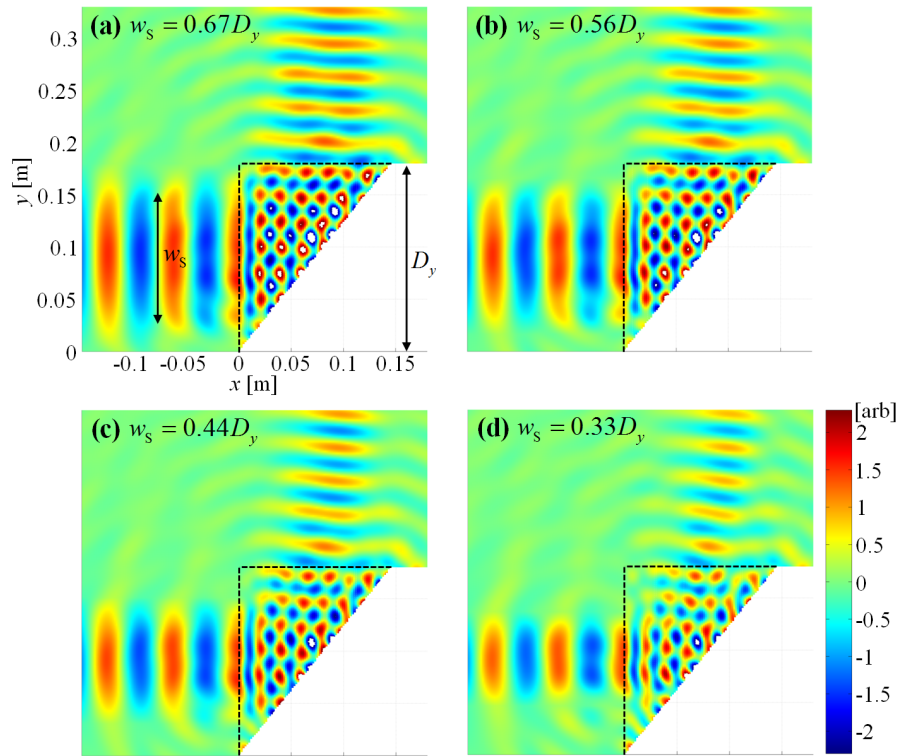


Figure 6.11 The FEM simulation results for the varying value of w_s , indicated by the x -directional velocity fields

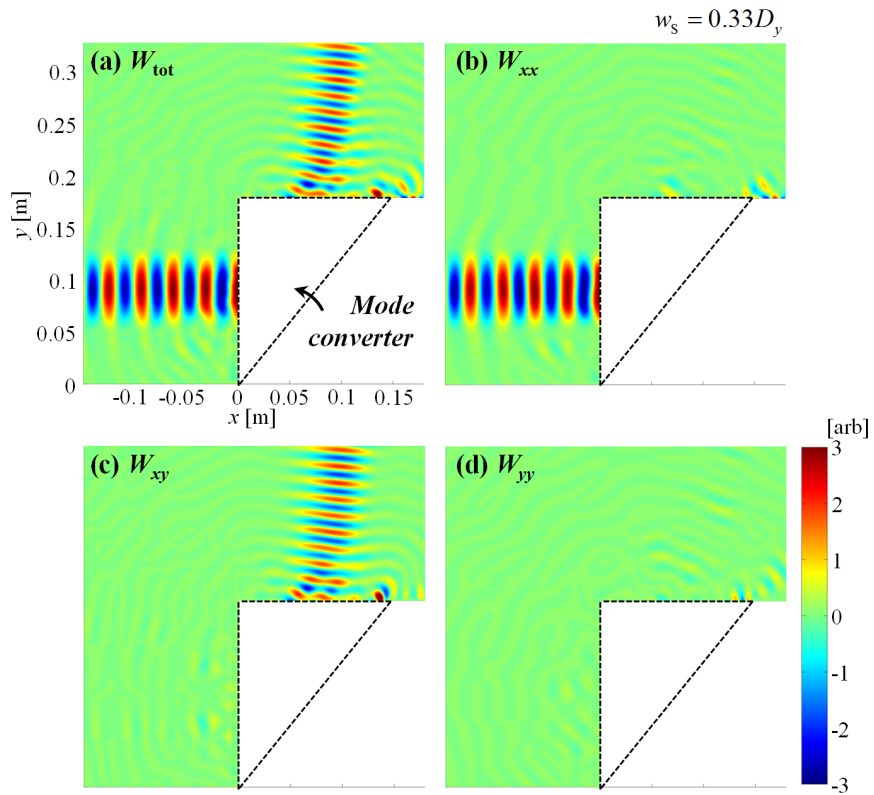


Figure 6.12 The FEM simulation results for $w_s = 0.33D_y$ indicated by the strain energy density fields

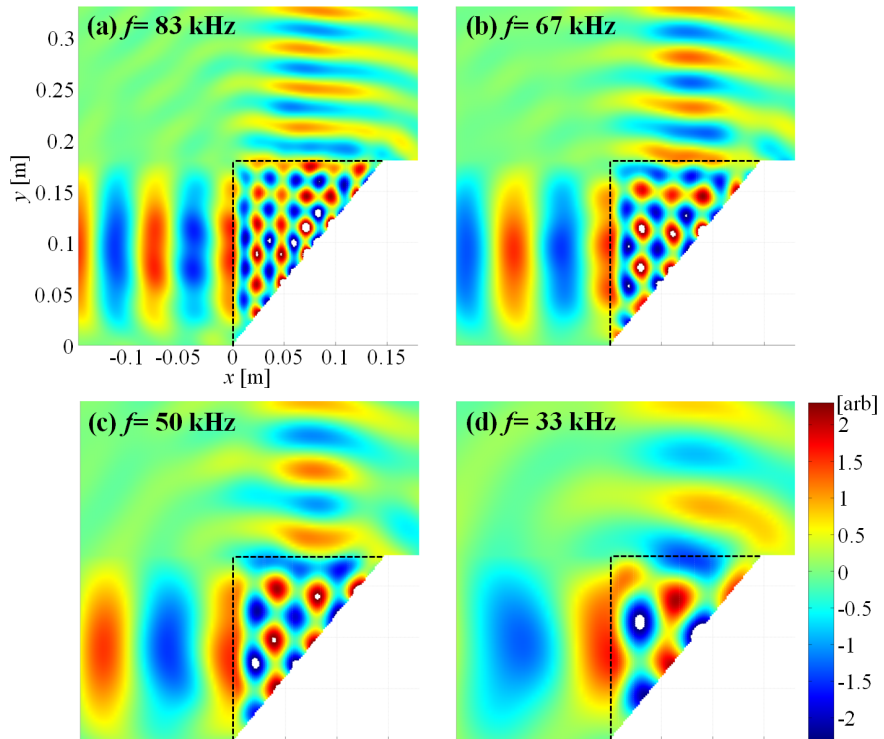


Figure 6.13 The FEM simulation results for the varying frequency, indicated by the x -directional velocity fields

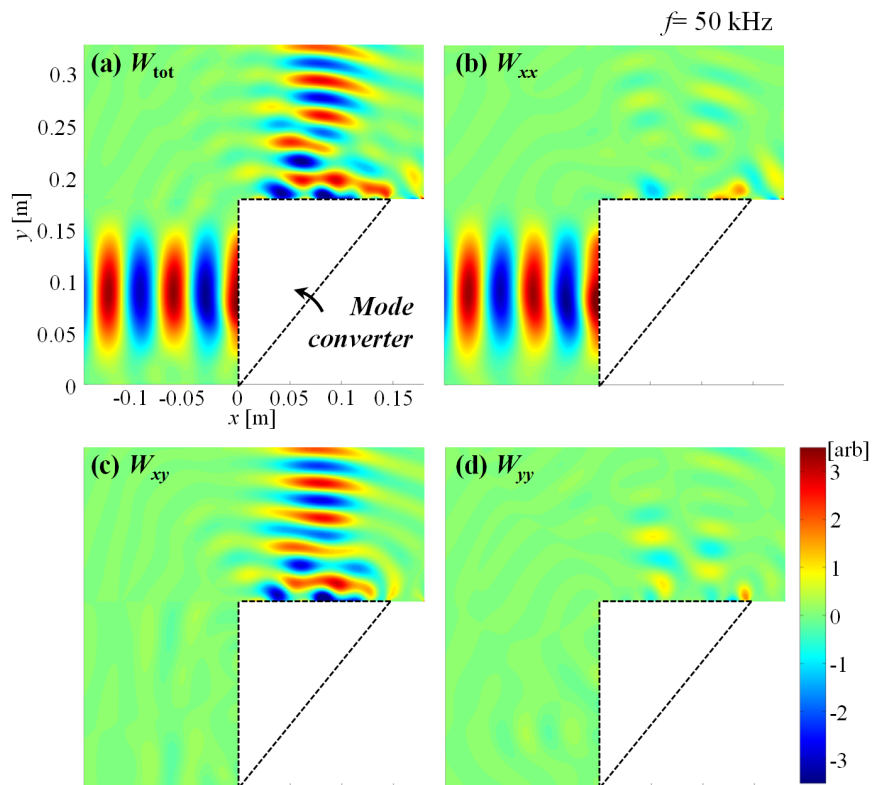


Figure 6.14 The FEM simulation results for $f = 50 \text{ kHz}$, indicated by the strain energy density fields

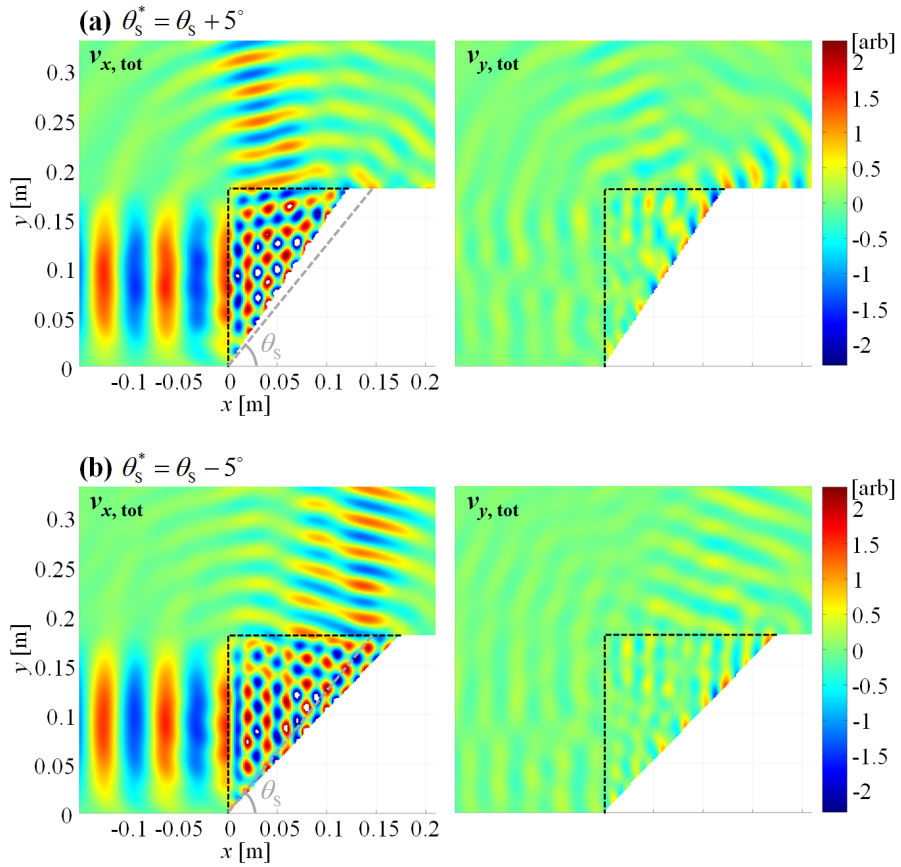


Figure 6.15 The FEM simulation results for (a) $\theta_s^* = \theta_s + 5^\circ$ and (b) $\theta_s^* = \theta_s - 5^\circ$, indicated by the x - (left plots) and y - (right) velocity fields

CHAPTER 7.

Conclusions

The thesis presented the improved version of the S-parameter retrieval method applicable for characterizing anisotropic elastic metamaterials. Furthermore, by employing the developed retrieval method, novel elastic metamaterials are successfully designed and utilized for engineering applications. The detail contributions of this work can be summarized as follows:

First, the developed S-parameter retrieval method can thoroughly determine the effective material parameters of elastic metamaterials. The characterizations are implemented in the two steps: one is to determine the effective properties involved in the S-parameters for normal incidences and the other is to determine the rest of properties involved in the S-parameters for oblique incidences. Through the two-step approach, the whole constitutive properties including the diagonal as well as the non-diagonal components in stiffness can be accurately extracted even for the metamaterials possessing the principal axes not aligned with the coordinate axes. The proposed retrieval method is expected to give great contributions to the characterizations of elastic metamaterials and the analyses on their performances.

Secondly, the proposed elastic magnifying hyperlens, constructed by extremely anisotropic metamaterials, can achieve significantly high resolution images. The elastic hyperlens is shown to overcome the diffraction limit, which is well-known as the fundamental limit for a usual imaging device, owing to the extreme

anisotropy achieved by the metal-air multilayer metamaterial. The performance is validated through the experiments conducted at 100 kHz, an ultrasonic frequency, and the experiments confirm that the hyperlens can image a sub-diffraction-limited object without any help of a resonance scheme while working in a quite broad frequency range. The proposed hyperlens is expected to be utilized for subwavelength imaging in medical ultrasound or non-destructive evaluation.

Thirdly, the proposed mechanical bandpass filters, constructed by impedance-only-varying metamaterials, can achieve quasi-ideal filtering performances. The novel methodology using impedance-varying phononic bandgap structures for bandpass filters are successfully realized through using impedance-only-varying metamaterials. The designed filters are shown to achieve a unity passband with the virtually flat top, broad surrounding stopbands, and steep bandedges simultaneously. They exhibit excellent performances compared with the conventional bandpass filters also with the compact dimensions. The proposed bandpass filters and the design methodology are expected to be utilized in the medical imaging and non-destructive evaluation areas.

Finally, the proposed wave mode converters, constructed by metamaterials exhibiting anomalous polarization characteristic, can achieve the high conversion efficiencies. The novel methodology using a refraction scheme for mode converters is successfully realized through using the metamaterials exhibiting dramatic wave mode transitions at each branch of EFCs. The developed converters are shown to robustly work for various environmental conditions while consistently emitting a purely transverse wave as the output along the normal direction to the surface for a

longitudinal wave input. Since the converter does not utilize the well-known critical-angle scheme, they can work with the high efficiencies. The proposed converters are expected to be utilized specifically in the non-destructive evaluation area.

REFERENCES

- [1] J. B. Pendry, A. J. Holden, D. J. Robbins, and W. J. Stewart, *IEEE Transactions on Microwave Theory and Techniques* 47, 2075 (1999).
- [2] R. A. Shelby, D. R. Smith, and S. Schultz, *Science* 292, 77 (2001).
- [3] S. Enoch, G. Tayeb, P. Sabouroux, N. Guérin, and P. Vincent, *Physical Review Letters* 89, 213902 (2002).
- [4] A. Grbic and G. V. Eleftheriades, *Journal of Applied Physics* 92, 5930 (2002).
- [5] M. A. Antoniades and G. V. Eleftheriades, *IEEE Antennas and Wireless Propagation Letters* 2, 103 (2003).
- [6] B. T. Schwartz and R. Piestun, *Journal of the Optical Society of America B* 20, 2448 (2003).
- [7] A. B. Movchan and S. Guenneau, *Physical Review B* 70, 125116 (2004).
- [8] G. V. Viktor, *Soviet Physics Uspekhi* 10, 509 (1968).
- [9] D. R. Smith, W. J. Padilla, D. C. Vier, S. C. Nemat-Nasser, and S. Schultz, *Physical Review Letters* 84, 4184 (2000).
- [10] J. B. Pendry, *Physical Review Letters* 85, 3966 (2000).
- [11] R. W. Ziolkowski and E. Heyman, *Physical Review E* 64, 056625 (2001).
- [12] G. V. Eleftheriades, A. K. Iyer, and P. C. Kremer, *IEEE Transactions on Microwave Theory and Techniques* 50, 2702 (2002).
- [13] R. W. Ziolkowski, *Physical Review E* 70, 046608 (2004).
- [14] J. Shin, J.-T. Shen, and S. Fan, *Physical Review Letters* 102, 093903 (2009).
- [15] M. Choi, S. H. Lee, Y. Kim, S. B. Kang, J. Shin, M. H. Kwak, K.-Y. Kang,

- Y.-H. Lee, N. Park, and B. Min, *Nature* 470, 369 (2011).
- [16] Z. Jacob, L. V. Alekseyev, and E. Narimanov, *Optics Express* 14, 8247 (2006).
- [17] H. Lee, Z. Liu, Y. Xiong, C. Sun, and X. Zhang, *Optics Express* 15, 15886 (2007).
- [18] Z. Liu, H. Lee, Y. Xiong, C. Sun, and X. Zhang, *Science* 315, 1686 (2007).
- [19] T. W. Ebbesen, H. J. Lezec, H. F. Ghaemi, T. Thio, and P. A. Wolff, *Nature* 391, 667 (1998).
- [20] F. J. García de Abajo, *Reviews of Modern Physics* 79, 1267 (2007).
- [21] A. Alù, G. D'Aguanno, N. Mattiucci, and M. J. Bloemer, *Physical Review Letters* 106, 123902 (2011).
- [22] J. Perruisseau-Carrier and A. K. Skriverviky, *IEEE Transactions on Microwave Theory and Techniques* 54, 1582 (2006).
- [23] M. Gil, J. Bonache, and F. Martín, *Metamaterials* 2, 186 (2008).
- [24] D. Schurig, J. J. Mock, B. J. Justice, S. A. Cummer, J. B. Pendry, A. F. Starr, and D. R. Smith, *Science* 314, 977 (2006).
- [25] L. H. Gabrielli, J. Cardenas, C. B. Poitras, and M. Lipson, *Nature Photon* 3, 461 (2009).
- [26] R. Liu, C. Ji, J. J. Mock, J. Y. Chin, T. J. Cui, and D. R. Smith, *Science* 323, 366 (2009).
- [27] J. Valentine, J. Li, T. Zentgraf, G. Bartal, and X. Zhang, *Nature Materials* 8, 568 (2009).
- [28] T. Ergin, N. Stenger, P. Brenner, J. B. Pendry, and M. Wegener, *Science* 328, 337 (2010).

- [29] U. Leonhardt, *Science* 312, 1777 (2006).
- [30] J. B. Pendry, D. Schurig, and D. R. Smith, *Science* 312, 1780 (2006).
- [31] A. V. Kildishev and V. M. Shalaev, *Optics Letters* 33, 43 (2008).
- [32] M. Rahm, D. A. Roberts, J. B. Pendry, and D. R. Smith, *Optics Express* 16, 11555 (2008).
- [33] B.-I. Popa and S. A. Cummer, *Physical Review B* 72, 165102 (2005).
- [34] B.-I. Popa and S. A. Cummer, *Physical Review E* 73, 016617 (2006).
- [35] D. R. Smith, S. Schultz, P. Markoš, and C. M. Soukoulis, *Physical Review B* 65, 195104 (2002).
- [36] X. Chen, T. M. Grzegorzcyk, B.-I. Wu, J. Pacheco, Jr., and J. A. Kong, *Physical Review E* 70, 016608 (2004).
- [37] L. Li Hou, J. Y. Chin, X. M. Yang, X. Q. Lin, R. Liu, F. Y. Xu, and T. J. Cui, *Journal of Applied Physics* 103 (2008).
- [38] C. Menzel, C. Rockstuhl, T. Paul, F. Lederer, and T. Pertsch, *Physical Review B* 77, 195328 (2008).
- [39] Z. Liu, C. T. Chan, and P. Sheng, *Physical Review B* 71, 014103 (2005).
- [40] G. W. Milton and J. R. Willis, *Proceedings of the Royal Society A: Mathematical, Physical and Engineering Science* 463, 855 (2007).
- [41] H. H. Huang, C. T. Sun, and G. L. Huang, *International Journal of Engineering Science* 47, 610 (2009).
- [42] Y. Lai, Wu, Ying, Sheng, Ping, and Zhang, Zhao-Qing, *Nature Materials* 10, 5 (2011).
- [43] F. Liu, Y. Lai, X. Huang, and C. T. Chan, *Physical Review B* 84, 224113 (2011).

- [44] A. P. Liu, R. Zhu, X. N. Liu, G. K. Hu, and G. L. Huang, *Wave Motion* 49, 411 (2012).
- [45] R. Zhu, X. N. Liu, G. L. Huang, H. H. Huang, and C. T. Sun, *Physical Review B* 86, 144307 (2012).
- [46] R. Zhu, G. K. Hu, and G. L. Huang, *Journal of Vibration and Acoustics* 134, 031006 (2012).
- [47] B. A. Auld, *Acoustic Fields and Waves in Solids* (Robert E. Krieger Publishing Company, Florida, 1990).
- [48] J. L. Rose, *Ultrasonic Waves in Solid Media* (Cambridge University Press, New York, 1999).
- [49] R. M. Jones, *Mechanics of Composite Materials* (Scripta, Washington, 1975).
- [50] D. R. Smith, P. Kolinko, and D. Schurig, *Journal of the Optical Society of America B* 21, 1032 (2004).
- [51] D. Torrent, A. Håkansson, F. Cervera, and J. Sánchez-Dehesa, *Physical Review Letters* 96, 204302 (2006).
- [52] J. B. Pendry and L. Jensen, *New Journal of Physics* 10, 115032 (2008).
- [53] D. Torrent and S.-D. José, *New Journal of Physics* 10, 023004 (2008).
- [54] D. Schurig and D. R. Smith, *New Journal of Physics* 7, 162 (2005).
- [55] G. P. Agrawal and S. Radic, *Photonics Technology Letters, IEEE* 6, 995 (1994).
- [56] R. Zengerle and O. Leminger, *Journal of Lightwave Technology* 13, 2354 (1995).
- [57] F. Bakhti and P. Sansonetti, *Electronics Letters* 32, 581 (1996).
- [58] F. Bakhti and P. Sansonetti, *Journal of Lightwave Technology* 15, 1433

- (1997).
- [59] I. E. Psarobas, N. Papanikolaou, N. Stefanou, B. Djafari-Rouhani, B. Bonello, and V. Laude, *Physical Review B* 82, 174303 (2010).
- [60] K. Subbarao and B. R. Rao, *Nature* 180, 978 (1957).
- [61] H. J. McSkimin, *The Journal of the Acoustical Society of America* 31, 287 (1959).
- [62] A. Bernard, M. J. S. Lowe, and M. Deschamps, *The Journal of the Acoustical Society of America* 110, 186 (2001).
- [63] P. D. Wilcox, M. J. S. Lowe, and P. Cawley, *Journal of Intelligent Material Systems and Structures* 12, 553 (2001).
- [64] K. F. Graff, *Wave Motion in Elastic Solids* (Oxford University Press, London, 1975).
- [65] J. D. Achenbach, *Wave Propagation in Elastic Solids* (North-Holland, New York, 1975).
- [66] P. S. Ma, H. W. Kim, J. H. Oh, and Y. Y. Kim, *Applied Physics Letters* 99 (2011).
- [67] M. K. Lee, P. S. Ma, I. K. Lee, H. W. Kim, and Y. Y. Kim, *Applied Physics Letters* 98 (2011).
- [68] J. H. Oh, I. K. Lee, P. S. Ma, and Y. Y. Kim, *Applied Physics Letters* 99 (2011).
- [69] S. J. Orfanidis, *Electromagnetic Waves and Antennas* (Rutgers Univ., Piscataway, 2008).
- [70] S. S. Stuchly and M. Matuszewski, *IEEE Transactions on Instrumentation and Measurement* 27, 285 (1978).

- [71] L. P. Ligthart, IEEE Transactions on Microwave Theory and Techniques 31, 249 (1983).
- [72] L. Li, Journal of the Optical Society of America A 13, 1024 (1996).
- [73] J. Baker-Jarvis, E. J. Vanzura, and W. A. Kissick, IEEE Transactions on Microwave Theory and Techniques 38, 1096 (1990).
- [74] B. Hosten, M. Deschamps, and B. R. Tittmann, The Journal of the Acoustical Society of America 82, 1763 (1987).
- [75] A. G. Every and W. Sachse, Physical Review B 42, 8196 (1990).
- [76] B. Hosten, The Journal of the Acoustical Society of America 89, 2745 (1991).
- [77] Y. Shih-Kuang, V. V. Varadan, A. Lakhtakia, and V. K. Varadan, Journal of Physics D: Applied Physics 24, 1601 (1991).
- [78] B. Hosten and M. Castaings, The Journal of the Acoustical Society of America 94, 1488 (1993).
- [79] S. I. Rokhlin and L. Wang, International Journal of Solids and Structures 39, 4133 (2002).
- [80] L. Wang and S. I. Rokhlin, The Journal of the Acoustical Society of America 112, 916 (2002).
- [81] W. T. Thomson, Journal of Applied Physics 21, 89 (1950).
- [82] D. L. Folds and C. D. Loggins, The Journal of the Acoustical Society of America 62, 1102 (1977).
- [83] R. B. Lindsay, The Journal of the Acoustical Society of America 11, 165 (1939).
- [84] J. R. Barber, *Elasticity* (Kluwer Academic, New York, 2002).
- [85] V. Fokin, M. Ambati, C. Sun, and X. Zhang, Physical Review B 76, 144302

(2007).

- [86] Z. Li, K. Aydin, and E. Ozbay, *Physical Review E* 79, 026610 (2009).
- [87] Y. Wu and Z.-Q. Zhang, *Physical Review B* 79, 195111 (2009).
- [88] T. Daniel and S.-D. José, *New Journal of Physics* 13, 093018 (2011).
- [89] C. Menzel, T. Paul, C. Rockstuhl, T. Pertsch, S. Tretyakov, and F. Lederer, *Physical Review B* 81, 035320 (2010).
- [90] Z. H. Jiang, J. A. Bossard, X. Wang, and D. H. Werner, *Journal of Applied Physics* 109 (2011).
- [91] T. M. Grzegorzczak, M. Nikku, C. Xudong, B.-I. Wu, and J.-A. Kong, *IEEE Transactions on Microwave Theory and Techniques* 53, 1443 (2005).
- [92] B.-I. Popa and S. A. Cummer, *Physical Review B* 80, 174303 (2009).
- [93] C. Rockstuhl, T. Paul, F. Lederer, T. Pertsch, T. Zentgraf, T. P. Meyrath, and H. Giessen, *Physical Review B* 77, 035126 (2008).
- [94] W. C. Chen, A. Totachawattana, K. Fan, J. L. Ponsetto, A. C. Strikwerda, X. Zhang, R. D. Averitt, and W. J. Padilla, *Physical Review B* 85, 035112 (2012).
- [95] J. Gerardin and A. Lakhtakia, *Microwave and Optical Technology Letters* 34, 409 (2002).
- [96] A. Fang, T. Koschny, and C. M. Soukoulis, *Physical Review B* 79, 245127 (2009).
- [97] B.-I. Wu, et al., *Microwave and Optical Technology Letters* 48, 680 (2006).
- [98] F. Bongard, I. Stevanovic, O. J. F. Martin, and J. R. Mosig, *First European Conference on Antennas and Propagation*, p.1 (2006).
- [99] Q. Cheng, W. Xiang Jiang, and T. Jun Cui, *Applied Physics Letters* 99 (2011).

- [100] Z. H. Jiang, M. D. Gregory, and D. H. Werner, *Physical Review B* 84, 165111 (2011).
- [101] R. J. Pollard, A. Murphy, W. R. Hendren, P. R. Evans, R. Atkinson, G. A. Wurtz, A. V. Zayats, and V. A. Podolskiy, *Physical Review Letters* 102, 127405 (2009).
- [102] A. A. Orlov, P. M. Voroshilov, P. A. Belov, and Y. S. Kivshar, *Physical Review B* 84, 045424 (2011).
- [103] S. S. Kruk, D. A. Powell, A. Minovich, D. N. Neshev, and Y. S. Kivshar, *Optics Express* 20, 15100 (2012).
- [104] L. Zigoneanu, B.-I. Popa, A. F. Starr, and S. A. Cummer, *Journal of Applied Physics* 109 (2011).
- [105] Å. Björck, *Numerical methods for least squares problems* (Siam, 1996).
- [106] R. Wangberg, J. Elser, E. E. Narimanov, and V. A. Podolskiy, *Journal of the Optical Society of America B* 23, 498 (2006).
- [107] P. A. Belov and Y. Hao, *Physical Review B* 73, 113110 (2006).
- [108] X. Ao and C. T. Chan, *Physical Review E* 77, 025601 (2008).
- [109] J. Li, L. Fok, X. Yin, G. Bartal, and X. Zhang, *Nature Materials* 8, 931 (2009).
- [110] J. Zhu, J. Christensen, J. Jung, L. Martin-Moreno, X. Yin, L. Fok, X. Zhang, and F. J. Garcia-Vidal, *Nature Physics* 7, 52 (2010).
- [111] H. J. Lee, H. W. Kim, and Y. Y. Kim, *Applied Physics Letters* 98 (2011).
- [112] A. N. Norris, *Wave Motion* 9, 509 (1987).
- [113] L. E. Kinsler, A. R. Frey, A. B. Coppers, and J. V. Sanders, *Fundamentals of Acoustics* (Wiley, New York, 1999).

- [114] G. H. Yoon, J. S. Jensen, and O. Sigmund, *International Journal for Numerical Methods in Engineering* 70, 1049 (2007).
- [115] B. Hassani, E. Hinton, *Homogenization and Structural Topology Optimization* (Springer, London, 1999).
- [116] Y. Wu, Y. Lai, and Z.-Q. Zhang, *Physical Review B* 76, 205313 (2007).
- [117] P. A. Martin, A. Maurel, and W. J. Parnell, *The Journal of the Acoustical Society of America* 128, 571 (2010).
- [118] Y. Wu, Lai, Yun, and Zhang, Zhao-Qing, *Effective Medium Theories and Symmetry Properties of Elastic Metamaterials* (InTech, 2012).
- [119] M. Wang and N. Pan, *Journal of Computational Physics* 228, 5978 (2009).
- [120] J. S. Lee, Y. Y. Kim, and S. H. Cho, *Smart Materials and Structures* 18, 015009 (2009).
- [121] A. V. Amirkhizi, A. Tehranian, and S. Nemat-Nasser, *Wave Motion* 47, 519 (2010).
- [122] H. W. Kim, H. J. Lee, and Y. Y. Kim, *NDT & E International* 46, 115 (2012).
- [123] D. W. L. Sprung, H. Wu, and J. Martorell, *American Journal of Physics* 61, 1118 (1993).
- [124] A. M. Steinberg, P. G. Kwiat, and R. Y. Chiao, *Physical Review Letters* 71, 708 (1993).
- [125] G. D'Aguanno, M. Centini, M. Scalora, C. Sibilìa, M. Bertolotti, M. J. Bloemer, C. M. Bowden, and J. W. Hans, *Summaries of papers presented at the Conference on Lasers and Electro-Optics*, p.598 (2001).
- [126] F. Kobayashi, S. Biwa, and N. Ohno, *International Journal of Solids and Structures* 41, 7361 (2004).

- [127] S. Feng, J. Elson, and P. Overfelt, *Optics Express* 13, 4113 (2005).
- [128] S. Feng, J. M. Elson, and P. L. Overfelt, *Physical Review B* 72, 085117 (2005).
- [129] J. M. Bendickson, J. P. Dowling, and M. Scalora, *Physical Review E* 53, 4107 (1996).
- [130] G. A. Luna-Acosta, F. M. Izrailev, N. M. Makarov, U. Kuhl, and H. J. Stöckmann, *Physical Review B* 80, 115112 (2009).
- [131] I. S. Nefedov and S. A. Tretyakov, *Physical Review E* 66, 036611 (2002).
- [132] L. Wu, S. He, and L. Chen, *Optics Express* 11, 1283 (2003).
- [133] W. Li and J. W. Y. Lit, *Journal of Lightwave Technology*, 15, 1405 (1997).
- [134] S. John, *Physical Review Letters* 58, 2486 (1987).
- [135] A. Kondilis and P. Tzanetakis, *Physical Review B* 46, 15426 (1992).
- [136] J. M. Frigerio, J. Rivory, and P. Sheng, *Optics Communications* 98, 231 (1993).
- [137] A. R. McGurn, K. T. Christensen, F. M. Mueller, and A. A. Maradudin, *Physical Review B* 47, 13120 (1993).
- [138] D. Zhang, W. Hu, Y. Zhang, Z. Li, B. Cheng, and G. Yang, *Physical Review B* 50, 9810 (1994).
- [139] M. M. Sigalas and C. M. Soukoulis, *Physical Review B* 51, 2780 (1995).
- [140] L. Wu, F. Zhuang, and S. He, *Physical Review E* 67, 026612 (2003).
- [141] M. I. Hussein, G. M. Hulbert, and R. A. Scott, *Journal of Sound and Vibration* 289, 779 (2006).
- [142] L. Zigoneanu, B.-I. Popa, and S. A. Cummer, *Physical Review B* 84, 024305 (2011).

- [143] A. Demma, P. Cawley, M. Lowe, and A. G. Roosenbrand, *The Journal of the Acoustical Society of America* 114, 611 (2003).
- [144] Z. Liu, C. He, B. Wu, X. Wang, and S. Yang, *Ultrasonics* 44, Supplement, e1135 (2006).
- [145] H. Kwun, S. Y. Kim, H. Matsumoto, and S. Vinogradov, *AIP Conference Proceedings* 975, 193 (2008).
- [146] M. Ratssepp, S. Fletcher, and M. J. S. Lowe, *The Journal of the Acoustical Society of America* 127, 730 (2010).
- [147] X. Jia, *The Journal of the Acoustical Society of America* 101, 834 (1997).
- [148] A. Peter and M. Shreefal, *Physics in Medicine and Biology* 42, 1763 (1997).
- [149] H. Zhilin and M. A. Badreddine, *Journal of Physics D: Applied Physics* 41, 215102 (2008).
- [150] X. Zhu, X. Zou, B. Liang, and J. Cheng, *Journal of Applied Physics* 108 (2010).
- [151] R. D. Kirz, and H. M. Ledbetter, *Elastic representation surfaces of unidirectional graphite/epoxy composites*, *Recent Advances in Composites in the United States and Japan*, p.661 (1983).
- [152] M. Schoenberg, *Geophysical Prospecting* 31, 265 (1983).
- [153] K. Helbig and M. Schoenberg, *The Journal of the Acoustical Society of America* 81, 1235 (1987).

APPENDIX

Density for Quartz:

$$\rho = 2651 \text{ kg/m}^3$$

Stiffness tensor for Quartz:

$$\mathbf{C} = \begin{bmatrix} 8.674 & 0.699 & 1.191 & -1.791 & 0 & 0 \\ & 8.764 & 1.191 & 1.791 & 0 & 0 \\ & & 10.72 & 0 & 0 & 0 \\ & & & 5.794 & 0 & 0 \\ & \text{sym} & & & 5.794 & -1.791 \\ & & & & & 3.988 \end{bmatrix} \times 10^{10} \text{ N/m}^2$$

Density for Rutile:

$$\rho = 4260 \text{ kg/m}^3$$

Stiffness tensor for Rutile:

$$\mathbf{C} = \begin{bmatrix} 26.60 & 17.33 & 13.62 & 0 & 0 & 0 \\ & 26.60 & 13.62 & 0 & 0 & 0 \\ & & 46.99 & 0 & 0 & 0 \\ & & & 12.39 & 0 & 0 \\ & \text{sym} & & & 12.39 & 0 \\ & & & & & 18.86 \end{bmatrix} \times 10^{10} \text{ N/m}^2$$

ABSTRACT (KOREAN)

탄성 메타물질의 유효 특성 정의 및 이를 이용한 파동 테일러링

이 형 진

서울대학교 대학원

기계항공공학부

본 연구에서는 비등방성 탄성 메타물질의 유효 특성을 정의하는 방법론에 대해서 다루었다. 메타물질의 유효 특성 정의 방법과 관련하여, 전자기학 메타물질 분야에서는 산란계수를 이용하는 정의 방법이 가장 효율적인 방법으로 알려져 있고, 널리 사용되고 있다. 하지만 기존의 이 정의 방법은 탄성 메타물질의 유효 특성을 온전히 정의하는데 적용될 수 없다. 이는 탄성 메타물질 고유의 복잡한 구조특성 때문인데, 탄성 메타물질의 강성 행렬은 인장-인장 결합과 인장-전단 결합과 관련된 비대각 행렬 요소를 포함하고 있다. 때문에 비등방성 탄성 메타물질의 유효 특성을 정의하기 위해서는, 기존의 산란계수를 이용하는 정의 방법은 개선되어야 한다.

이를 위하여, 본 연구에서는 비등방성 탄성 메타물질에 적용 가능한 개선된 정의 방법을 제안하였다. 제안한 방법은 크게 두 단계의 정의 과정으로 이루어져 있다. 첫 번째는 수직 입사를 이용하여 탄성 메타물질의 산란계수를 추출하고 이와 관련된 유효 특성을 정의하는 과정이고, 두 번째는 경사 입사를 이용하여 산란계수를 추출하고 관련된

유효 특성을 정의하는 과정이다. 기존의 방법이 특정 주축을 갖는 탄성 메타물질에 적용되어 대각 강성 행렬 요소만을 정의할 수 있었던 데에 반해, 제안한 방법은 다양한 주축을 갖는 탄성 메타물질에 적용되어 모든 강성 행렬 요소를 정의할 수 있다.

제안한 정의 방법을 이용하여, 특이한 특성을 갖는 세 가지 탄성 메타물질을 설계하였고 이를 탄성 확대 하이퍼렌즈, 기계적 밴드패스 필터, 파동 모드 전환기를 구현하는데 적용하였다. 먼저, 금속과 공기가 적층된 형상의 극한의 비등방성 탄성 메타물질을 제안하였고, 이를 이용하여 탄성 확대 하이퍼렌즈를 구현하였다. 구현한 하이퍼렌즈는 일반적인 (파동을 이용한) 영상화 기기의 해상도 한계인 회절 한계를 극복하여 고해상도 영상화를 가능케 함을 확인하였고, 이를 실험을 통해 검증하였다. 다음으로, 물질의 특성 임피던스만을 변화시킬 수 있는 탄성 메타물질을 제안하였고 이를 특성 임피던스가 변화되는 포노닉 밴드갭 구조물에 적용하여 이상적인 기계적 밴드패스 필터를 설계하였다. 설계한 밴드패스 필터는 평평한 통과대역과 주위의 넓은 차단대역, 그리고 가파른 통과대역 경계를 가짐을 확인하였다. 마지막으로, 특이한 편광 특성을 갖는 비등방성 탄성 메타물질을 제안하였고 이를 이용하여 파동 전환기를 설계하였다. 설계한 파동 전환 시스템은 주위 환경에 상관없이 견고하고 고효율의 성능을 보임을 확인하였다.

주요어: 비등방성 탄성 메타물질, 산란계수를 이용한 유효 특성 정의 방법, 탄성 확대 하이퍼렌즈, 기계적 밴드패스 필터, 파동 모드 전환기

학번: 2008-20784

ACKNOWLEDGEMENT

This work was supported by the National Research Foundation of Korea (NRF) grant (No: 2013035194) funded by the Korean Ministry of Education, Science and Technology (MEST) contracted through IAMD at Seoul National University.